

Implantable Wireless Intraocular Pressure Sensors

Thesis by

Po-Jui Chen

In Partial Fulfillment of the Requirements
for the Degree of

Doctor of Philosophy



California Institute of Technology

Pasadena, California

2009

(Defended July 16, 2008)

© 2009

Po-Jui Chen

All Rights Reserved

To my family

Acknowledgements

All the work in this thesis would not have been possible without remarkable guidance from my graduate research advisor, Dr. Yu-Chong Tai. I have been very fortunate to work with him for the past five years of my M.S./Ph.D. study at Caltech in many aspects, as he is a great model showing me how a scientist, a researcher, or an engineer thinks, acts, and talks; how to be creative, critical, analytical, exclusive, and passionate in our work duties; how to manage projects and time yet maintain balance between work and personal/family lives. It was really fun learning something from him from time to time if not every day. He has also given me many opportunities since he offered to let me join his group when I was still in Taiwan. I ought to give my most credit to him for my research achievements so far, and for possibly more in the future.

I will always remember the tremendous help from all previous and current student members—my friends in fact—that I had a chance to work with in Yu-Chong's group Caltech Micromachining Laboratory: Drs. Ellis Meng, Jun Xie, Justin Boland, Matthieu Liger, Qing He, Victor Chi-Yuan Shih, Scott Miserendino, Changlin Pang, Angela Tooker, Siyang Zheng, Damien Roger, Jason Shih; Ms. Wen Li; and Messrs. Nick Lo, Brandon Quach, Mike Liu, Luca Giacchino, Ray Huang, Jeffrey Lin, Monty Nandra, and Justin Kim. I give my word that they will be unforgettable in my memory, especially Justin Boland who taught me how to draw my first lithography mask; Damien who revised my manuscripts along the way, creating beautiful publications in the end so many times that even I lost count; Ellis, Damien, Wen, and Jeffrey, with whom I had lots of valuable

discussion and collaboration on different interesting research projects; and Victor who shared so much fun with me and gave so many good suggestions on my student life and career plan. I also appreciate Mesdames Tanya Owen, Christine Garske, Agnes Tong, and Mr. Trevor Roper for their great administrative and clean-room facility assistance during my time in this energetic and productive group.

The interdisciplinary nature of my work with biomedical application involvement enabled me to gain plenty of medical and surgical knowledge from my collaborators at the Keck School of Medicine at the University of Southern California and Doheny Eye Institute, to whom I am deeply grateful: Drs. Mark Humayun, Rohit Varma, Rajat Agrawal, and Saloomeh Saati. Their bright insights, along with amazing operations during numerous surgical trials of my devices, effectively clarified many issues as we moved forward in investigating science and engineering in microdevice research and development. Excellent facilitation from Dr. Sean Caffey and Ms. Mindy Morefield from USC Biomimetic MicroElectronic Systems (BMES) NSF Engineering Research Center on efficient project management, as well as close interaction with our industrial partner, is also gratefully acknowledged. Moreover, I would like to thank my Ph.D. candidacy and defense committee members, including Yu-Chong and Ellis for their helpful comments and suggestions on my thesis work: Drs. Kaushik Bhattacharya, Joel Burdick, Azita Emami, Demetri Psaltis, and Changhuei Yang.

I thank all my friends, especially the ones either in Taiwan or affiliated here with the Association of Caltech Taiwanese (ACT), for bringing me such good times to make my graduate student life fruitful and enjoyable during my days at Caltech. I really learnt a lot

from each of them. My parents, Kuan-Hung Chen and Pao-Yu Lin, and my elder brother, Bruce Po-Chia Chen, have been solidly and continuously backing me up ever since I was young. I sincerely thank them for everything. Last, but the most important in my life, I could not express how much I have received from my wife Tina Yuan-Ting Lin since our phenomenal encounter at the campus of National Taiwan University in January of 1999. I will never forget how many wonderful things appeared to me because of her after that. She has always been there for me over these nine years with her wholehearted cheers, advice, and love. I would not have come this far, nor had such pleasant Caltech and American experiences without her. With all that said, I could not ever return anything to my family to match their endless support and encouragement that lead to my fearless and undisturbed study at Caltech. But I dedicate this piece of work to them as a proof of our endeavors that ultimately made it happen.

Abstract

Implantable Wireless Intraocular Pressure Sensors

Thesis by

Po-Jui Chen

Doctor of Philosophy in Electrical Engineering

California Institute of Technology

The work in this thesis aims to develop a suite of biomedical microdevice implants, with an intense focus on pressure sensors, for glaucoma study and management featuring the enabling micro-electro-mechanical-system (MEMS) technologies and the use of parylene (poly-para-xylene) as a biocompatible MEMS material. The problems of the debilitating eye disease glaucoma threaten tens of millions of people worldwide with loss of vision, and are not completely resolved using the current non-optimal clinical procedures. Given the relation of neuropathy and the physiological parameter of intraocular pressure (IOP) in glaucoma from clinical findings, such parylene-based MEMS implants are investigated to realize physical IOP monitoring and regulation, and further to accomplish continuous, direct, accurate, reliable, and more effective glaucoma detection and treatment.

Miniaturized parylene-based passive pressure sensors are presented in this thesis for IOP monitoring. Complete design, fabrication, characterization, and analysis of such MEMS implants are described to demonstrate their feasibility, covering both engineering and surgical/biological aspects of the proposed applications. Their passive behaviors, based on the comprised micromechanical structures, facilitate unpowered device operations. In addition, such devices are microfabricated in suitable form factors so that minimally invasive suture-less implantation procedures are possible, minimizing time and complexity of the surgeries. Two types of micromachined wireless pressure sensors are developed utilizing optical and electrical sensing methodologies, respectively, to explore the possibility of the proposed implant approach. On-bench experimental results verify that wireless pressure sensing with 1 mmHg accuracy in the 0–100 mmHg range can be achieved using both types of devices. Surgical studies, including *ex vivo* and *in vivo* animal tests, confirm the bioefficacy and biostability of the device implants in the intraocular environment. With the attempt of providing implementation concepts of the MEMS implant approaches for ultimate glaucoma study and management in practice, system-level designs and configurations involving such microdevice implants are briefly described as well. Micromachined passive-valved flow-control devices with designed surgical and engineering features are also developed (experimentally achieving 0–100 mmHg and 0–10 $\mu\text{L}/\text{min}$ pressure and flow rate regulation ranges) to investigate the feasibility and possibility of such implant approach for unpowered physical IOP regulation in glaucoma treatment.

Table of Contents

Chapter 1	Glaucoma and Intraocular Pressure.....	1
1.1	Clinical Problems of Glaucoma.....	1
1.2	Physiological Influence of Intraocular Pressure on Glaucoma.....	4
1.3	Clinical Procedures for Intraocular Pressure Monitoring.....	6
1.4	Clinical Procedures for Intraocular Pressure Regulation.....	9
1.5	Summary.....	14
1.6	Bibliography	15
Chapter 2	MEMS Implant Approaches for Intraocular Pressure	
	Monitoring and Regulation.....	19
2.1	MEMS Implant Approach for Intraocular Pressure Monitoring.....	19
2.2	MEMS Implant Approach for Intraocular Pressure Regulation	22
2.3	Summary.....	26
2.4	Bibliography	27
Chapter 3	Implantable Parylene-Based Intraocular Pressure Sensors	
	with Electrical Readouts	29
3.1	Overview.....	29
3.2	Implant Design.....	30
3.2.1	Background.....	30
3.2.2	Sensing scheme.....	33
3.2.3	Sensor design	35
3.3	Device Fabrication.....	39
3.4	Characterization Results	44

3.4.1	Electrical characterization	45
3.4.2	On-bench pressure sensing test.....	47
3.4.3	<i>Ex vivo</i> pressure sensing test.....	52
3.4.4	<i>In vivo</i> implantation test.....	54
3.5	Improvement Strategies and Results	55
3.5.1	Improved sensor design and fabrication.....	55
3.5.2	Improved readout method design and implementation	60
3.5.3	Characterization results and discussions	66
3.6	Summary.....	82
3.7	Bibliography	83

Chapter 4 Implantable Parylene-Based Intraocular Pressure Sensors

	with Optical Readouts	87
4.1	Overview.....	87
4.2	Implant Design.....	88
4.2.1	Sensing scheme.....	88
4.2.2	Sensor design	89
4.2.3	Device packaging.....	91
4.3	Device Fabrication.....	92
4.4	Characterization Results and Discussions	97
4.4.1	<i>In vitro</i> pressure sensing test.....	97
4.4.2	<i>In vivo</i> anchoring test.....	100
4.4.3	<i>Ex vivo</i> pressure sensing test.....	101
4.4.4	<i>In vivo</i> implantation test.....	102
4.4.5	Temperature effect characterization.....	103
4.5	Summary	107
4.6	Bibliography	108

Chapter 5 Implantable Parylene-Based Intraocular Pressure

Drainage Devices.....	109
5.1 Overview.....	109
5.2 Surgical Design of Implant: Tissue Anchors	110
5.2.1 Background.....	110
5.2.2 Design and fabrication.....	111
5.2.3 Characterization results and discussions	114
5.3 Engineering Design of Implant: Microvalves.....	117
5.3.1 Background.....	117
5.3.2 Design and fabrication.....	118
5.3.3 Characterization results and discussions	124
5.4 Summary.....	131
5.4 Bibliography	132
 Chapter 6 Conclusions	 135
 Appendix Introduction to MEMS Technology	 139
A.1 MEMS.....	139
A.1.1 Origin and definition.....	139
A.1.2 Technology.....	141
A.1.3 Products and market.....	148
A.2 Implantable Medical MEMS	150
A.3 Polymeric MEMS Materials	153
A.3.1 Overview.....	153
A.3.2 Parylene	154
A.4 Summary.....	162
A.5 Bibliography	163

Figure 1-1: Loss of vision by glaucoma	2
Figure 1-2: Anatomy of the human eye	3
Figure 1-3: Ophthalmoscopic examination of glaucomatous eye with optic disc cupping indication	3
Figure 1-4: Illustration of optic nerve damage mechanism	4
Figure 1-5: Circulation path of aqueous humor in the human eye	6
Figure 1-6: Applanation tonometry.....	7
Figure 1-7: Concept of non-contact applanation tonometry	8
Figure 1-8: Improvement of intraocular fluid drainage by surgery therapy	11
Figure 1-9: State-of-the-art GDDs	13
Figure 1-10: Glaucoma tube shunt implantation	13
Figure 2-1: Concept of MEMS implant approach for continuous IOP monitoring.....	21
Figure 2-2: Surgical placement of the MEMS implant (highlighted in red).....	23
Figure 2-3: Proposed IOP regulation profile of the MEMS implant	25
Figure 3-1: Wireless passive MEMS pressure sensors for physiological parameter measurements in literature	31
Figure 3-2: Passive wireless IOP sensing concept.....	34
Figure 3-3: Proposed IOP monitoring in practice	35
Figure 3-4: Pressure sensor design (top view).....	35
Figure 3-5: Sensor design (cross-sectional view; not to scale) in variable capacitor (top) and variable capacitor/inductor (bottom) variations	39
Figure 3-6: Fabrication process flow of microsensors.....	41
Figure 3-7: Images of microfabricated devices	42
Figure 3-8: Volume change effect in gas-sealed MEMS gauge pressure sensors.....	43

Figure 3-9: Representative captured frequency scan of the equivalent impedance Z_{eq} of the reader coil coupled with the microsensor	46
Figure 3-10: On-bench pressure testing setup for device characterization.....	47
Figure 3-11: Overlay plot of measured phase-dip curves of the sensor (variable capacitor design as example) in on-bench wireless pressure sensing	48
Figure 3-12: On-bench pressure testing results of the sensors	51
Figure 3-13: <i>Ex vivo</i> device testing to demonstrate the wireless pressure sensing behavior of the sensor implant.....	53
Figure 3-14: Overlay plot of measured phase-dip curves of the sensor (variable capacitor design as example) in <i>ex vivo</i> wireless pressure sensing	53
Figure 3-15: Follow-up study results of <i>in vivo</i> device testing using rabbit model to verify long-term biocompatibility of the intraocular implant.....	54
Figure 3-16: Pressure sensor design with flexible parylene coil disk (top view)	57
Figure 3-17: Fabrication process flow of modified flexible-coiled microsensor	58
Figure 3-18: Full-scale image of the modified flexible-coiled microsensor with its top (left) and bottom (right) views.....	59
Figure 3-19: Device flexibility demonstration.....	59
Figure 3-20: Photographs of the captured frequency scans showing detected impedance phase dip with the modified flexible-coiled sensor	60
Figure 3-21: Photographs of the captured frequency scans when the sensing distance was 1 cm.....	61
Figure 3-22: Process scheme of developed data-processed external readout method	63
Figure 3-23: Data samples through Option 1 operations for example.....	64
Figure 3-24: Frequency averaging with data samples used in Figure 3-23 to illustrate the enhanced phase dip detection scheme.....	65
Figure 3-25: Another data sample used to illustrate the frequency averaging operation..	66

Figure 3-26: Schematic of on-bench pressure testing setup for characterization of the modified flexible-coiled sensor.....	67
Figure 3-27: Overlay plot of the measured phase-dip curves of the modified sensor in on-bench wireless pressure sensing	68
Figure 3-28: On-bench pressure testing result of the modified sensor	69
Figure 3-29: Characterization of volume change effect of the encapsulated air	69
Figure 3-30: Sample size effect on frequency measurements.....	71
Figure 3-31: Sensing distance study using $Q_s \sim 45$ sensor with approximately 4-mm-diameter on-sensor coil	73
Figure 3-32: Interaction effect in different wave-transmission media.....	74
Figure 3-33: Representative iris anchor assembly result (side view)	77
Figure 3-34: Implanted flexible-coiled pressure sensor in the intraocular environment of rabbit eye model.....	78
Figure 3-35: Follow-up study results of <i>in vivo</i> device testing using rabbit model to verify biocompatibility of the modified flexible-coiled implant.....	78
Figure 3-36: Acute <i>in vivo</i> device testing using rabbit model	79
Figure 3-37: Acute <i>ex vivo</i> device testing using enucleated porcine eye model.....	80
Figure 4-1: Concept of the micromechanical IOP sensor for optical sensing	90
Figure 4-2: Schematics of fully-packaged implantable device (not to scale).....	92
Figure 4-3: Fabrication process flow of the needle-implantable sensors as example.....	94
Figure 4-4: Microfabricated high-sensitivity parylene-based IOP sensors in spiral-tube (left) and long-armed-tube (right) designs	95
Figure 4-5: Integrated packaging components of the needle-implantable parylene-based IOP sensors.....	96
Figure 4-6: Microfabricated needle-implantable parylene-based IOP sensors	96
Figure 4-7: Schematic of on-bench pressure testing setup for device characterization....	98
Figure 4-8: <i>In vitro</i> pressure response of the high-sensitivity IOP sensors in water	99

Figure 4-9: <i>In vitro</i> pressure response of the needle-implantable IOP sensors in water...	99
Figure 4-10: <i>In vivo</i> anchoring test with fundus photograph (left) and fluorescein angiogram (right) taken after 1 month of study	100
Figure 4-11: <i>Ex vivo</i> pressure response of the high-sensitivity long-armed-tube IOP sensor.....	101
Figure 4-12: <i>Ex vivo</i> characterization of the needle-implantable IOP sensor.....	102
Figure 4-13: <i>In vivo</i> animal study using rabbit eyes with functional needle-implantable IOP sensor	103
Figure 4-14: Illustration of temperature effect on the IOP sensor	104
Figure 4-15: Parylene spiral tube for temperature effect characterization.....	105
Figure 4-16: Schematic of on-bench temperature testing setup.....	106
Figure 4-17: Characterization results.....	106
Figure 4-18: Concept of sensor-pair configuration.....	106
Figure 5-1: Concept of the needle-based device implantation scheme.....	111
Figure 5-2: Designs of flexible tissue anchor of the implant.....	112
Figure 5-3: Fabrication process flow of tube-type implant prototype with silicon- embedded arms as example of anchoring structures.....	113
Figure 5-4: Microfabricated parylene-based implants (middle) with SEM images highlighting their artificial conduit before release (left) and flexible tissue anchors after release (right)	113
Figure 5-5: Pressure/flow rate testing result of the microchannel conduit	115
Figure 5-6: <i>In vitro</i> tissue anchor testing	115
Figure 5-7: Needle-based implantation surgery of the device	116
Figure 5-8: <i>In vivo</i> animal study of the flexible tissue anchor.....	116
Figure 5-9: Fluidic and electronic diodes	118
Figure 5-10: Concept of dual-valve configuration featuring combination of tethered-disk microvalves in normally-closed and normally-open check valve designs.	119

Figure 5-11: Concept of single-valve configuration featuring floating-disk microvalve in pressure-bandpass check valve design.....	120
Figure 5-12: Fabrication process flow of dual parylene-based microvalves	121
Figure 5-13: Fabrication process flow of single parylene-based microvalve	122
Figure 5-14: Micrographs of the fabricated dual-valved channel (2 mm long in port-to-port distance) and cut-in views of the normally-closed (left) and normally-open (right) parylene check valves, all in top view	123
Figure 5-15: Micrographs of the fabricated floating-disk parylene single valves with different design variations immersed in water (top view)	123
Figure 5-16: Schematic of fluidic testing setup for device characterization	125
Figure 5-17: Dual valve characterization result to water microflow control.....	127
Figure 5-18: Single valve characterization result to water microflow control	128
Figure 5-19: Concept of representative dual-valved tube shunt implant integration for <i>in vivo</i> study	130
Figure A-1: Scale of things	140
Figure A-2: MEMS implementation concept with micromechanical structures as the key to realization of macro-to-micro communication and interfacing.....	141
Figure A-3: Concept of batch-fabrication process in silicon processing technology	142
Figure A-4: Concept of pattern transfer process in silicon processing technology	142
Figure A-5: Microelectronics development	143
Figure A-6: MEMS development.....	143
Figure A-7: Comparable trend of MEMS technology development to Moore's law in IC industry.....	143
Figure A-8: Silicon-based micromachining technology including bulk micromachining (left) and surface micromachining (right)	144
Figure A-9: Bulk-micromachined structure examples.....	145
Figure A-10: Examples of high-aspect-ratio (HAR) structures created by DRIE	145

Figure A-11: Concept of surface micromachining.....	146
Figure A-12: Micromachined structures by SUMMiT™ Technologies	147
Figure A-13: Micro optics system including laser, 3 Fresnel lenses, beam splitter, and 45° mirror.....	147
Figure A-14: Assembled 3-D microstructures	147
Figure A-15: MEMS evolution	148
Figure A-16: Analysis of global MEMS market 2006–2011	149
Figure A-17: Geographical breakdown of MEMS players	149
Figure A-18: Top 30 worldwide MEMS manufacturers (ranked by estimated 2007 revenues)	149
Figure A-19: Analysis of MEMS components for life sciences market 2005–2012	150
Figure A-20: MEMS for implantable applications	151
Figure A-21: Graphical overview of acute MEMS implants	152
Figure A-22: Graphical overview of chronic MEMS implants	152
Figure A-23: Commercially available parylene types.	155
Figure A-24: Parylene preparation.....	156
Figure A-25: Processed parylene film from a silicon wafer	158
Figure A-26: Concept of low-temperature multi-layer parylene micromachining technology	159
Figure A-27: Microfabricated parylene-based devices	159
Figure A-28: Integrated parylene LC-MS/MS microsystem	159
Figure A-29: Neural probe implant for cortex signal recording and stimulation	160
Figure A-30: Spinal cord prosthesis for neural stimulation.....	161
Figure A-31: Integrated intraocular prosthesis for retinal stimulation.....	161

List of Tables

Table 2-1: Design specifications of the proposed sensor implant paradigm for practical IOP monitoring.....	22
Table 2-2: Design specifications of the proposed device implant paradigm for practical IOP regulation.....	25
Table 3-1: Measured electrical parameters of the microfabricated pressure sensors.....	45
Table 3-2: Measured characteristics of the microfabricated pressure sensors	51
Table 3-3: Measured electrical parameters of the flexible-coiled pressure sensor	67
Table 3-4: Measured characteristics of the flexible-coiled pressure sensor.....	76
Table 4-1: Geometric designs of compliant structures for the IOP sensor	90
Table 4-2: Design metrics of the fabricated micromechanical IOP sensors	97
Table 5-1: Design metrics of the valved microvalves developed in this work	124
Table 5-2: Comparison of the developed parylene-based microvalves in regular check valve operation for flow shunting	128
Table 5-3: Comparison of the developed parylene-based microvalves with implementation considerations.....	129
Table A-1: Representative polymeric MEMS materials	154
Table A-2: Material properties of parylene N, C, D, and HT	157
Table A-3: Comparison of parylene N, C, and HT	157

CHAPTER 1

GLAUCOMA AND INTRAOCULAR PRESSURE

1.1 Clinical Problems of Glaucoma

Glaucoma is a debilitating eye disease that chronically damages the optic nerve and results in loss of vision and blindness for tens of millions of people worldwide [1–5]. It is the second leading cause of blindness in the world, according to the World Health Organization (WHO), after cataracts. Estimated incidences of glaucoma will occur to over 60 million people worldwide by 2010. Although blindness ranked third (after cancer and heart disease) as people's major fear, very few people are aware of glaucoma in its early development because there are no perceivable symptoms, making it extremely difficult to diagnose before it is already quite advanced and induces permanent visual damage. In fact, unfortunately, 10%–25% of people with glaucoma who receive clinical

treatments still experience loss of vision and blindness. The loss of vision from glaucoma starts with patients missing objects to the side and out of the corner of their eye. Gradually patients lose their peripheral (side) vision and seem to be looking through a tunnel, as shown in Figure 1-1. Over time, even their straight-ahead vision may decrease until no vision remains.



(a)



(b)

Figure 1-1: Loss of vision by glaucoma. (a) Normal vision. (b) Same scene as viewed by a patient with glaucoma. Images courtesy of National Eye Institute.

Pathological studies indicate that loss of vision in glaucomatous eyes results from damaged optic nerves in a characteristic pattern of optic neuropathy of the eye. The optic nerve is a bundle of more than 1 million nerve fibers located at the posterior segment of the eye, as shown in Figure 1-2. It provides a connecting neural pathway to transfer visual information from the retina to the brain. Ophthalmoscopic examination of a glaucomatous eye, as shown in Figure 1-3, reveals the cupping of the optic disc as an indication of optic nerve damage progression, which leads to loss of vision.

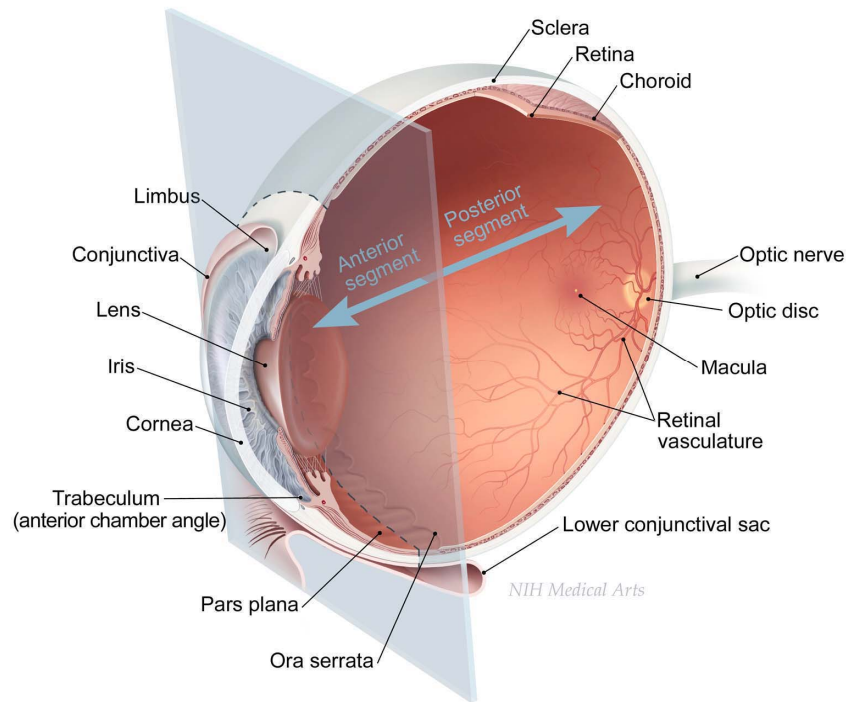


Figure 1-2: Anatomy of the human eye. Drawing courtesy of NIH Medical Arts.

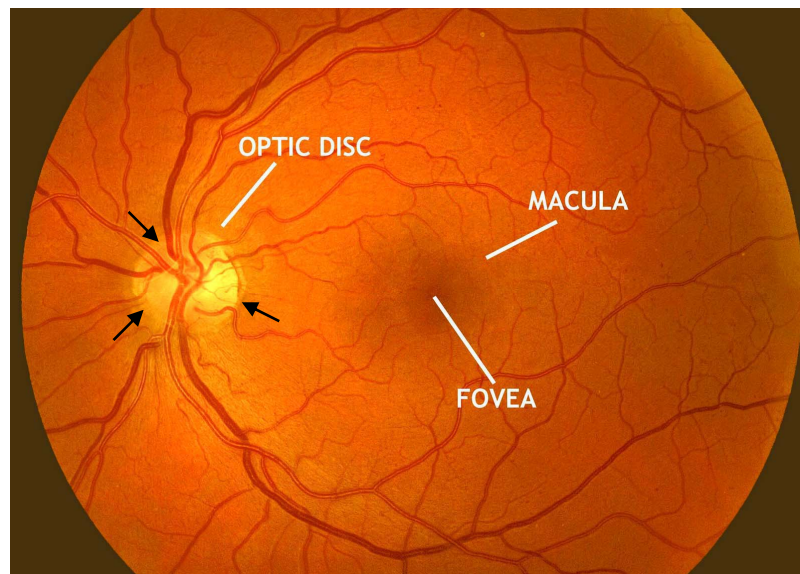


Figure 1-3: Ophthalmoscopic examination of glaucomatous eye with optic disc cupping indication. The arrows indicate the edge of the “cup” of the optic disc. The pale region of the cup is interpreted where optic nerve damage occurs. Image adapted from [6].

1.2 Physiological Influence of Intraocular Pressure on Glaucoma

Although the mechanism of optic nerve damage by glaucoma is not resolved yet, the mostly accepted hypothesis is the adverse suppression from abnormally elevated intraocular pressure (IOP) induced by glaucoma, as shown in Figure 1-4. The elevated IOP hypothetically obstructs the blood flow to the optic nerve, leading to damage and ultimate loss of the nerve (i.e., optic disc cupping, as shown in Figure 1-3). Note that the damage is not accompanied by any pain even while permanent and irreversible, meaning the damaged optic nerve can not be cured or regained. Current clinical treatments including medications and/or surgeries can only prevent the damage progression from further visual deterioration. Therefore, lifelong monitoring and immediate treatment are definitely necessary for successful glaucoma management.

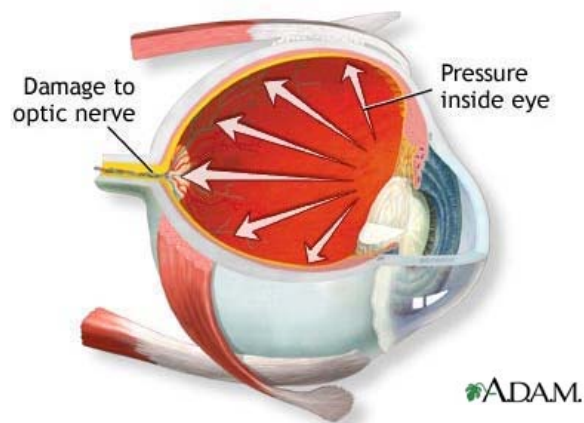


Figure 1-4: Illustration of optic nerve damage mechanism. Drawing courtesy of A.D.A.M.

Abnormal elevation of IOP results from accumulation of ocular fluid in glaucomatous eyes. In normal eyes, a clear fluid called aqueous humor flows continuously within the eye chamber and nourishes nearby tissues. The aqueous humor is produced primarily from the ciliary processes [7] and drained from the anterior chamber

at an open angle where the cornea and iris meet, as shown in Figure 1-5. When the fluid reaches the angle, it flows through a spongy meshwork called trabecular meshwork, analogous to a drain, and leaves the eye. The production rate of aqueous humor corresponds to a turnover rate of approximately 1% of the anterior chamber volume per minute ($2\text{--}3\text{ }\mu\text{L}/\text{min}$) [7, 8]; in a balance with the drainage rate this provides good circulation to maintain sufficient ocular rigidity and visual acuity. The production varies diurnally but is relatively independent of IOP. More details of aqueous humor production and drainage mechanisms can be found in [7]. In glaucomatous eyes, although the aqueous humor production is unaffected, its drainage is impeded at the angle through the influenced meshwork drain, leading to fluid accumulation, IOP elevation, and ultimately optic nerve damage. Specifically, this form of glaucoma is called open-angle glaucoma [3] and is the most common and the most referenced type. Other forms such as low-tension (normal-tension, where no abnormal IOP elevation occurs), angle-closure, congenital, and secondary glaucomas also exist with different causes and medical complications, but they are not as common as the open-angle form. Consequently, only diagnoses and treatments for open-angle glaucoma are described in this work. In spite of no set threshold for an IOP that causes glaucoma, it is generally recognized that normal IOP ranges from 10–15 mmHg, and values over 15–20 mmHg are considered at risk. Because elevated IOP is highly associated with glaucoma, this crucial risk factor needs to be carefully monitored and controlled, even in a real-time (*in situ*) fashion. Current clinical procedures for IOP monitoring and regulation are described in the following sections, and concepts of the correspondingly proposed MEMS-implant-based approaches in this work are presented in Chapter 2.

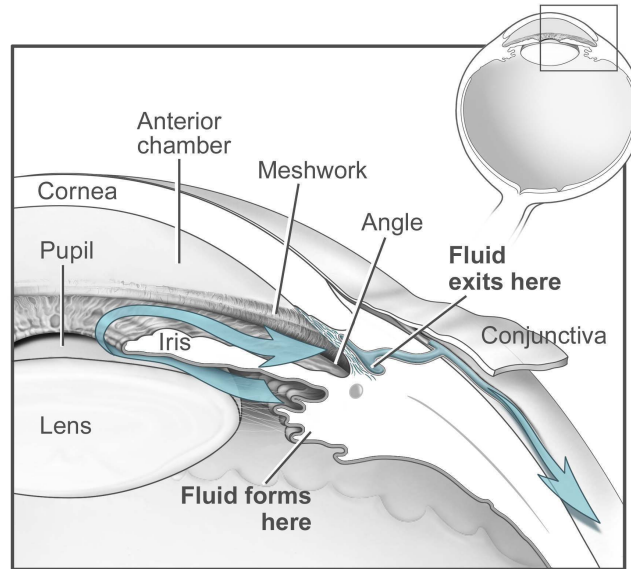


Figure 1-5: Circulation path of aqueous humor in the human eye. Drawing courtesy of National Eye Institute.

1.3 Clinical Procedures for Intraocular Pressure Monitoring

Current clinical procedures for IOP measurement utilize applanation tonometry [9] as the standard method. The concept, as shown in Figure 1-6, is to apply a measurable force to the corneal surface with a probe. An ophthalmologist examines when a portion of the cornea is flattened out with the advance of the probe and measures how much applanation force is applied. As a result, this force balancing the internal pressure of the cornea over a determined area can be obtained to calculate the related IOP. Goldmann applanation tonometry (GAT) [10] and tonopen (Reichert Inc., Depew, NY) are the representative examples of this method. Compared with this contact tonometry, the non-contact tonometry [11, 12], such as pneumotonometry (i.e., air-puff tonometry), is more often used nowadays in clinics for more convenient IOP measurements. In this method, the cornea curvature is monitored by a light beam with the setup shown in Figure 1-7,

while a puff of air is directed to the cornea as the applanation force, similar to contact tonometry. During operation the air-puff pressure is increased until it flattens a determined area of the cornea under surveillance through the optical system, and the obtained pressure balancing the internal pressure of the cornea can be used to estimate the related IOP. This method allows a large number of measurements in a relatively shorter period and more accurate readouts with minimal natural refractory responses from the targets during the measurement.

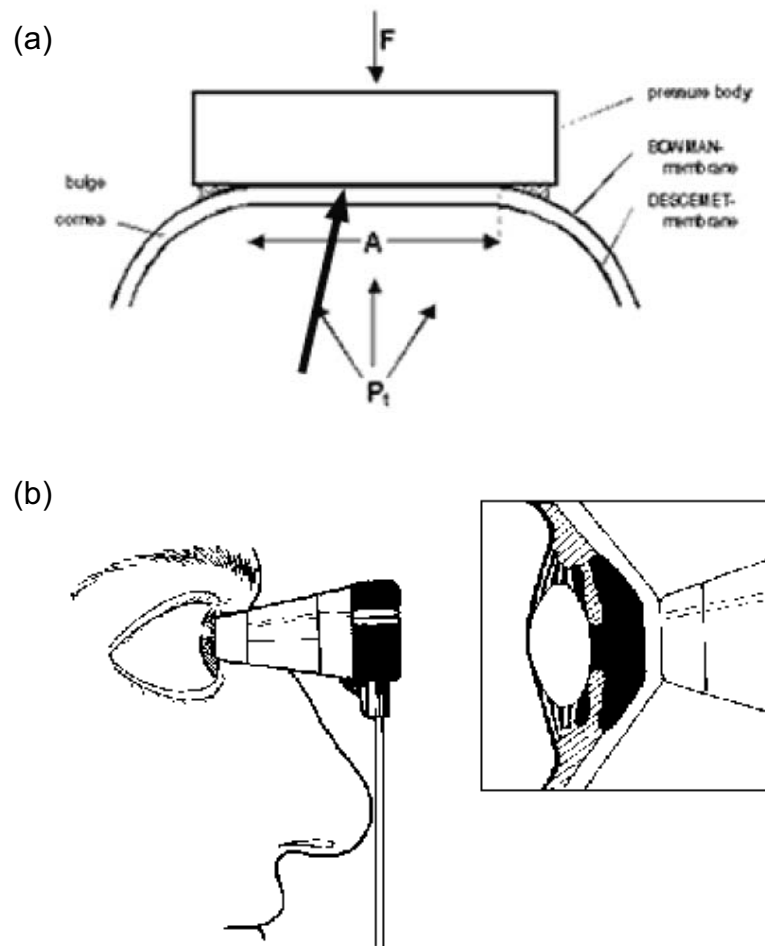


Figure 1-6: Applanation tonometry. (a) Concept. (b) Illustration of actual implementation.

Image (a) courtesy of Dr. Kirstein and (b) reprinted from [13].

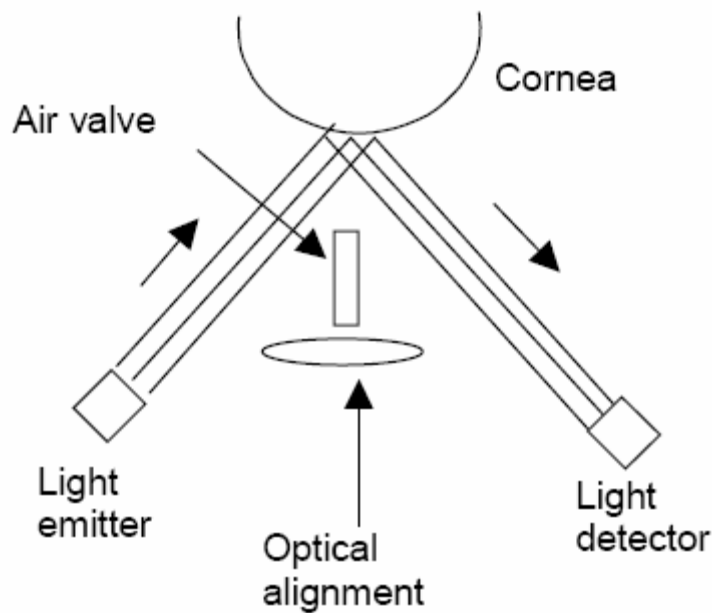


Figure 1-7: Concept of non-contact applanation tonometry. Image reprinted from [12].

Although applanation tonometry is the current clinical standard, it has difficulty in achieving faithful IOP readouts because of its indirect measurement nature. Its implementation also causes low precision and low repeatability in common practice, especially in the contact scheme. In addition, difference of dimensions (e.g., corneal thickness and curvature) and mechanical properties (e.g., ocular rigidity) in individual eyes greatly influence the resultant applanation force/pressure from ocular mechanics [7, 14, 15], giving a large measurement variation that may cover the accuracy of interest (1 mmHg). Moreover, such procedures require care from specialists, implying frequent clinic visits and examination, making it less than ideal for regular (e.g., daily) monitoring of pressure fluctuations and treatment progress. As recent findings suggest that IOP spikes from diurnal fluctuations should be considered as a separate risk factor to optic nerve damage [16–18], new paradigms with continuous IOP tracking capability are being

developed for prompt detection and appropriate treatment in order to provide a different solution to glaucoma management. These considerations together articulate the great need for a direct, convenient, and reliable continuous IOP sensing technology.

1.4 Clinical Procedures for Intraocular Pressure Regulation

Although elevated IOP is only one of the major risk factors of glaucoma, lowering it via pharmaceuticals or surgery is currently the mainstream of effective glaucoma treatment [1–5]. To clarify again, these treatments may save a patient’s remaining vision, but they can not improve his/her sight already lost from glaucoma. Current clinical procedures comprise medicines, surgeries (laser and conventional), or a combination of these. In the U.S., medications are often first prescribed, while laser surgery is often the first line of therapy in Europe, Japan, and Canada.

In terms of drug therapy, there are several different classes of medications to treat glaucoma by lowering IOP, with several different medications in each class (such as adrenergic, alpha agonist, beta blockers, carbonic anhydrase inhibitors, cholinergic (miotic) and prostaglandin analogs to name a few examples [4]). Each of these medicines may have local and/or systemic side effects, as well as potential patient refractoriness to the drug composition. The medication treatment is typically in the form of eye drops with dosages depending on the severeness of the disease. It inherently causes prescription difficulty due to the lack of effective diagnosis and efficient dosage style, especially at the early detection and treatment stage. In addition, because glaucoma often has no symptoms, people may be tempted to stop taking, or may forget to take, their medicine. As a result, poor compliance with medications and follow-up visits become a

major reason for vision loss in glaucoma patients. Patient education and communication must be ongoing to sustain successful treatment plans using drug therapy for this lifelong disease with no early symptoms.

Surgery therapy involves laser surgery or conventional microsurgery that creates a cut in the eye in order to increase the intraocular fluid drainage blocked by neuropathy from glaucoma so as to reduce the resultant IOP. Laser surgery is performed using a high-intensity beam of light aiming at the lens and reflected onto the meshwork inside the glaucomatous eye. During operation the laser makes several evenly spaced burns that stretch the drainage holes in the trabecular meshwork so that the fluid can be drained more effectively. Conventional microsurgery is utilized when a new fluid drainage path needs to be created at the eye, as shown in Figure 1-8 [3]. Depending on different surgical locations determined by an ophthalmologist, different surgeries such as canaloplasty and trabeculectomy can be performed [5]. These created openings also facilitate the fluid being drained out of the eye more effectively. Overall the surgery therapy offers a high success rate (60%–80%) at lowering the IOP. However, it is only a temporary solution and its effects can wear off in the long term as the wound/opening will heal over time. Further treatment, even including repeated procedures, may need to be conducted for lifelong glaucoma management, while surgical and post-operative complications such as eye infection and inflammation are a serious concern.

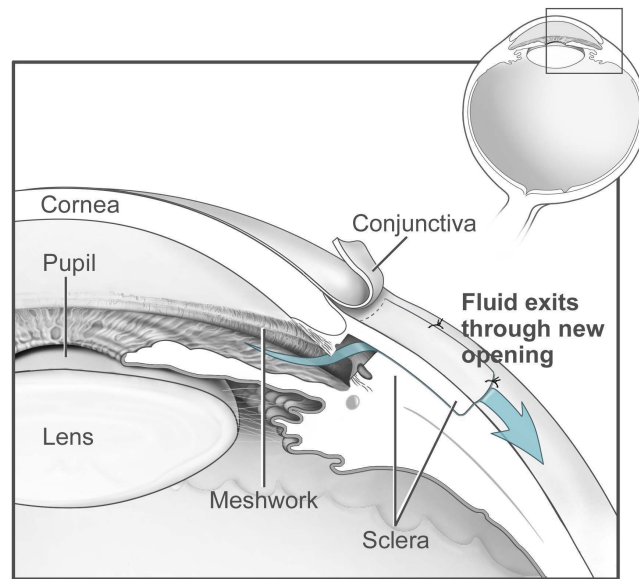


Figure 1-8: Improvement of intraocular fluid drainage by surgery therapy. Drawing courtesy of National Eye Institute.

Given that improving intraocular fluid drainage is still the most effective known solution to glaucoma treatment and that continuous regulation should be realized to avoid fluid re-accumulation, the concept of an artificial drainage path using implants has been proposed. An implant device is positioned at the surgically created drainage opening so that the drainage path will remain even when the wound is healed. This implant therapy can achieve the same functionality of lowering IOP as standard surgery therapy, while the effective duration of treatment can be extensively prolonged, suitable for lifelong glaucoma management. Generally, such implants or glaucoma drainage devices (GDDs) embody a through tube to shunt the fluid in a path similar to that shown in Figure 2-8. GDDs have been developed over the last 100 years (since 1907 [19–22]). State-of-the-art examples are shown in Figure 1-9 in non-valved (Molteno and Baerveldt) and valved (Krupin and Ahmed) designs, and the typical implantation configuration is represented in

Figure 1-10. The flow tube is inserted into the anterior chamber and the plate is implanted at the subconjunctiva (i.e., underneath the conjunctiva) to allow the fluid flow out of the eye into a chamber called a bleb. However, the existing implant therapy faces challenge of systematically controlling the fluid outflow. No set threshold point can be reliably achieved for tube shunt opening and closing even in valved implants, leading to excessive fluid drainage and hypotony where the IOP drops lower than 5–10 mmHg—obviously a failure mode in implant operation. Other than that, surgical/biological compliance of these alien devices in the intraocular environment is also a critical issue. Possible surgical and post-operative complications include tissue inflammation and scarring as well as clogging of the tube implant. Trade-off appears to be related to the size of the implant: The larger the amount of the effective implant volume, the higher likelihood of drainage success and length of operation time, but the greater chance of accompanied complications. With these considerations, a new implant paradigm needs to be developed for reliable IOP regulation with minimal complications. Although this thesis emphasizes development of implantable MEMS pressure sensors and corresponding wireless IOP sensing technology, the concept of a MEMS-implant-based approach for continuous and systematic IOP regulation is also proposed in Chapter 2, with preliminary experimental demonstrations and verifications presented in Chapter 5 as a supplement addressing the feasibility of the proposed solution in light of the aforementioned issues and challenges.

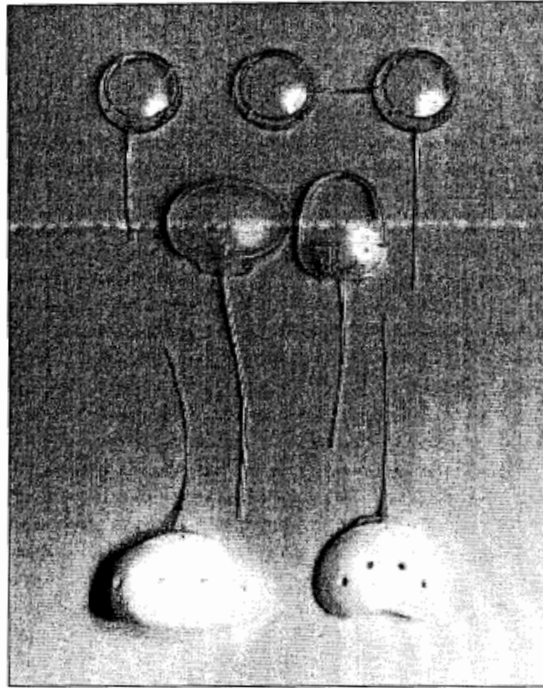


Figure 1-9: State-of-the-art GDDs. (top row) Single- and double-plate Molteno implants. (middle row) Krupin slit valve and Ahmed glaucoma valve. (bottom row) 350 mm² and 250 mm² Baerveldt glaucoma implants. Image reprinted from [22].

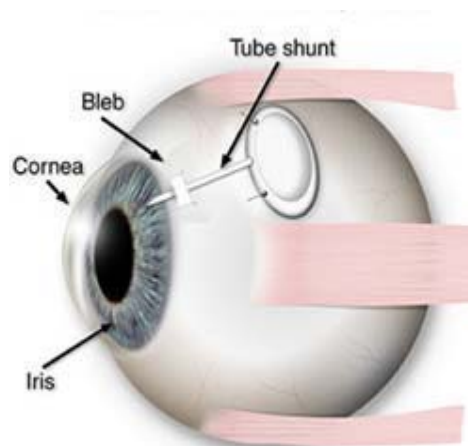


Figure 1-10: Glaucoma tube shunt implantation. Illustration courtesy of EyeMDLink.com.

1.5 Summary

This chapter describes the clinical problems of the ocular disease glaucoma and its physiological relation with intraocular pressure (IOP) of the eye. It shows that successful glaucoma management is highly dependent on accurate and reliable IOP monitoring and regulation. The clinical diagnosis and treatment procedures presented here are effective and widely utilized nowadays, but they may not be sufficient to manage this lifelong chronic disease, as studies show that patients can still experience loss of vision even in the care of ophthalmologists. New approaches to continuous/real-time IOP monitoring and regulation are therefore needed to improve the current situation so that early detection and appropriate treatment of glaucoma can be better managed.

1.6 Bibliography

- [1] J. E. Cairns, Ed., *Glaucoma*, Orlando, FL: Grune & Stratton, 1986.
- [2] M. Sherwood, "Glaucoma," in *Ophthalmology*, 2nd ed., M. Yanoff and J.S. Duker, Eds., St. Louis, MO: Mosby, pp. 1413–1473, 2004.
- [3] National Eye Institute, "Glaucoma," http://www.nei.nih.gov/health/glaucoma/glaucoma_facts.asp (accessed: Jul. 2, 2008).
- [4] Glaucoma Research Foundation, <http://www.glaucoma.org/> (accessed: Jul. 2, 2008).
- [5] Wikipedia, "Glaucoma," <http://en.wikipedia.org/wiki/Glaucoma> (accessed: Jul. 2, 2008).
- [6] Eyesight, http://eyelightphoto.blogspot.com/2007_04_01_archive.html (accessed: Jul. 2, 2008).
- [7] C.R. Ethier, M. Johnson, and J. Ruberti, "Ocular biomechanics and biotransport," *Annu. Rev. Biomed. Eng.*, vol. 6, pp. 249–273, 2004.
- [8] R. F. Brubaker, "Flow of aqueous humor in humans," *Invest. Opth. Vis. Sci.*, vol. 32, pp. 3145–3166, 1991.
- [9] D. Cline, H. W. Hofstetter, and J. R. Griffin, Eds., *Dictionary of Visual Science*, 4th ed., Boston, MA: Butterworth-Heinemann, 1997.
- [10] R. A. Moses, "The Goldmann applanation tonometer," *Am. J. Ophthalmol.*, vol. 46, no. 6, pp. 865–869, Dec. 1958.
- [11] N. Ducrey, J. Geinoz, and R. Faggioni, "Non-contact applanation tonometry," *Ophthalmologica*, vol. 170, pp. 446–449, 1975.

- [12] H. Cao, "Pressure sensors," in *Minimally Invasive Medical Technology*, J. G. Webster, Ed., Philadelphia, PA: Institute of Physics Publishing, pp. 33–45, 2001.
- [13] Glaucoma, <http://www.lea-test.fi/en/eyes/glaucoma.html> (accessed: Jul. 2, 2008).
- [14] P. A. Tonnu, T. Ho, A. El Sheikh, K. Sharma, E. White, C. Bunce, and D. Garway-Heath, "The influence of central corneal thickness and age on intraocular pressure measured by pneumotonometry, noncontact tonometry, the Tono-Pen XL, and Goldmann applanation tonometry," *Brit. J. Ophthalmol.*, vol. 89, pp. 851–854, 2005.
- [15] I. G. Pallikaris, G. D. Kymionis, H. S. Ginis, G. A. Kounis, and M. K. Tsilimbaris, "Ocular rigidity in living human eyes," *Invest. Ophth. Vis. Sci.*, vol. 46, pp. 409–414, 2005.
- [16] S. Asrani, R. Zeimer, J. Wilensky, D. Gieser, S. Vitale, and K. Lindenmuth, "Large diurnal fluctuations in intraocular pressure are an independent risk factor in patients with glaucoma," *J. Glaucoma*, vol. 9, pp. 134–142, 2000.
- [17] E. Hughes, P. Spry, and J. Diamond, "24-hour monitoring of intraocular pressure in glaucoma management: a retrospective review," *J. Glaucoma*, vol. 12, pp. 232–236, 2003.
- [18] R. Puers, G. Vandevoorde, and D. D. Bruyker, "Electrodeposited copper inductors for intraocular pressure telemetry," *J. Micromech. Microeng.*, vol. 10, pp. 124–129, 2000.
- [19] K. S. Lim, B. D. S. Allan, A. W. Lloyd, A. Muir, and P. T. Khaw, "Glaucoma drainage devices: Past, present, and future," *Brit. J. Ophthalmol.*, vol. 82, pp. 1083–1089, 1998.

- [20] C.-H. Hong, A. Arosemena, D. Zurakowski, and R. S. Ayyala, "Glaucoma drainage devices: A systematic literature review and current controversies," *Surv. Ophthalmol.*, vol. 50, pp. 48–60, 2005.
- [21] R. S. Ayyala, J. Laursen Duarte, and N. Sahiner, "Glaucoma drainage devices: State of the art," *Expert Rev. Med. Dev.*, vol. 3, pp. 509–521, 2006.
- [22] K. S. Schwartz, R. K. Lee, and S. J. Gedde, "Glaucoma drainage implants: A critical comparison of types," *Curr. Opin. Ophthalmol.*, vol. 17, pp. 181–189, 2006.

CHAPTER 2

MEMS IMPLANT APPROACHES FOR INTRAOCULAR PRESSURE MONITORING AND REGULATION

2.1 MEMS Implant Approach for Intraocular Pressure Monitoring

In order to fulfill continuous IOP monitoring with high fidelity and high accuracy (which is not available using current clinical procedures), information on IOP variations must be obtained directly from the inside of the eye and be registered/accessed at all times—ideally in a 24/7 fashion to accommodate the concerns of current glaucoma detection approaches as described in Chapter 1. These requirements can be met by having a pressure sensor implanted into the eye [1]. As shown in Figure 2-1 for illustration, such a sensor paradigm is designed to be secured on the iris under the

transparent cornea for the best observation from and communication with the outside world. Because of its placement, the pressure sensor can register *in situ* IOP variations in the anterior chamber of the eye. An external reader is exploited to interrogate the sensor and obtain the direct IOP readouts, with the possibility of autonomous recording facilitated by electrical and/or optical transduction from the reader/sensor interaction. The sensor implant is the key component and needs to be highly biocompatible in the intraocular environment. Its form factor also needs to be suitable for minimally invasive implantation to minimize the complexity of surgical procedures. It turns out that MEMS technology and its derivation parylene MEMS technology (described in the Appendix), is the perfect means to address these constraints and ultimately accomplish the proposed application. The developed parylene-based MEMS pressure sensors are designed to be totally implantable, with small characteristic dimension so that no sutures are required for the corresponding small flat incision (< 2 mm) after the surgery. They are a passive sensing scheme, in contrast to active sensing [2, 3] in which power transfer, hermetic packaging, size, and cost of the device are critical concerns. Major design specifications of the proposed sensor implant paradigm to be achieved for practical IOP monitoring are listed in Table 2-1. Depending on different reader implementation, two types of parylene-based MEMS sensor implants having specific core micromechanical structures for electrical [4] and optical [5] wireless sensing are demonstrated in this work. Detailed device design, fabrication, experimental results, and analysis are presented in the following chapters (Chapter 3: electrical sensing; Chapter 4: optical sensing) in order to prove the passive sensor implant concept for continuous IOP monitoring. All associated animal procedures and experiments in this study conformed to the ARVO Statement on

the Use of Animals in Ophthalmic and Vision Research, and were held to the highest ethical standards possible.

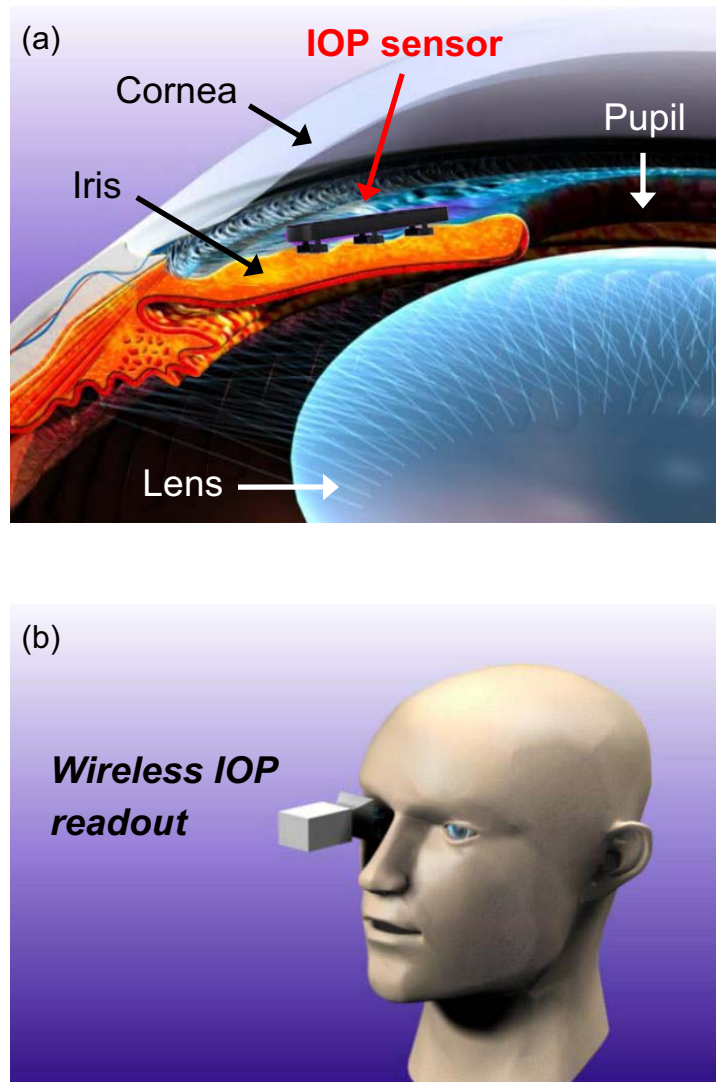


Figure 2-1: Concept of MEMS implant approach for continuous IOP monitoring. (a) Surgical placement of the device implant in the intraocular environment. (b) Wireless IOP sensing with the use of an external reader interrogating the intraocular implant

Table 2-1: Design specifications of the proposed sensor implant paradigm
for practical IOP monitoring

Design item	Specification
Pressure sensing accuracy	1 mmHg
Pressure sensing range	1–50 mmHg
Characteristic length	< 2 mm*
Surgical placement	Anterior chamber (iris)
Biocompatibility	Implantable grade
Sensing method	Wireless; passive
Readout constraint	Autonomous or self-checking (free from clinic visit)
Sensing Distance (Implant-reader distance)	> 1 cm [†]

*Facilitating minimally invasive implantation surgery

[†] Incorporating iris-cornea distance (~ 0.5 cm)

2.2 MEMS Implant Approach for Intraocular Pressure Regulation

The interest in utilizing MEMS technology in this work also covers application of IOP regulation other than IOP monitoring, in the sense of providing alternative approaches to current non-optimal clinical glaucoma management techniques. MEMS technology has been implemented for microfluidics and flow control/transport at the microscale for years [6–8]. The form factor and the operation range of these fabricated microfluidic devices surprisingly match the required specifications of intraocular fluid drainage, enabling their use in implantable microdevices [9]. The MEMS implant approach is based on the conventional GDD concept that the device implant is designed

to be positioned at the subconjunctiva (as shown in Figure 2-2) in order to create the biomimetic drainage path. The intraocular fluid is drained through the implant to the subconjunctiva then eventually diffused away, the same as in the natural drainage path previously shown in Figure 1-5. With micromachining processes the shunt device can be fabricated in a tube shape and in a form factor smaller than a hypodermic needle, so that a minimally invasive needle-based device implantation scheme can be realized. The entire implant is designed to be placed in the intraocular environment with no exposure to the outside world or through the sclera, minimizing the possibility of surgical and post-operative complications of the implantation. Designed tissue anchors (not shown in Figure 2-2) are integrated on the device implant for its suture-less fixation in the intraocular environment. Because of the small incision size, no sutures would be needed after the surgery as the eye will heal spontaneously.

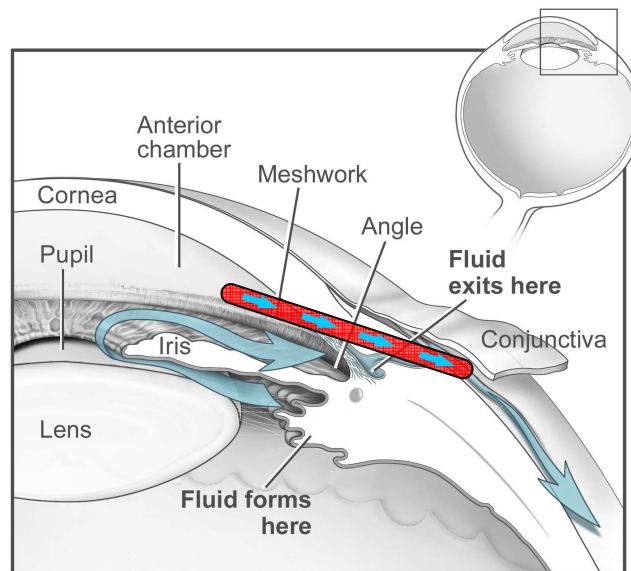


Figure 2-2: Surgical placement of the MEMS implant (highlighted in red). The small arrows indicate fluid drainage direction through the tube implant. Image adapted from Figure 1-5.

The flow control behavior of the MEMS implant is accomplished using a combination of microchannel and microvalve, as in a typical microfluidic device paradigm. Because of its sophisticated microflow control in the miniature pressure/flow rate regime, this combination can achieve more reliable and more controllable intraocular fluid drainage compared to conventional large-scale valved GDDs. The flow can be regulated in a customized pressure-bandpass profile as shown in Figure 2-3, with highlighted low-off and high-off threshold characteristics for safety reasons. For example, the artificial drainage path is closed when the IOP is low (e.g., < 10 mmHg) in glaucoma patients to prevent hypotony. It is also closed when IOP spikes (e.g., 50–80 mmHg) because of routine external interferences, such as rubbing or pressing on the eye, to prevent excessive high-pressure high-flow-rate fluid drainage. Furthermore, this drainage path must be proof to any fluid backflow (i.e., from outside to the anterior chamber of the eye through the implant) for biological/medical considerations. These features can be further adapted in all biomedical flow controls for safe and effective regulation within a range of interest. This approach is implemented in a passive-valved configuration to demonstrate a non-electronic and power-free implant. The passive paradigm is advantageous in many aspects compared with actively powered valves, in which design complexity, actuation implementation, power consumption, form factor, and/or integration capability is a major concern. As stated previously, the parylene MEMS technology can be applied here as well to pursue fully biocompatible implants while achieving required structural and fluidic performance from such micromechanical devices. Major design specifications of the proposed sensor implant paradigm to be achieved for practical IOP regulation are listed in Table 2-2. The correspondingly

developed parylene-based MEMS IOP drainage device [10–12] is presented in Chapter 5 with illustrative description of design, fabrication, and experimental results, in order to prove the concept for continuous IOP regulation. Same with the pressure sensors, all associated animal procedures and experiments in this study regarding the drainage devices conformed to the ARVO Statement on the Use of Animals in Ophthalmic and Vision Research, and were held to the highest ethical standards as possible.

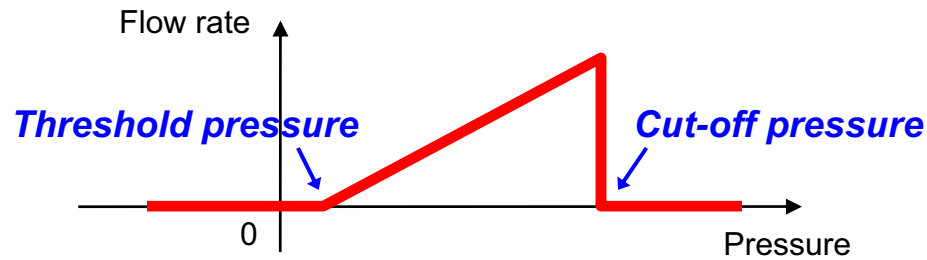


Figure 2-3: Proposed IOP regulation profile of the MEMS implant. The slope in flow conductive region is determined by the practical fluidic resistance of the device.

Table 2-2: Design specifications of the proposed device implant paradigm
for practical IOP regulation

Design item	Specification
Regulated pressure range	10–15 mmHg
Drainage flow rate	1–10 $\mu\text{L}/\text{min-mmHg}$
Regulation method	Spontaneous; passive
Characteristic length	< 0.5 mm*
Surgical placement	Subconjunctiva
Biocompatibility	Implantable grade

*Facilitating needle-based minimally invasive implantation surgery

2.3 Summary

This chapter delivers the concept of utilizing MEMS-based implant paradigms as alternative approaches to current clinical techniques with the intent of providing accurate, reliable, and continuous/real-time IOP monitoring and regulation toward glaucoma detection and drainage. Enabled by MEMS technology and the use of biocompatible polymeric parylene material described in the Appendix, the microfabricated implants can be developed for such ophthalmic applications, including wireless passive IOP sensors with an electrical sensing method presented in Chapter 3, and with an optical sensing method presented in Chapter 4. In addition to the IOP sensing technology, investigations on passive microfluidic IOP drainage devices are also described in Chapter 5 to convey device feasibility and future possibility. These biocompatible, unpowered, micromechanical MEMS implant paradigms are designed to have surgical/biological compliance for minimally invasive implantation and long-term operation in the intraocular environment, as well as ultimately more effective and reliable glaucoma study and management compared with current state-of-the-art medical technologies.

2.4 Bibliography

- [1] K. C. Katuri, S. Asrani, and M. K. Ramasubramanian, "Intraocular pressure monitoring sensors," *IEEE Sens. J.*, vol. 8, pp. 12–19, 2008.
- [2] W. Mokwa and U. Schnakenberg, "Micro-transponder systems for medical applications," *IEEE Trans. Instrum. Meas.*, vol. 50, pp. 1551–1555, 2001.
- [3] W. Mokwa, "Medical implants based on microsystems," *Meas. Sci. Technol.*, vol. 18, pp. R47–R57, 2007.
- [4] P.-J. Chen, D. C. Rodger, S. Saati, M. S. Humayun, and Y.-C. Tai, "Microfabricated implantable parylene-based wireless passive intraocular pressure sensors," *J. Microelectromech. Syst.*, in press.
- [5] P.-J. Chen, D. C. Rodger, R. Agrawal, S. Saati, E. Meng, R. Varma, M. S. Humayun, and Y.-C. Tai, "Implantable micromechanical parylene-based pressure sensors for unpowered intraocular pressure sensing," *J. Micromech. Microeng.*, vol. 17, pp. 1931–1938, 2007.
- [6] A. van den Berg and T. S. J. Lammerink, "Micro total analysis systems: Microfluidic aspects, integration concept and applications," *Top. Curr. Chem.*, vol. 194, pp. 21–49, 1998.
- [7] S. Shoji, "Fluids for sensor systems," *Top. Curr. Chem.*, vol. 194, pp. 163–188, 1998.
- [8] K. W. Oh and C. H. Ahn, "A review of microvalves," *J. Micromech. Microeng.*, vol. 16, pp. R13–R39, 2006.

- [9] B. Bae, K. Park, and M. A. Shannon, "MEMS application of actuators and sensors for glaucoma treatment," in *MEMS/NEMS Handbook: Techniques and Applications*, vol. 5, C.T. Leondes, Ed., New York: Springer, pp. 57–99, 2006.
- [10] P.-J. Chen, D. C. Rodger, S. Saati, J. C. Altamirano, C.-H. Lin, R. Agrawal, R. Varma, M. S. Humayun, and Y.-C. Tai, "Implementation of microfabricated suture-less flexible parylene tissue anchors on minimally invasive biomedical implants," in *Proc. 11th Int. MicroTAS Conf.*, Paris, France, pp. 518–520, Oct. 7–11, 2007.
- [11] P.-J. Chen, D. C. Rodger, E. Meng, M. S. Humayun, and Y.-C. Tai, "Surface-micromachined parylene dual valves for on-chip unpowered microflow regulation," *J. Microelectromech. Syst.*, vol. 16, pp. 223–231, 2007.
- [12] P.-J. Chen, D. C. Rodger, M. S. Humayun, and Y.-C. Tai, "Floating-disk parylene microvalves for self-pressure-regulating flow controls," *J. Microelectromech. Syst.*, in press.

CHAPTER 3

IMPLANTABLE PARYLENE-BASED INTRAOCULAR PRESSURE SENSORS WITH ELECTRICAL READOUTS

3.1 Overview

This chapter presents an implantable, unpowered, parylene-based wireless MEMS pressure sensor for continuous IOP monitoring in an electrical sensing paradigm. It has an electrical LC-tank resonant circuit formed by an integrated capacitor and an inductor coil to facilitate passive wireless sensing with the use of an external interrogating coil on a reading apparatus. The first version of the surface-micromachined sensor is in two designs involving variable capacitor and variable capacitor/inductor resonant circuits to realize the pressure-sensitive components. The sensor is monolithically microfabricated

by exploiting parylene as a biocompatible structural material in a suitable form factor for minimally invasive intraocular implantation. Pressure responses of the microsensor have been characterized on-chip to demonstrate its high pressure sensitivity in both sensor designs. A 6-month animal study verifies the *in vivo* bioefficacy and biostability of the sensor implant in the intraocular environment with no surgical or post-operative complications. After incorporating improvements of sensor design and readout method, the second version of the device implant successfully meets engineering and surgical specifications with enhanced performance for practical IOP measurements through on-bench and *in vivo* experimental verifications. This sensor will ultimately be implanted on the iris of the eye to fulfill continuous, convenient, direct, and accurate IOP monitoring.

3.2 Implant Design

3.2.1 Background

Passive telemetric sensing has been widely used as one of the viable methods to accomplish continuous and accurate non-contact IOP measurements [1, 2]. This methodology enables straightforward IOP sensing by utilizing a transensor implant that registers environmental pressure variations inside the eye, so that the IOP can be directly measured by using an external reader wirelessly interrogating the implant. In contrast to active sensing in which power transfer, size, and cost of the device are critical concerns [3, 4], passive telemetric sensing has relatively flexible design considerations on the device side [5]. The first paradigm using this sensing method was reported in 1967 [6] when a capsulated sensor having an electrical LC-tank resonant circuit was implanted to the anterior chamber of the eye for IOP monitoring. With recent progress in

microelectromechanical systems (MEMS) technology, miniaturized pressure sensors [7–11] (such as those shown in Figure 3-1) have been developed using the LC resonant circuit concept and the enabling microfabrication technologies for various wireless sensing of physiological parameters: including transcutaneous pressure monitoring, intracranial pressure monitoring, and pressure monitoring of abdominal aortic aneurysms (AAA), in addition to the proposed IOP monitoring application.

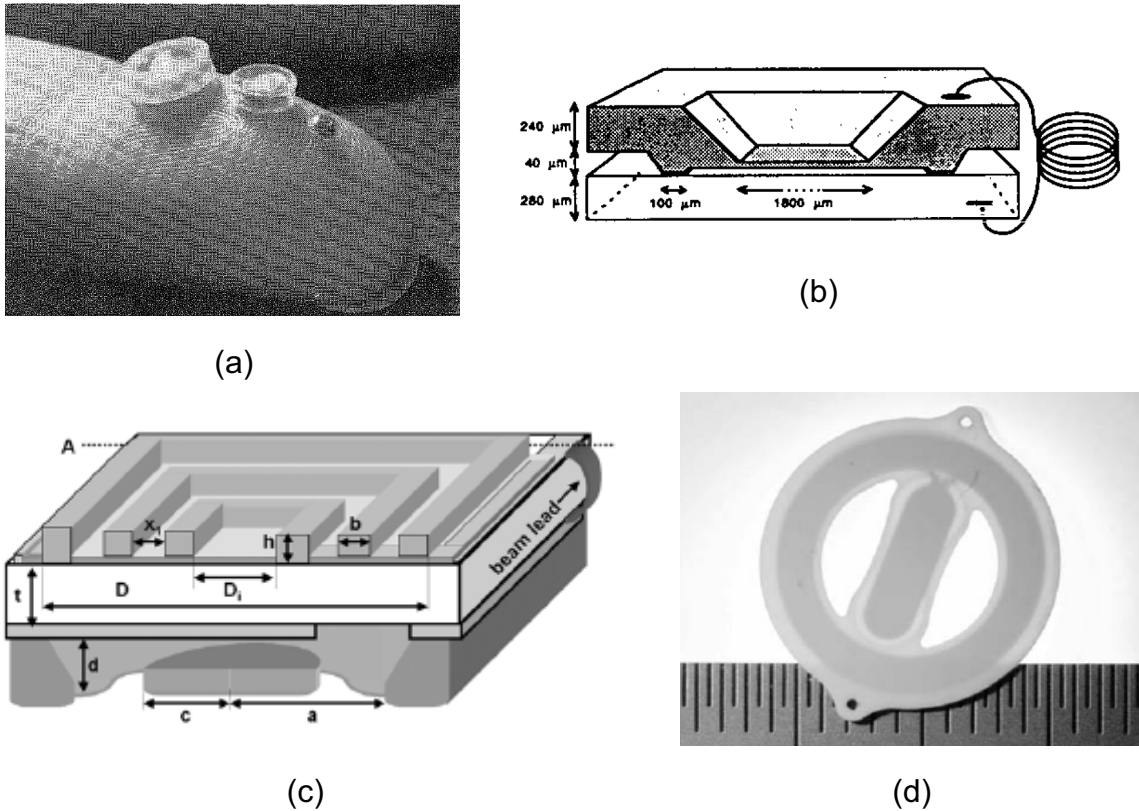


Figure 3-1: Wireless passive MEMS pressure sensors for physiological parameter measurements in literature. (a) Device for IOP sensing [6]. (b) Device for IOP sensing [7]. (c) Device for transcutaneous pressure sensing [9]. (d) Device for aortic aneurysms pressure sensing [11]

These reported devices serve as excellent examples showing the potential for using such wireless passive pressure transensors for continuous measurement of physiological parameters in biomedical systems and human healthcare. The theory and model of wireless LC sensing have been well established, given the development of these reported pressure microsensors. On the technology side, however, all these MEMS devices to date involve delicate multiple wafer fabrication procedures, with wafer bonding as the essential process to create the pressure-sensitive chamber of the variable capacitor. This creates challenges in adapting them to intraocular implants due to the small available space in the anterior chamber of the eye. Consequently, by exploiting parylene in integrated surface-micromachined capacitive sensors [12], a monolithically microfabricated parylene-based wireless passive pressure sensor is developed having a form factor suitable for minimally invasive device implantation and placement at the pars plana or on the iris of the eye. Along with engineering specifications, design considerations are also focused on compatibility with surgical procedures to minimize complexity and time of operation for ease of device implantation in practice. Featuring parylene as the biocompatible polymeric material, the pressure sensor is designed to be completely implantable in the intraocular environment so that long-term continuous IOP monitoring of glaucoma patients becomes practical.

3.2.2 Sensing scheme

The concept of the wireless IOP sensing system in the passive electrical sensing scheme is shown in Figure 3-2, and the associated glasses-type reader paradigm is proposed as shown in Figure 3-3 for autonomous and continuous monitoring in practice. The sensor implant is designed to have an electrical LC-tank resonant circuit with a corresponding resonant frequency represented as

$$f_s = \frac{1}{2\pi} \sqrt{\frac{1}{L_s C_s} - \frac{R_s^2}{L_s^2}} \cong \frac{1}{2\pi \sqrt{L_s C_s}} \quad \text{if } R_s^2 \ll \frac{L_s}{C_s}, \quad (3.1)$$

where L_s , C_s , and R_s are respectively the inductance, capacitance, and resistance of the sensor. Using an external coil to build an inductive coupling link with the implanted sensor, the equivalent impedance viewed from the measurement instrument can be derived using circuit analysis as [11–13]

$$Z_{eq} = \frac{V}{I} = j2\pi f L_r \left[1 + k^2 \frac{\left(\frac{f}{f_s}\right)^2}{1 - \left(\frac{f}{f_s}\right)^2 + \frac{1}{Q_s} j \frac{f}{f_s}} \right], \quad (3.2)$$

where V and I are the exciting voltage and current across the reader coil, f is the excitation frequency, $Q_s = R_s^{-1}(L_s C_s^{-1})^{1/2}$ the quality factor of the sensor at resonance, and k is the coupling coefficient of the inductive link (totally dependent on physical geometries such as the planar size of the sensor and reader coils, and the separation distance between the coils [9–13]. Therefore, from (3.2), a phase-dip technique can be applied to wirelessly detect the resonant frequency of the sensor as the phase of the complex impedance Z_{eq} drops to the minimum in the frequency scan from the

measurement instrument—such as an impedance analyzer, network analyzer, or other involving customized electronics. When the sensor is excited at resonance, Z_{eq} becomes

$$Z_{eq} = j2\pi f_s L_r (1 + jk^2 Q_s), \quad (3.3)$$

and its phase dip magnitude can be approximated as

$$\Delta\phi \cong \tan^{-1}(k^2 Q_s). \quad (3.4)$$

As long as the impedance phase dip is detectable in the frequency scan, the resonant frequency of the sensor can be accurately characterized. As a result, if the sensor implant has pressure-sensitive electrical components, its resonant frequency will be shifted based on external pressure variation, thus registering the *in situ* environmental pressure. This change can be interrogated using the external reader coil to accomplish continuous wireless IOP monitoring.

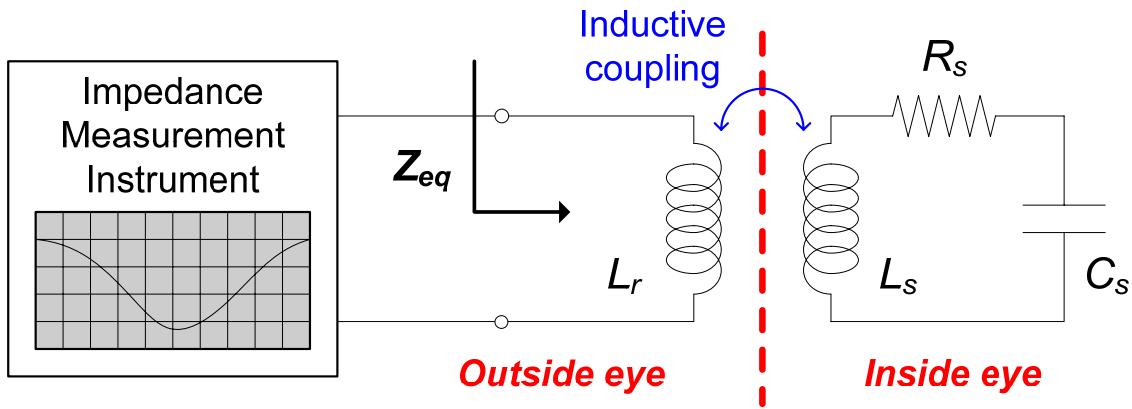


Figure 3-2: Passive wireless IOP sensing concept. The implanted sensor can faithfully register pressure variations using corresponding electrical characteristic changes, which are measured using an external reader through a wireless inductive coupling link.

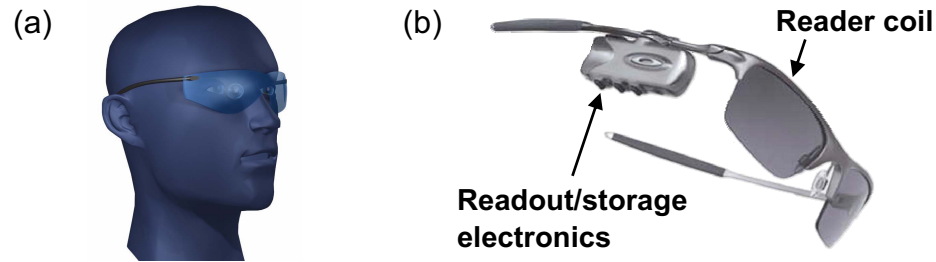


Figure 3-3: Proposed IOP monitoring in practice. (a) Autonomous and continuous sensing using glasses reader paradigm. (b) Integrated reader components on the frame

3.2.3 Sensor design

The pressure sensor is designed as illustrated in Figure 3-4 to facilitate the passive wireless pressure sensing scheme. It comprises a flexible diaphragm chamber integrated with parallel metal plates as an integrated capacitor and surrounding metal wires as a planar inductor to create the resonant circuit that communicates with the external reader. A dual-layer metal structure is employed to increase the overall inductance of the coil in the given device area. In the surgical design aspect, the device has a rectangular in-plane contour to minimize the required incision size during implantation, along with smooth edges to prevent tissue irritation in the intraocular environment. Suture holes are located at both ends of the device for convenience in implant anchoring.

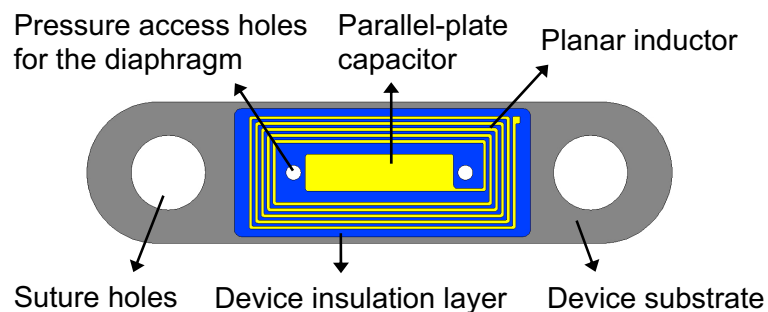


Figure 3-4: Pressure sensor design (top view). The flexible diaphragm on top of the device area as the movable structure is not shown in this planar illustration.

In the engineering design aspect, the electrical characteristics of the sensor can be determined by using the following equations [8, 14, 15]. The inductance of the dual-layer planar inductor in rectangular conformation can be calculated as

$$L_s \cong L_{s,top} + L_{s,bot} + 2M, \quad (3.5)$$

where $L_{s,top}$ and $L_{s,bot}$ are inductances, respectively, from top and bottom metal layers as

$$\begin{aligned} L_{s,top} = L_{s,bot} = & 0.02339n^2 \left[(s_1 + s_2) \log \left(\frac{2s_1s_2}{nD} \right) - s_1 \log(s_1 + g) - s_2 \log(s_2 + g) \right] \\ & + 0.01016n^2 \left[2g - \frac{(s_1 + s_2)}{2} + 0.447nD \right] \\ & - 0.01016n(s_1 + s_2)(A + B) \text{ (}\mu\text{H)}, \end{aligned} \quad (3.6)$$

where n is the number of turns of the inductor, s_1 and s_2 are the average lengths of two sides of the inductor (in), $g = \sqrt{s_1^2 + s_2^2}$ (in), D is the distance of the planar metal line separation plus metal line width (in), and A and B are constant coefficients determined by the winding geometry and the number of turns of the coil. The mutual inductance M is generated by intrinsic magnetic coupling between the top and bottom metal wires of the inductor and can be calculated as

$$M = 0.00254l \left[2.303 \log \left(\frac{l}{g} \right) - 1 + \frac{2g}{l} \right] \text{ (}\mu\text{H)} \text{ if } l \gg g, \quad (3.7)$$

where l is the total length of the dual-layer metal wires ($l/2$ for each layer) (in), and g is the separation distance between the top and bottom metal layers of the inductor (in). The integrated inductor imperatively has a series resistance dominating R_s , and its value with consideration of the high-frequency skin effect can be calculated as

$$R_s = \frac{\rho l}{w \delta \left(1 - e^{-h/\delta}\right)}, \quad (3.8)$$

where ρ is the electrical resistivity of the metal, w and h are the metal line width and height, respectively, and δ is the frequency-dependent metal skin depth given by

$$\delta = \sqrt{\frac{\rho}{\pi f \mu}}, \quad (3.9)$$

where μ is the magnetic permeability of the metal. Finally, the capacitance of the sensor can be expressed as

$$C_s = C_{s,g} + C_{s,p}, \quad (3.10)$$

where $C_{s,g}$ is the capacitance determined by the integrated parallel metal plates with a gap separation at center of the sensor, and $C_{s,p}$ is the parasitic/stray capacitance generated by the other components in the entire device. It is clear from (3.5)–(3.7) and (3.10) that the electrical characteristics of the sensor can vary with respect to geometrical changes in the movable structures. Therefore, a deformable free-standing diaphragm embedding electrical components is employed to realize the transensor device. The deformation profile of a rectangular diaphragm with four fixed edges under a pressure loading can be estimated as in [16], where in the case of small deflection the maximum diaphragm deformation at the center can be calculated by [17]

$$y_{\max} = \left[\frac{C_1 a^4}{D} \right] \Delta P, \quad (3.11)$$

where ΔP is the pressure difference across the diaphragm, a is half the length of the short edge of the rectangular diaphragm, $D = Et^3 / [12(1-\nu^2)]$ the flexural rigidity of the

diaphragm in which E is Young's modulus and ν is Poisson's ratio of the material, t is the diaphragm thickness, and C_1 is a constant coefficient determined by geometry and boundary conditions of the diaphragm. In a large deflection case where the assumption ($y \ll t$) is not valid, y_{\max} is calculated using the load-deflection relationship as [18, 19]

$$\left(\frac{C_2\sigma t}{a^2}\right)y_{\max} + \left(\frac{C_3Et}{a^4}\right)y_{\max}^3 = \Delta P, \quad (3.12)$$

where σ is residual stress of the diaphragm, and C_2 and C_3 are constant coefficients determined by geometry and material property (Poisson's ratio) of the diaphragm. Incorporating such an electrical-mechanical-coupled effect, a pressure-sensitive variable capacitor can be realized, as shown in Figure 3-5, by arranging the bottom plate on the substrate and the top plate in the diaphragm. Additionally, instead of having a fixed inductor surrounding the variable capacitor, a variable inductor can be realized by embedding the top metal wire layer in the diaphragm to alter the intrinsic mutual inductance of the dual-layer inductor for further enhanced overall pressure sensitivity. These two sensor designs are implemented on a monolithic substrate with the use of surface-micromachining technology, so as to have less fabrication complexity compared with wafer bonding technology. The pressure reference can be encapsulated inside the diaphragm chamber after sealing the backside of the device at a constant pressure for gauge pressure sensing. All device structures—including oxidized and parylene-coated silicon substrate, titanium/gold metal lines and plates, and the flexible parylene diaphragm—have sufficient biocompatibility to ensure the feasibility and reliability of long-term operation of the device implant in the intraocular environment. The dielectric behavior of parylene (dielectric constant ~ 2.95 at 1 MHz) also favors its use as an

insulator between metal layers. Given the aforementioned models and materials, the overall sensing performance can be estimated to meet the required specification of minute pressure variation measurement (± 1 mmHg) for accurate IOP monitoring.

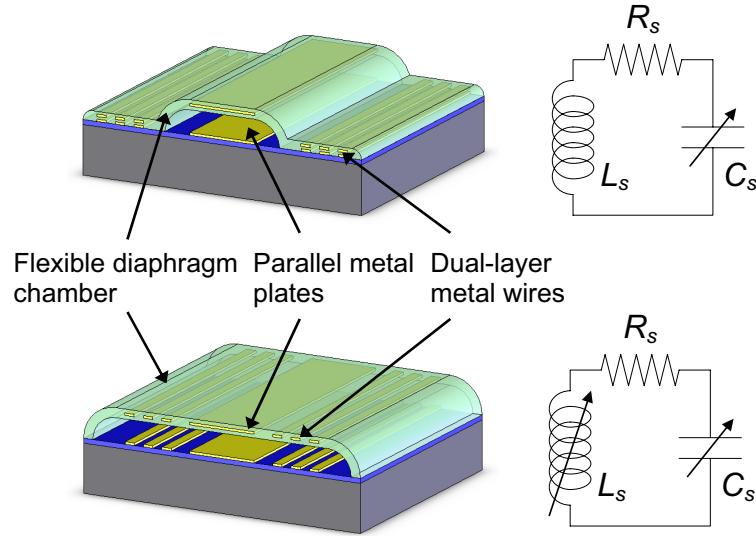


Figure 3-5: Sensor design (cross-sectional view; not to scale) in variable capacitor (top) and variable capacitor/inductor (bottom) variations. The deformable diaphragm chamber with respect to pressure changes realizes pressure-sensitive characteristics of the sensors.

3.3 Device Fabrication

The fabrication process of the wireless pressure sensor is illustrated in Figure 3-6. It began with thermally growing and patterning 0.75- μm -thick oxide on a double-side-polished (DSP) silicon wafer using buffered hydrofluoric acid (BHF, Transene Company Inc., Danvers, MA) and photoresist as the mask. AZ series photoresist (Clariant Corp., Charlotte, NC) was used in this step and in the rest of the microfabrication processes. The frontside oxide insulates the surface-micromachined structures from the silicon substrate, and the backside oxide defines the recess and release boundaries of the device.

A titanium/gold ($200 \text{ \AA}/2 \text{ }\mu\text{m}$) layer was deposited using e-beam evaporation and patterned using standard metal etching techniques to form the bottom half of the electrical components of the sensor. Thick metals are preferred in order to reduce the overall electrical resistance of the metal lines. Although metals with higher thickness could be deposited using electroplating, evaporated metals were used because of their superior material quality for implant use and fabrication compatibility with subsequent surface-micromachining processes. A parylene layer was then coated on the bottom metal of the sensor in the variable capacitor design for insulation purposes between the dual-layer metal wires, while an air gap was used for the sensor in variable capacitor/inductor design. Parylene deposition was conducted in a PDS 2010 Labcoater™ system (Specialty Coating Systems, Inc., Indianapolis, IN). A via for metal contact was created in the parylene layer after patterning it using oxygen plasma and photoresist as the mask. A sacrificial layer of photoresist was then coated and patterned on the wafers so as to define the enclosed space of the pressure-sensitive diaphragm chamber. Gas-phase xenon difluoride (XeF_2 , Nesca Corp., Pretoria, South Africa) silicon roughening was preformed for physically strengthened adhesion between the final surface-micromachined structures and the substrate [20]. Afterwards, sandwiched parylene-metal-parylene layers were deposited and patterned, including another e-beam-evaporated titanium/gold ($200 \text{ \AA}/0.5 \text{ }\mu\text{m}$) layer to realize the flexible diaphragm chambers with variable capacitor or variable capacitor/inductor structures by having different patterns of the sacrificial photoresist layer in different sensor designs. Finally, the devices were released after performing a silicon deep-reactive-ion etching (DRIE) in a PlasmaTherm™ SLR system (Unaxis Inc., St. Petersburg, FL) on the backside of the

wafer, followed by photoresist stripping with acetone. Backside recesses and through-holes as necessary features were also created after DRIE. Supercritical carbon dioxide (CO_2) drying in an Autosamdri-815™ system (Tousimis Research Corp., Rockville, MD) was used to eliminate stiction of the free-standing parylene-metal-parylene diaphragm. Figure 3-7 shows the microfabricated parylene-based pressure sensors in both designs, in a form factor smaller than $4 \text{ mm} \times 2 \text{ mm} \times 1 \text{ mm}$, suitable for intraocular implantation.

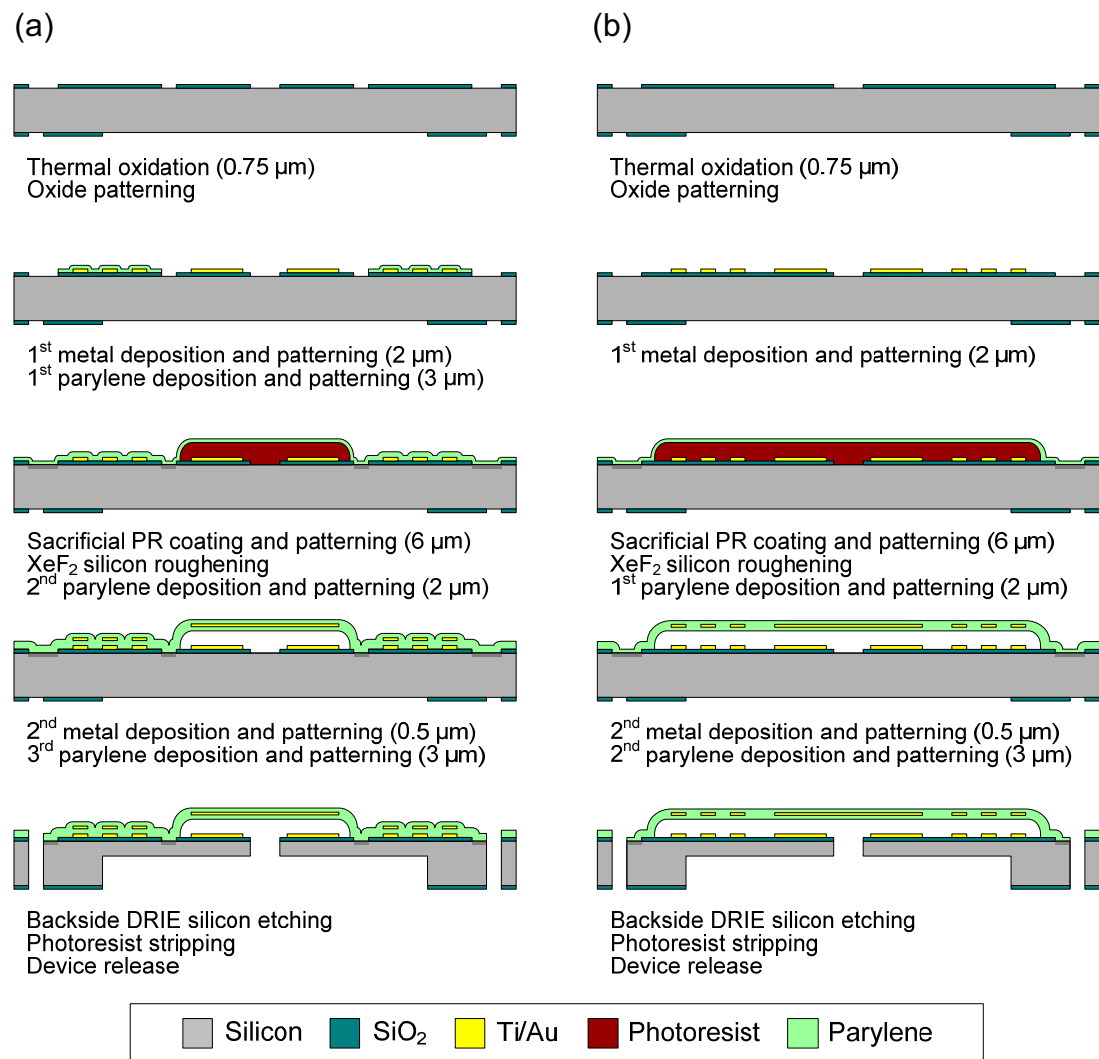


Figure 3-6: Fabrication process flow of microsensors. (a) Variable capacitor design. (b)

Variable capacitor/inductor design

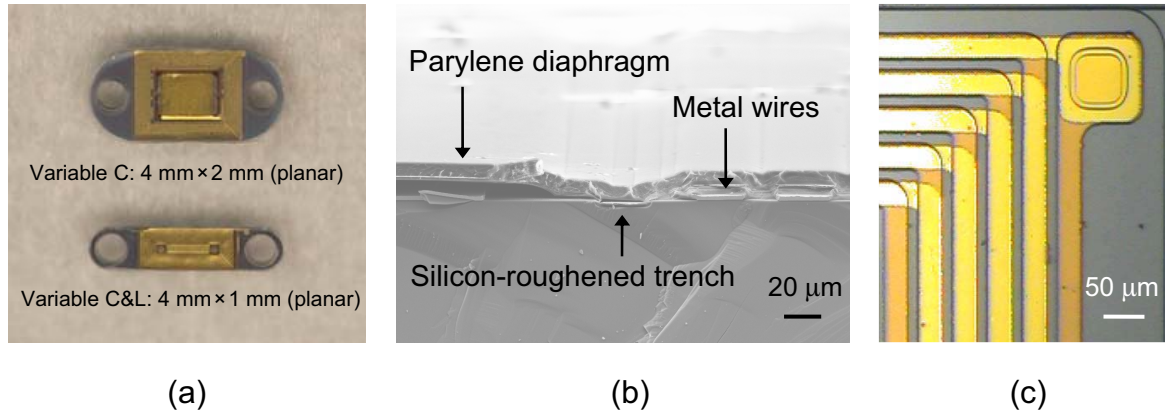


Figure 3-7: Images of microfabricated devices. (a) Full-scale photograph of the sensors (top view). (b) SEM image of the sensor (cross-sectional view). (c) Micrograph of the sandwiched metal-parylene-metal structure showing the inductor wiring and the via (top view). (b) and (c) are images of the sensor in variable capacitor design as example.

In order to achieve both successful device release and packaging, a special two-step etch mask consisting of oxide and photoresist was used for the backside DRIE. By controlling the heights of this two-step mask and the associated etch time, a backside recess was formed on the substrate along with through-wafer etches at locations of the photoresist release holes beneath the parylene diaphragm chamber, the end suture holes, and the release boundaries of the device. The backside recess enables gauge pressure sensing of the devices. For gas-sealed MEMS gauge pressure sensors, the change of encapsulated pressure reference due to diaphragm deflection and corresponding change of volume should be considered [21], as illustrated in Figure 3-8. Derived from the ideal gas law, the increase of the pressure reference can be written as [10]

$$\Delta P_0 = \frac{nRT}{V_0 - \Delta V} - P_0, \quad (3.13)$$

where n is the number of moles of gas/air particles, R is the universal gas constant, T is the environmental temperature, ΔV is the magnitude of change of volume, and V_0 and P_0 are the originally encapsulated volume and pressure of the sensor. As a result, the change of reference pressure would influence the diaphragm deflection and the resultant pressure-sensing behavior, thus it needs to be reduced if it is comparable with the pressure difference to be measured. For the microsensors fabricated in this work, a large gas volume can be encapsulated inside the device after sealing the 250- μm -deep backside recess in addition to that from the surface-micromachined diaphragm chamber, which effectively increases the resultant pressure sensing capacity after packaging.

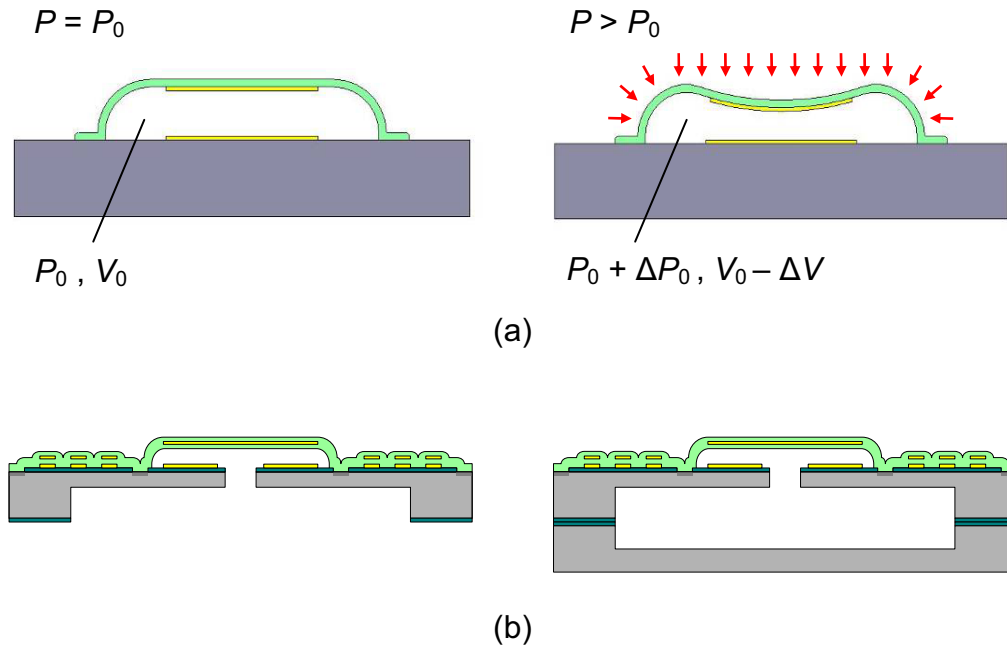


Figure 3-8: Volume change effect in gas-sealed MEMS gauge pressure sensors. (a) The encapsulated gas volume and pressure is variable due to diaphragm deformation. (b) Method to reduce such effect by attaching the sensor back-to-back to a non-electric piece to increase the reference volume V_0 (variable capacitor design as example).

For demonstration purposes, the fabricated sensor device in this work was attached back-to-back to a non-electronic parylene-coated silicon piece with identical geometrical dimensions under atmospheric pressure (1 atm) at room temperature. The influence on pressure sensing from such volume change effect could then be controlled to less than 100 ppm/mmHg, insignificant compared with the results from designed compliant diaphragm deflections. The overall device thickness can definitely be trimmed by thinning down the silicon pieces during fabrication to result in a smaller device size if required. After packaging, a thin conformal parylene layer was selectively coated on the entire device to enhance its biocompatibility for medical use.

3.4 Characterization Results

The microfabricated devices were tested on-bench, *ex vivo*, and *in vivo* to characterize their electrical, physical, and surgical/biological behaviors. During testing a HP 4195A network/spectrum analyzer (HP/Agilent Technologies Inc., Santa Clara, CA) under standard settings was utilized in connection with a 1.5-mm-diameter hand-wound coil made out of standard insulated copper wire to serve as the external reader for the wireless sensing demonstration. Measured equivalent impedance spectra data were stored in a personal computer using the LabVIEW™ program (National Instruments Corp., Austin, TX) for pressure measurement analysis. Testing results are described in the following sections.

3.4.1 Electrical characterization

Electrical parameters of the sensors were first obtained by analyzing the measurement data from both the actual devices with the external readout method and several testing structures through on-chip probing. Table 3-1 lists the experimental results, which were in good agreement with theoretical calculations. The resistance, inductance, and capacitance of the sensor in variable capacitor design were all higher than that of the sensor in variable capacitor/inductor design due to a larger device area. The dual-layer metal wires in proximity across the parylene dielectric in the variable capacitor design gave substantial stray capacitance to the sensor.

Table 3-1: Measured electrical parameters of the microfabricated pressure sensors

	Variable C	Variable C&L
Inductance	0.78 μH	0.36 μH
Capacitance	7.4 pF	3.1 pF
Resistance at resonance	112 Ω	72 Ω
Resonant frequency	~ 62 MHz	~ 150 MHz
Quality factor	~ 3	~ 5

Although the low quality factor ($Q_s < 10$) and small integrated coil size of the sensors fundamentally limits the sensing distance of the wireless system, the sensor signal was still detectable (as shown in Figure 3-9), which validates the feasibility of the impedance phase-dip measurement technique as the sensing scheme. Being different from the ideal case, the phase of the impedance Z_{eq} dipped to the minimum at the frequency f_{\min} , which is highly correlated to f_s and can be expressed as [13]

$$f_{\min} = f_s \left(1 + \frac{k^2}{4} + \frac{1}{8Q^2} \right), \quad (3.14)$$

while the discrepancy was less than 1% given the negligible term from the small coil coupling coefficient effect compared with the term from the quality factor effect in this work. The maximum sensing distance where the phase dip $\Delta\phi < 0.1^\circ$, determined by the noise floor from the testing system, was confirmed to be approximately 2 mm for both sensor designs. Other than reader optimization, the following strategies directly related to sensor development can be implemented to improve the sensing distance and should be included: 1) increase the integrated coil size and the planar geometry ($k \uparrow$); 2) increase the metal wire thickness ($R_s \downarrow$); 3) increase the insulating oxide thickness and/or modify the substrate material ($C_s \downarrow$); and 4) include ground shield patterns [22] which can be potentially utilized as inductor interlayer shield patterns ($C_s \downarrow$).

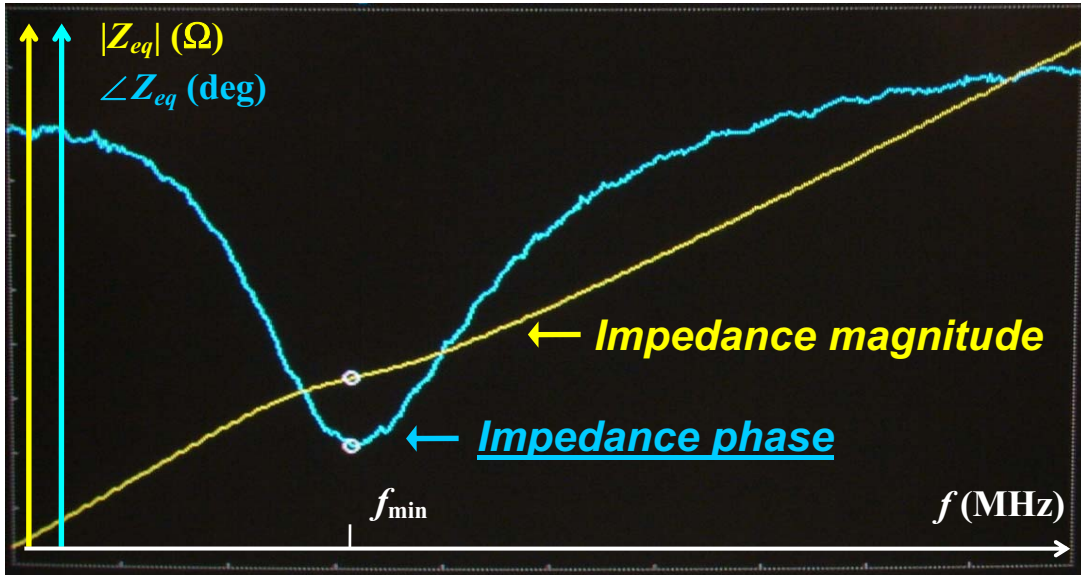


Figure 3-9: Representative captured frequency scan of the equivalent impedance Z_{eq} of the reader coil coupled with the microsensor

3.4.2 On-bench pressure sensing test

After electrical characterization the sensors were tested on-chip to measure their pressure responses. Pressure differences were generated by supplying pressurized air to the inside of the sensor diaphragm chamber through a customized packaging jig connected to a controllable pressure regulation system (as shown in Figure 3-10) with constant environmental pressure outside the diaphragm chamber. A commercial off-chip pressure regulator and a pressure gauge were used to control the pressurization with 0.5 mmHg tuning resolution. The external reader coil was aligned above the packaged device on the same axis using a manipulation stage for *in situ* wireless sensing. This testing configuration was applied to condition the sensors for testing convenience without losing the fidelity of the sensor performance because the volume change effect can be neglected given the fabricated device dimensions.

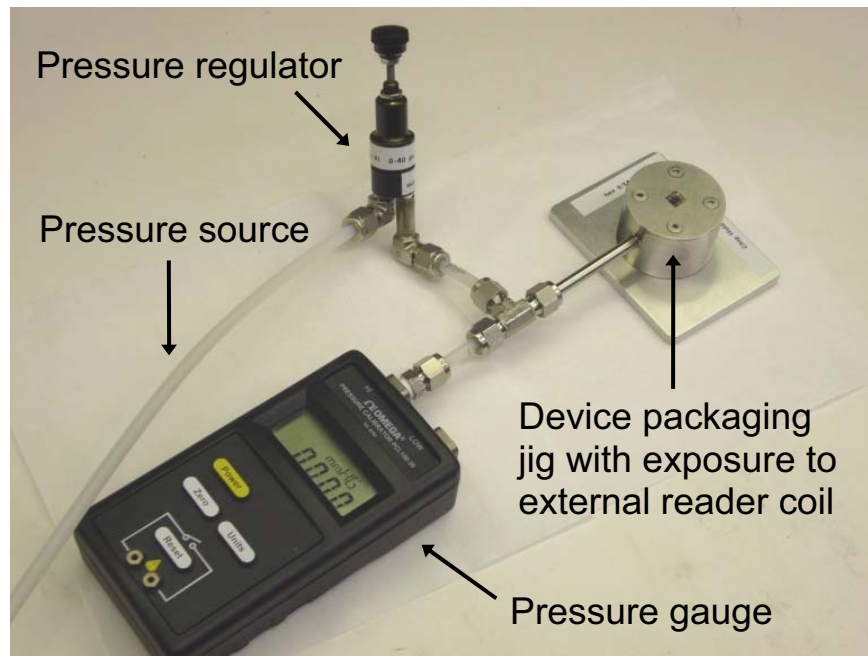


Figure 3-10: On-bench pressure testing setup for device characterization

Experimental results, as shown in Figure 3-11, successfully verified the feasibility of wireless pressure sensing with the sensor in variable capacitor design as an example. The phase-dip plots indicate that, as the pressure inside the diaphragm chamber increases, the diaphragm is deformed outward and moves the embedded metal components away from the bottom substrate, leading to a decrease in the overall capacitance/inductance and an increase in the resonant frequency of the sensor.

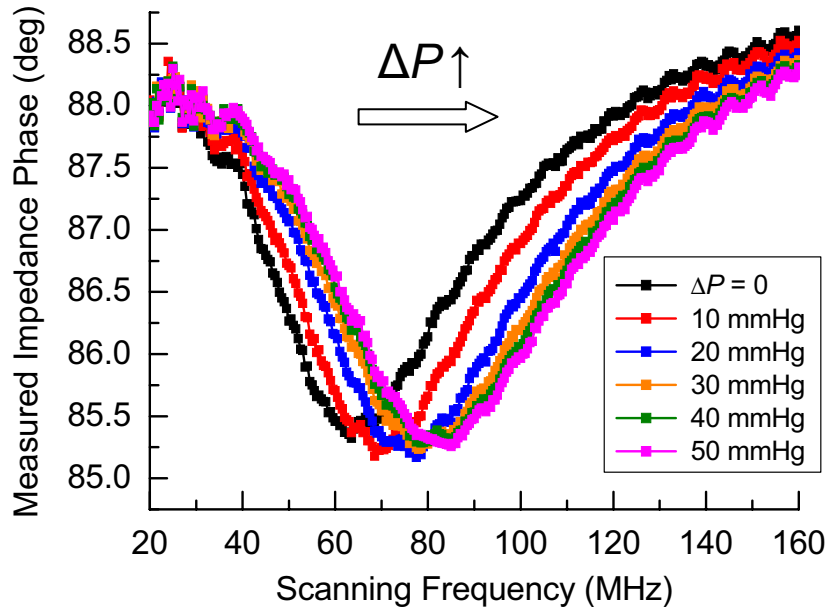


Figure 3-11: Overlay plot of measured phase-dip curves of the sensor (variable capacitor design as example) in on-bench wireless pressure sensing. $\Delta P = P_{\text{inside sensor}} - P_{\text{outside sensor}}$.

For the sensors in variable capacitor design, the normalized shifted resonant frequency can be written as

$$\frac{f_{\min}(\Delta P)}{f_{\min}(\Delta P = 0)} = \frac{\frac{1}{2\pi\sqrt{L_s(C_s - \Delta C_s)}}}{\frac{1}{2\pi\sqrt{L_s C_s}}} = \sqrt{1 + \frac{\Delta C_s}{C_s}} \quad \text{if } \Delta C_s \ll C_s, \quad (3.15)$$

where ΔC_s is the changed capacitance due to diaphragm deflection. It can be further derived to

$$\frac{f_{\min}(\Delta P)}{f_{\min}(\Delta P = 0)} = (1 + \alpha y)^{\frac{1}{2}}, \quad (3.16)$$

where α is a constant coefficient based on material properties and physical dimensions of the device. Assuming small diaphragm deflection which is proportional to pressure difference by (3.12), the relationship can be finally derived to

$$\frac{f_{\min}(\Delta P)}{f_{\min}(\Delta P = 0)} = (1 + \alpha' \Delta P)^{\frac{1}{2}}, \quad (3.17)$$

where α' is a parameter incorporating the mechanical behavior of the diaphragm. For the sensors in variable capacitor/inductor design, the normalized shifted resonant frequency can be written as

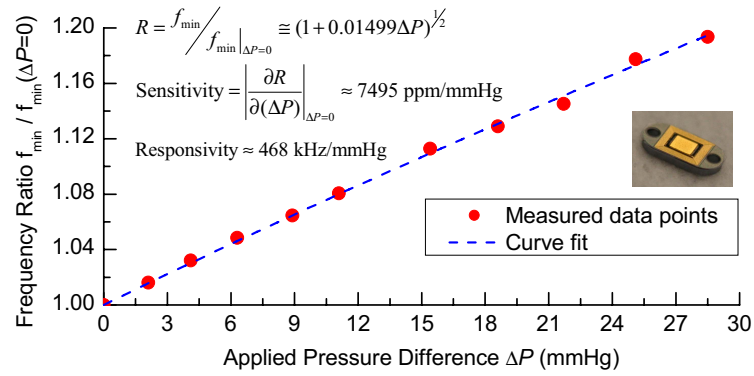
$$\frac{f_{\min}(\Delta P)}{f_{\min}(\Delta P = 0)} = \frac{\frac{1}{2\pi\sqrt{(L_s - \Delta L_s)(C_s - \Delta C_s)}}}{\frac{1}{2\pi\sqrt{L_s C_s}}} = \sqrt{1 + \frac{\Delta L_s}{C_s}} \sqrt{1 + \frac{\Delta C_s}{C_s}} \quad \text{if } \begin{matrix} \Delta L_s \ll L_s \\ \Delta C_s \ll C_s \end{matrix}, \quad (3.18)$$

where ΔL_s is the changed inductance due to diaphragm deflection. Similar procedures can be used with the small deflection assumption to derive the dependency of the normalized shift resonant frequency on pressure difference as

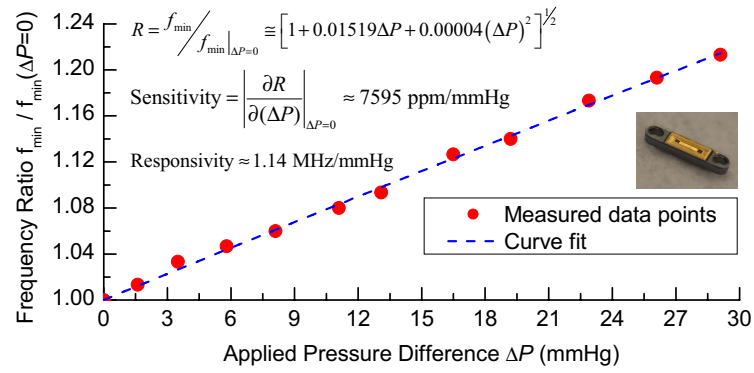
$$\frac{f_{\min}(\Delta P)}{f_{\min}(\Delta P = 0)} = \left[1 + \beta_1 \Delta P + \beta_2 (\Delta P)^2 \right]^{\frac{1}{2}}, \quad (3.19)$$

where β_1 and β_2 are parameters incorporating coupled capacitance and inductance variations from the mechanical behavior of the diaphragm, implying more sensitive pressure response from this design. The measurement results from the sensors in both

designs shown in Figure 3-12 were well fit using (3.17) and (3.19) in 0–30 mmHg pressure operation range. Data analysis confirmed that the microfabricated sensors achieved excellent pressure-sensing performance with high sensitivities ($> 7,000$ ppm/mmHg), providing readouts with resolutions smaller than 1 mmHg so as to sufficiently cover all pressure variations of interest for practical IOP monitoring. Highly sensitive pressure responses were obtained based on high compliance of the parylene flexible diaphragm and high resonant frequency of the sensors. In spite of its smaller parylene diaphragm, the sensor in the variable capacitor/inductor design has comparable sensitivity result with that in the other design, showing the possibility of using devices in a smaller form factor while achieving the required sensing performance. Corrections would need to be made on (3.17) and (3.19) to accommodate large diaphragm deflections by (3.12) if the diaphragm experiences large pressure loadings, as this pressure-sensitivity-reduced effect can be observed in Figure 3-11, where the shift of phase-dip frequency was smaller when the applied pressure difference was closer to 50 mmHg. Table 3-2 summarizes several important characteristics of the microfabricated wireless pressure sensors presented in this work



(a)



(b)

Figure 3-12: On-bench pressure testing results of the sensors. (a) Sensor in variable capacitor design. (b) Sensor in variable capacitor/inductor design

Table 3-2: Measured characteristics of the microfabricated pressure sensors

	Variable C	Variable C&L
Planar dimensions	4 mm × 2 mm	4 mm × 1 mm
Resonant frequency	~ 62 MHz	~ 150 MHz
Quality factor	~ 3	~ 5
Pressure sensitivity	7495 ppm/mmHg	7595 ppm/mmHg
Pressure responsivity	0.47 MHz/mmHg	1.14 MHz/mmHg

3.4.3 *Ex vivo* pressure sensing test

The pressure sensor was implanted into an enucleated porcine eye, as shown in Figure 3-13, in order to demonstrate acute *ex vivo* pressure sensing characterization. The microfabricated sensor was placed under the cornea so as to have the best proximity to the external reader coil. Hence, a corneal flap incision was made with the use of sutures to restore environment to an enclosed intraocular space after implantation. A catheter was then inserted to the eye model interfacing with an external infusion-based pressurization setup to simulate a situation of IOP variation. Although not ideal, the experimental results shown in Figure 3-14 demonstrated the feasibility of using this microsensor for wireless pressure sensing in such an isolated environment. The measured phase-dip frequency of the equivalent impedance dropped more than 15% as the sensor implant experienced a substantial environmental permittivity change in the liquid medium as compared with air [13]. The measurement noise in the plots resulted from the close proximity of the reader coil to the cornea necessary for interrogating the implant given the short sensing distance, and could be greatly improved by having a longer sensing distance from stronger sensor-reader coil coupling. The results revealed another issue: it was difficult to characterize the pressure sensitivity in this testing setup because stable pressure control was not achieved due to protocols in place at the time of surgery. For more systematic *ex/in vivo* pressure sensing studies, development of surgical procedures and tools having improved compatibility will be another focus of future work.

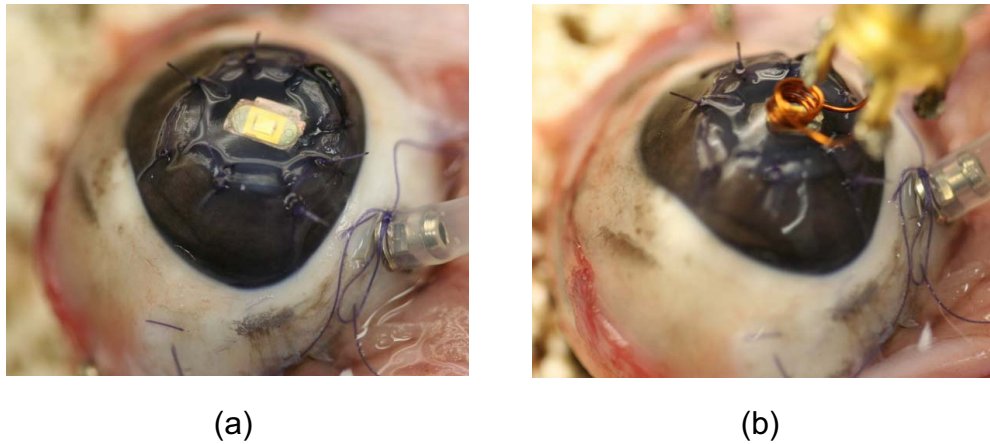


Figure 3-13: *Ex vivo* device testing to demonstrate the wireless pressure sensing behavior of the sensor implant. (a) Test model with the sensor inside the eye. (b) Wireless sensing with the external coil placed in front of the eye model

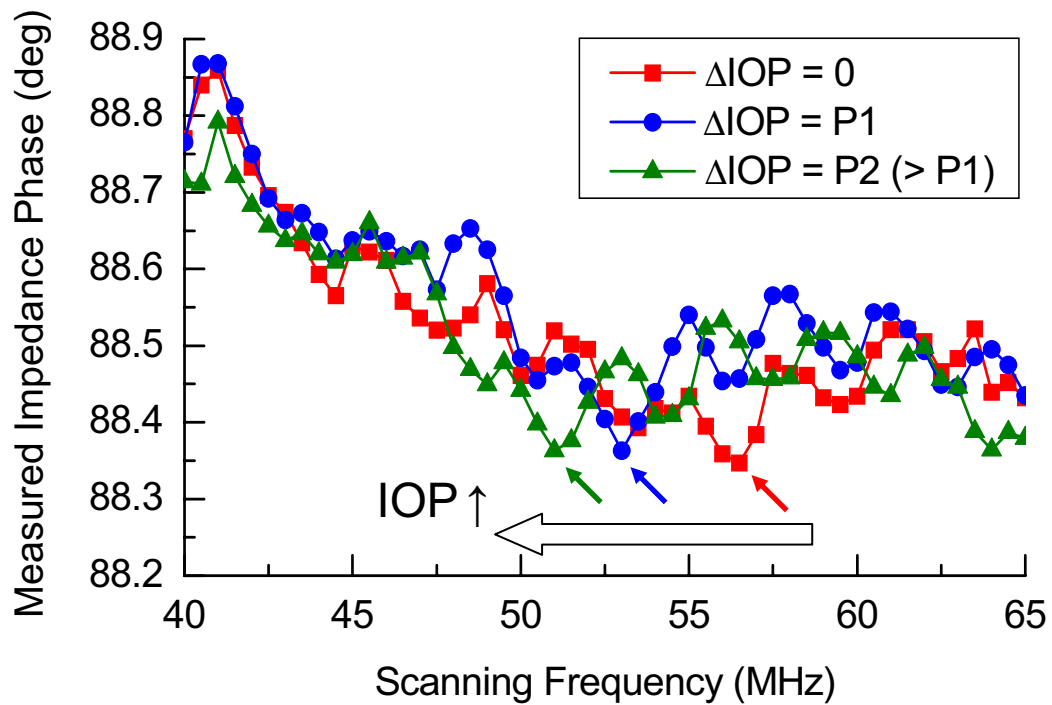


Figure 3-14: Overlay plot of measured phase-dip curves of the sensor (variable capacitor design as example) in *ex vivo* wireless pressure sensing. The small arrows indicate the phase-dip shift with respect to the simulated IOP increase.

3.4.4 *In vivo* implantation test

In vivo device implantation testing was conducted using live rabbit eyes as the model to evaluate the bioefficacy and biostability of the sensor implant. The fully packaged microdevices with the bottom sealing piece were sterilized using ethylene oxide gas and implanted at the pars plana site in the eyes of two rabbits. A small 2-mm angled razor blade incision was made to insert the implant into the eye. Clinical procedures utilizing the end suture holes of the devices were developed to facilitate fast and robust device anchoring during implantation. The operation could be completed within 15 min, curtailing occurrence of surgical complications. Long-term follow-up observation, with result photographs shown in Figure 3-15, verified implant biocompatibility, as no post-operative complications appeared in the intraocular environment. Given these results as the basis, further improvements of such an implant paradigm were performed as described in the following section.

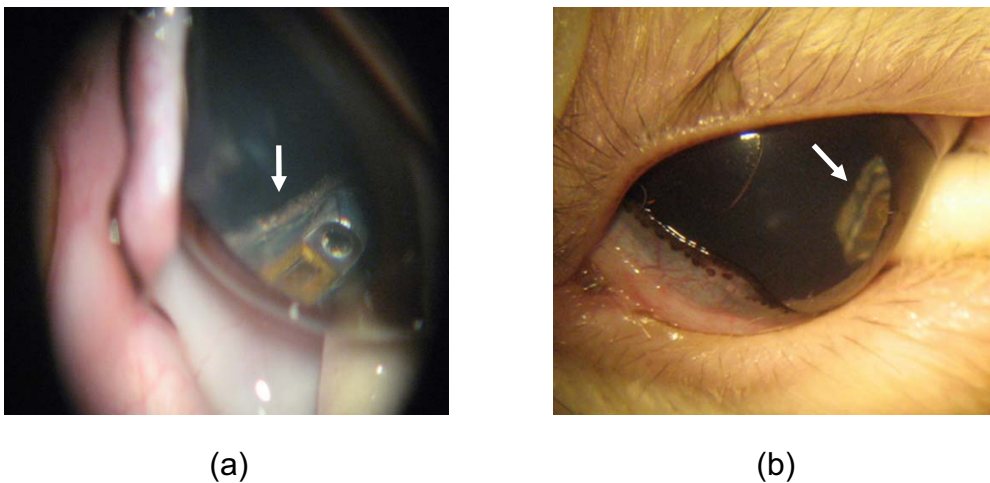


Figure 3-15: Follow-up study results of *in vivo* device testing using rabbit model to verify long-term biocompatibility of the intraocular implant. (a) 3 months after surgery. (b) 6 months after surgery. The arrows indicate the implant as observed through the cornea.

3.5 Improvement Strategies and Results

In spite of successful wireless pressure sensing demonstration, the sensing distance of the entire sensor-reader system was not sufficient, especially when considering the ultimate glasses-to-iris distance in practice, and thus needs further improvement. Because the entire sensing scheme is based on impedance measurement given by (3.3), efforts can be made to increase the measurement sensitivity to obtain a more distinguished phase dip, so that the corresponding sensing distance can be enhanced. Accordingly, separate strategies can be applied to 1) increase the magnitude of the real term, which involves sensor improvement, or 2) decrease that of the imaginary term, which involves reader improvement, to enhance the sensing performance. This work focuses on improvement of sensor design for electromagnetic coil coupling and resonance quality factor enhancements, followed by the improvement of readout method for noise reduction and signal-to-noise ratio (SNR) enhancement in actual wireless measurements. These modifications have been implemented as described in the following sections to experimentally verify their effect on increasing the overall sensing distance of such a telemetric system for practical IOP monitoring.

3.5.1 Improved sensor design and fabrication

In terms of sensor improvement, both the quality factor and integrated coil size should be increased as much as possible in order to increase the k^2Q factor in (3.4). Another flexible-coiled microsensor prototype was created to prove this concept. Its design, illustrated in Figure 3-16, features a larger circular disk substrate to incorporate a larger spiral inductor. The disk diameter was designed to be 4 mm, fitting the iris rim

width in normal conditions, and the disk was made out of parylene C with sufficient mechanical flexibility so as to maintain a small required incision (< 2 mm) during device implantation. This flexible/foldable coil disk was monolithically microfabricated in integration with a bottom rigid silicon substrate in a suitable form factor smaller than $4 \text{ mm} \times 1.5 \text{ mm}$ for ease of handling and realization of the parallel-plate variable capacitor. Because this prototype also needs another attachment piece to realize the pressure reference in gauge pressure sensing, surgical features were directly created on the non-electronic sealing silicon piece for suture-less implant fixation on the iris. Electrical/mechanical design, material selection, and micromachining processes of the pressure-sensitive resonant circuit structures were analogous to those previously described, with more intuitive equations applicable to calculate inductance of the circular spiral coil. For example, the inductance of such a coil can be calculated as [15]

$$L \cong \frac{\mu_0 n^2 d_{\text{avg}} c_1}{2} \left[\ln \left(\frac{c_2}{F} \right) + c_3 F + c_4 F^2 \right], \quad (3.20)$$

where n is the number of turns of the inductor, d_{avg} is the averaged diameter of the coil windings, $F = (d_{\text{out}} - d_{\text{in}}) / (d_{\text{out}} + d_{\text{in}})$ the fill factor of the coil windings, and c_1 – c_4 are constant coefficients determined by the winding geometry. The resistance and capacitance of the sensor can be determined by the same relations in (3.8)–(3.10). Besides the electrical behavior, the mechanical behavior of the parallel-plate variable capacitor was determined by (3.11) specifically in the small deflection regime to better estimate the pressure-sensitive performance of the micro-electro-mechanical device. By incorporating this theoretical model into sensor design, the thicknesses of the first layer metal line ($3 \text{ }\mu\text{m}$) and the sandwiched parylene ($8 \text{ }\mu\text{m}$)-metal ($0.5 \text{ }\mu\text{m}$)-parylene ($8 \text{ }\mu\text{m}$)

structures were substantially increased in order to facilitate better electrical/structural behavior of the microsensor. Moreover, besides being used to create the top parallel capacitor plate, the second metal layer was arranged to be with all boundaries of the pressure-sensitive parylene diaphragm chamber in order to effectively serve as a barrier to water vapor and gas transmissions/permeations in between the encapsulated air/gas and the ambience of the device [23]. It prevents them from substantial performance drift and guarantees their long-term operation in the intraocular environment.

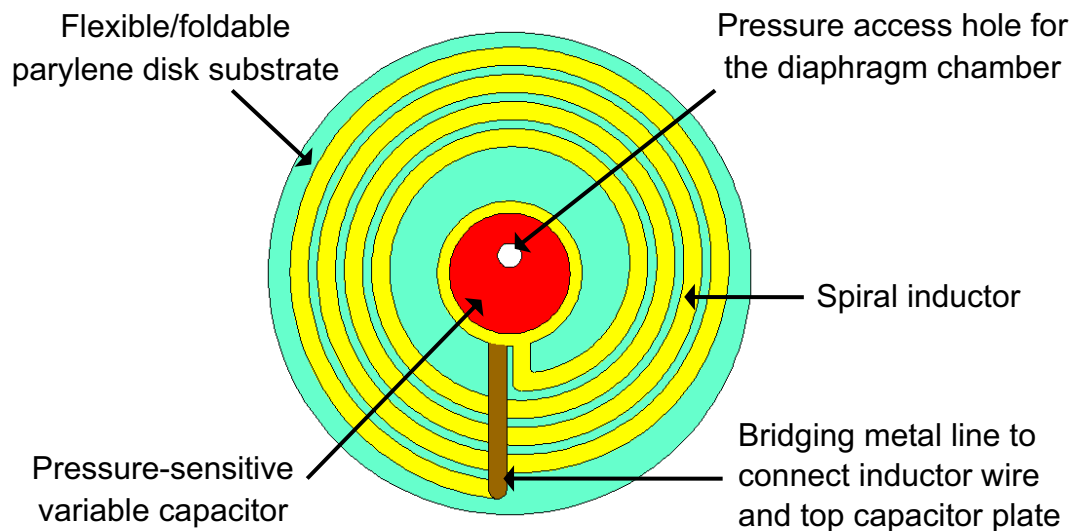


Figure 3-16: Pressure sensor design with flexible parylene coil disk (top view). The bottom silicon substrate and the pressure-sensitive flexible diaphragm are not shown in this planar illustration.

The fabrication process of the modified wireless pressure sensor illustrated in Figure 3-17 is comparable to that described in Section 3.3. As previously stated, the deformable diaphragm was created by parylene-metal-parylene layers, including all

sidewalls, so as to minimize liquid/gas permeation from/to the encapsulated air cavity.

Figure 3-18 shows the microfabricated flexible parylene-based sensors.

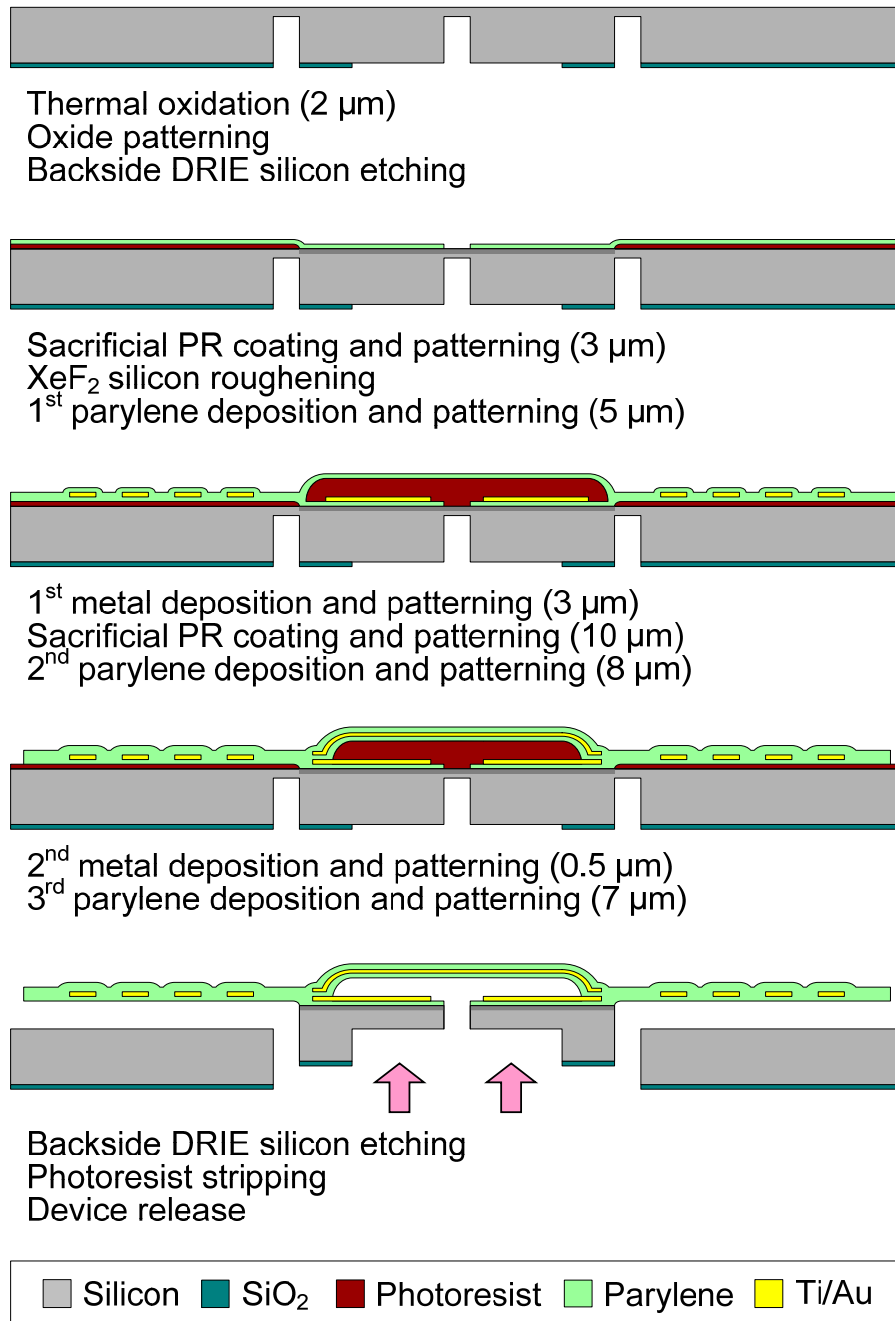


Figure 3-17: Fabrication process flow of modified flexible-coiled microsensor. The arrows indicate the outcome of device release after microfabrication processes.

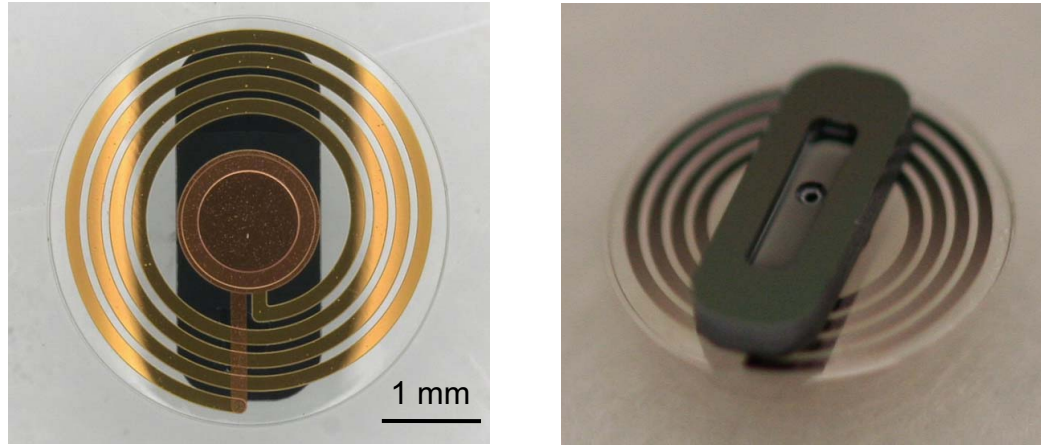


Figure 3-18: Full-scale image of the modified flexible-coiled microsensor with its top (left) and bottom (right) views. The diameter of the flexible coil disk was 4 mm.

After packaging the sensor with a non-electronic piece on the bottom for pressure reference, the overall size was measured at $\phi 4 \text{ mm} \times 1 \text{ mm}$ and reduced to a form factor of $4 \text{ mm} \times 1.5 \text{ mm} \times 1 \text{ mm}$ by folding the coil disk as shown in Figure 3-19, still suitable for minimally invasive intraocular implantation. Given the high yield strain ($\sim 3\%$) characteristic of parylene C, the flexible disk could be stretched back to circular shape without severe permanent deformation after this extent of folding.

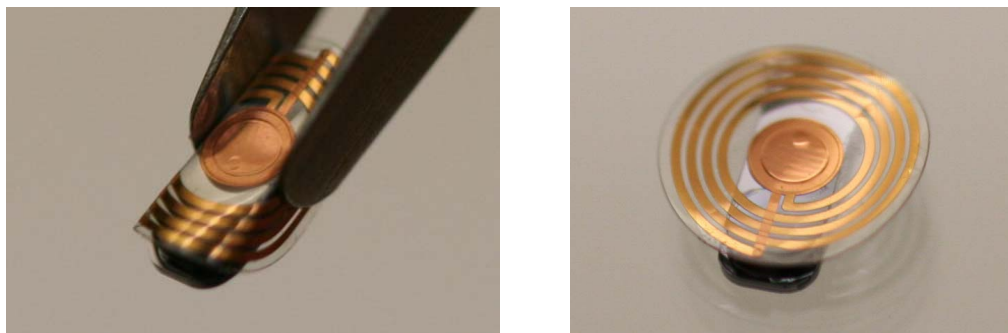


Figure 3-19: Device flexibility demonstration. The device width could be reduced to 1.5 mm (predetermined by bottom silicon substrate) when folded (left), then stretched back after folding (right) without permanent deformation or other severe damages.

3.5.2 Improved readout method design and implementation

Even though the modified sensor design was implemented, it is still not sufficient for achieving the required sensing distance when using the primitive readout method, as previously described, due to high noise from the actual testing system. Photographs of the captured frequency scans shown in Figure 3-20 indicate that the signal strength of the detected phase dip decreases as the sensing distance increases due to the decreased inductive coupling between sensor and reader coils. With this effect the maximum sensing distance can be defined as where the phase dip signal is lower than the noise floor, and is thus undetectable. Using the aforementioned measurement setup, a $\Delta\phi \sim 0.1^\circ$ noise was obtained, and the corresponding maximum sensing distance is characterized to be only approximately 1 cm with the optimized size of the reader coil. However, phase change can still be identified as shown in Figure 3-21 when the distance is more than 1 cm, giving evidence that electromagnetic coil coupling still exists in that distance range; thus longer sensing distance should be achievable if the noise floor can be reduced.

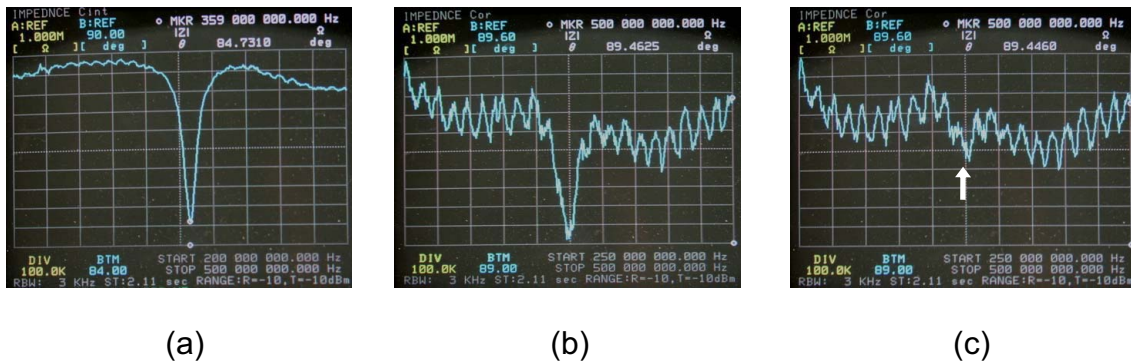


Figure 3-20: Photographs of the captured frequency scans showing detected impedance phase dip with the modified flexible-coiled sensor. (a) Sensor in proximity to reader coil. (b) Sensing distance = 0.5 cm. (c) Sensing distance = 0.75 cm

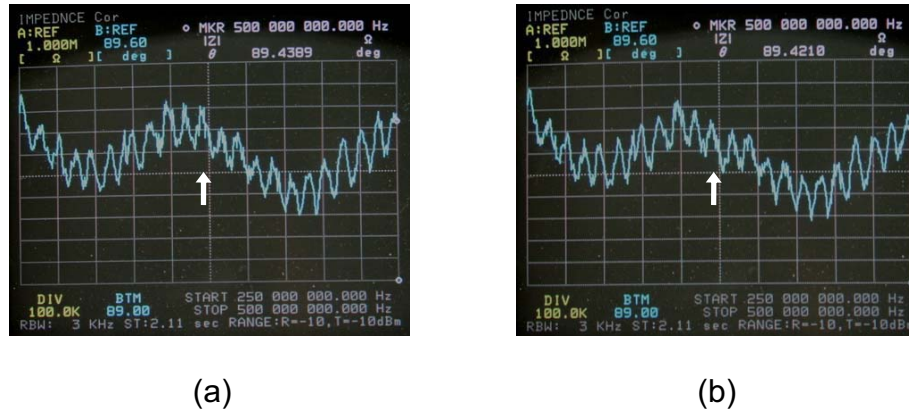


Figure 3-21: Photographs of the captured frequency scans when the sensing distance was 1 cm. (a) Signal without sensor interaction. (b) Signal with sensor interaction. Obviously the phase dip is covered by the noise in this case, but slight phase change from the baseline signal is identifiable during experiments.

From the need of phase-dip spectrum recovery for frequency recognition in further coil separation distance, a supportive data-processed external readout method has been developed in this work. This method was implemented using the same measurement unit as previously described as it only involves post-measurement data processing and analysis, so that no additional efforts needed to be made on physical sensor and reader components. The process scheme, as shown in Figure 3-22, is based on a noise reduction concept with measurement averaging [24] accompanied by frequency averaging procedure for better phase-dip spectra recovery. First of all, multiple frequency scan samples are obtained using the measurement instrument in the aforementioned operation. The samples are categorized in two groups: one where the reader coil is not interrogating or interacting with the sensor implant, which is defined as the baseline signal, and the other where the reader coil is interrogating or interacting with

the sensor implant, which is defined as the sensor signal. The necessary sample data are captured and stored to the personal computer through a data acquisition system. The data are then processed in a series of operations including the following: 1) baseline/background subtraction; and 2) averaging of the processed scans (i.e., time averaging) in common signal processing principle. The baseline/background subtraction serves the purpose of eliminating substantial environmental interferences on the sensor-reader coil interaction, and the time averaging can significantly reduce the random noise of the signals from the actual sensor and reader coils. The sequence of such operations is interchangeable due to their linear operation nature, also resulting in the possibility of algorithm optimization depending on actual hardware/software constraints. The reduced representative noise floor on the frequency scan after such operations can be mathematically represented as

$$\Delta\phi' = \overline{(\phi_{\text{sensor}} - \phi_{\text{no sensor}})} \quad (3.21)$$

in Option 1 in Figure 3-22, equivalent to

$$\Delta\phi' = \overline{\phi_{\text{sensor}}} - \overline{\phi_{\text{no sensor}}} \quad (3.22)$$

in Option 2 in Figure 3-22. The processed data through Option 1 procedures, for example, are shown in Figure 3-23. The measured phase noise was successfully reduced from the original value of $\sim 0.1^\circ$ to $\sim 0.01^\circ$ by the differentiating the signals, and further to $\sim 0.003^\circ$ after processing 20 scan samples (10 for the baseline signal and 10 for the sensor signal), indicating more than a $30\times$ noise reduction so as to enhance the resultant sensing distance, even without signal strengthening by other modification on the sensor implant or the associated reader coil setup.

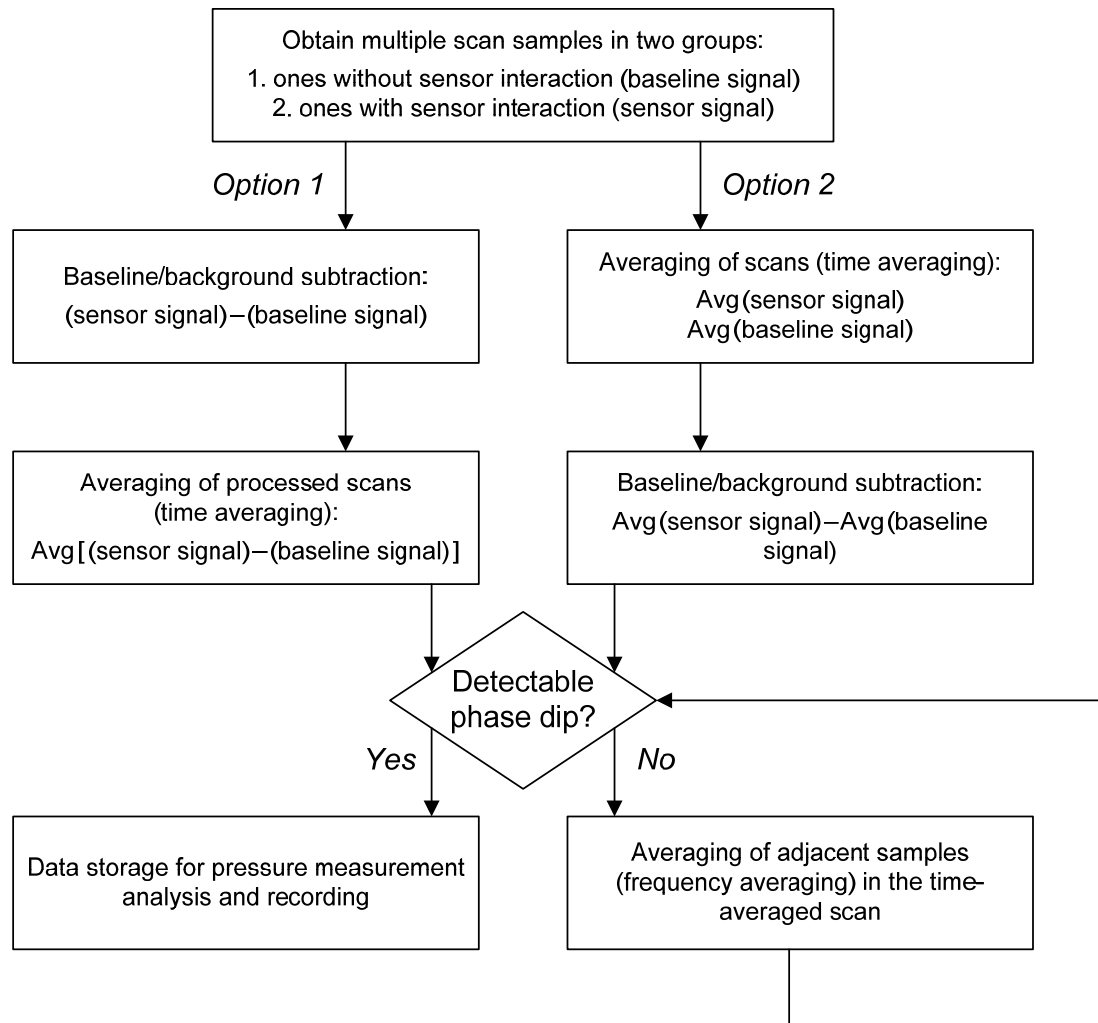


Figure 3-22: Process scheme of developed data-processed external readout method

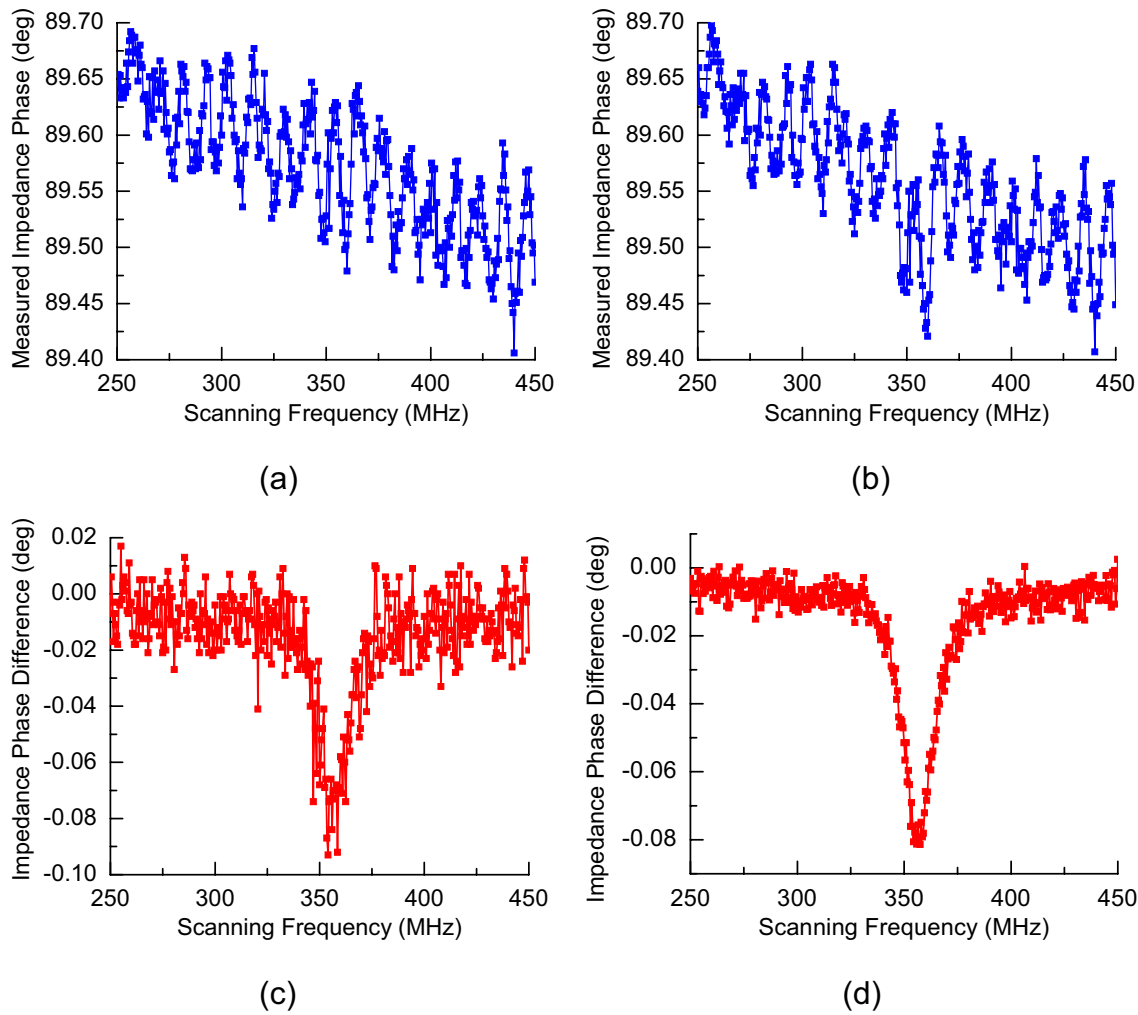


Figure 3-23: Data samples through Option 1 operations for example. (a) Unprocessed baseline signal. (b) Unprocessed sensor signal. (c) Processed signal after baseline/background subtraction. (d) Processed signal after time averaging (sample size = 20)

After such operations, the data after baseline/background subtraction and time averaging operations can be investigated for detectable phase-dip frequency, as shown in Figure 3-23(d). If a phase dip can be detected at a certain frequency point, the data is stored for the corresponding pressure measurement analysis. If such a dip can not be detected, further data processing, including frequency averaging, needs to be utilized to

virtually increase the SNR for better phase-dip spectra recovery. Frequency averaging is a common signal processing technique where adjacent samples are averaged in the frequency domain [25]. Similar operations based on this concept include the use of moving averaging in financial and economic fields. For example, the SNR of the plot shown in Figure 3-23(d) can be further enhanced by appropriate frequency averaging with the data, as shown in Figure 3-24, for better phase dip detection. Figure 3-25 shows another successful data example benefited from the frequency averaging operation. These examples clearly illustrate the advantages of exploiting the proposed data processing method. Combining the modified implantable flexible-coiled sensor and the data-processed external readout method, prevailing low-noise long-range signal detection can be anticipated to facilitate the continuous wireless passive pressure sensing system.

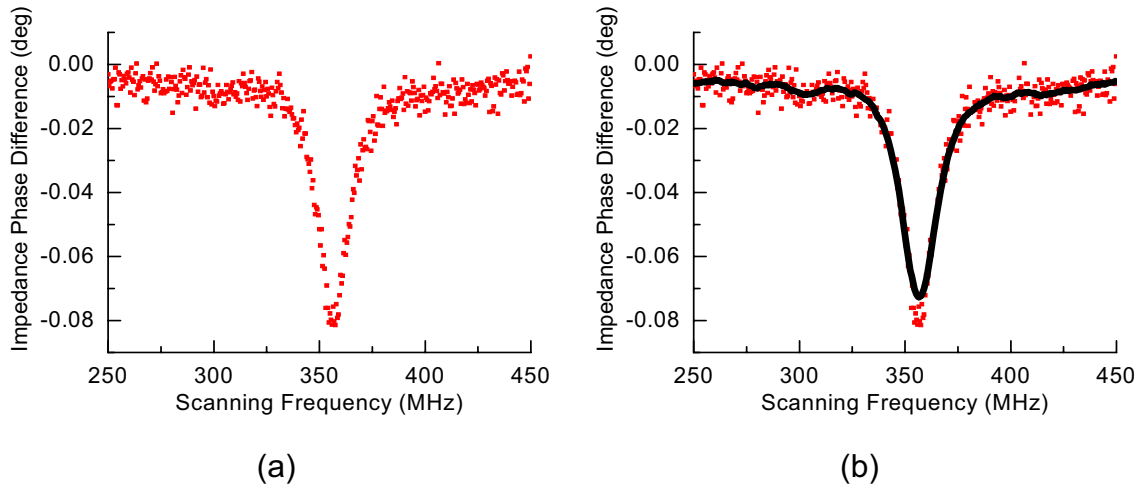


Figure 3-24: Frequency averaging with data samples used in Figure 3-23 to illustrate the enhanced phase dip detection scheme. (a) Data points from Figure 3-23(d) before frequency averaging. (b) Smoothed curve after frequency averaging with higher SNR, thus more obvious phase dip over the entire frequency spectrum

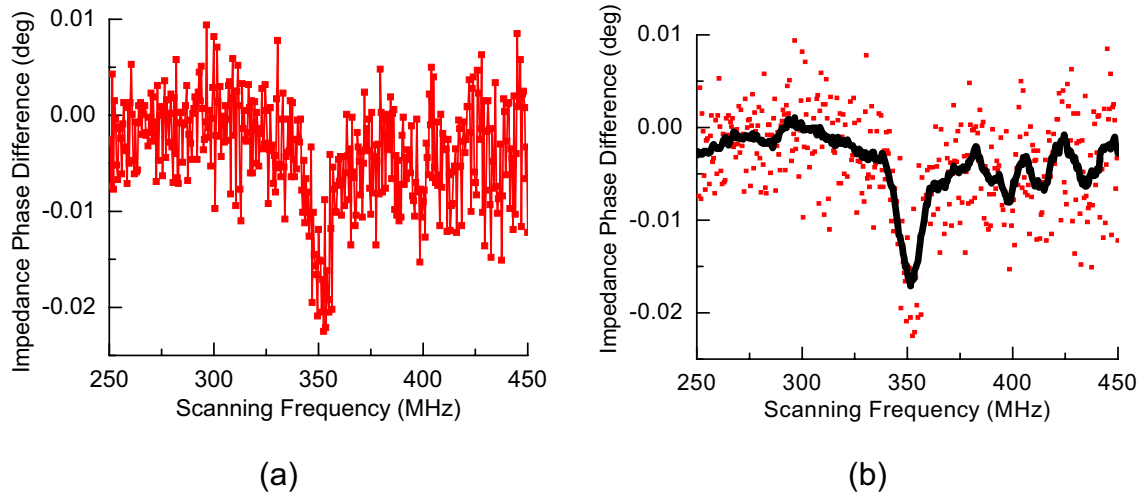


Figure 3-25: Another data sample used to illustrate the frequency averaging operation. (a) Processed data before frequency averaging (sample size = 20 for time averaging). (b) Smoothed curve after frequency averaging with unveiled impedance phase dip

3.5.3 Characterization results and discussions

The modified microfabricated flexible pressure sensor has been successfully characterized. The same on-bench electrical testing configuration was utilized for electrical characterization of the device, with the experimental results listed in Table 3-3, for comparison with the previous sensor prototype in fixed coil design. Smaller electrical inductance, capacitance, and resistance resulted in a higher resonant frequency and higher quality factor of such paradigm. A modified pressure control configuration, as shown in Figure 3-26, was utilized for wireless pressure sensing demonstration. The device was placed inside the customized chamber connected to a pressurization setup where a commercial off-chip pressure regulator and a pressure gauge were used to provide 0.5 mmHg tuning resolution. Accurate environmental pressure variations could thus be created for the device ($\Delta P = P_{\text{outside sensor}} - P_{\text{inside sensor}}$) with this pressure-control setup.

Table 3-3: Measured electrical parameters of the flexible-coiled pressure sensor

Parameters	Values
Inductance	57 nH
Capacitance	3.6 pF
Resistance at resonance	4.2 Ω
Resonant frequency	~ 350 MHz
Quality factor	~ 30

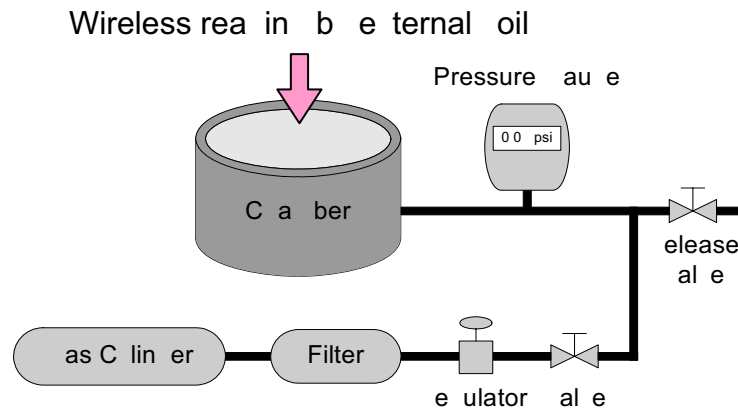


Figure 3-26: Schematic of on-bench pressure testing setup for characterization of the modified flexible-coiled sensor

Although the pressure sensitivity was expected to be small due to the use of a smaller and less flexible circular parylene diaphragm, it was compensated by the high resonant frequency, resulting in a reasonable pressure responsivity for detection of phase-dip shift with respect to environmental pressure variations. Measured phase-dip curves and a sensitivity characterization curve were obtained, as shown in Figures 3-27 and 3-28, to characterize the wireless pressure sensing behavior. A similar relation to (3.17) was used in the analysis with different sign convention due to a different pressurization

situation. It was also observed that the aforementioned volume change effect from the encapsulated air/gas reference was non-negligible in this case. As shown in Figure 3-29, the ideal pressure sensitivity was designed to be 985 ppm/mmHg, while in measurements only 455 ppm/mmHg sensitivity was obtained when the sealed cavity volume was $500\text{ }\mu\text{m} \times 2,000\text{ }\mu\text{m} \times 250\text{ }\mu\text{m}$ (width \times length \times height). By designing different geometry on the non-electronic sealing piece to double the sealed cavity volume ($500\text{ }\mu\text{m} \times 2,000\text{ }\mu\text{m} \times 500\text{ }\mu\text{m}$) in the final packaged device, the pressure sensitivity and responsivity was experimentally characterized to be 695 ppm/mmHg and 243 kHz/mmHg, approximately 1.52 \times enhancement over the original values and closer to the ideal values. These results were in good agreement with expectations after incorporating the ideal gas law, and showed the possibility of altering/optimizing the design parameters depending on actual application specifications.

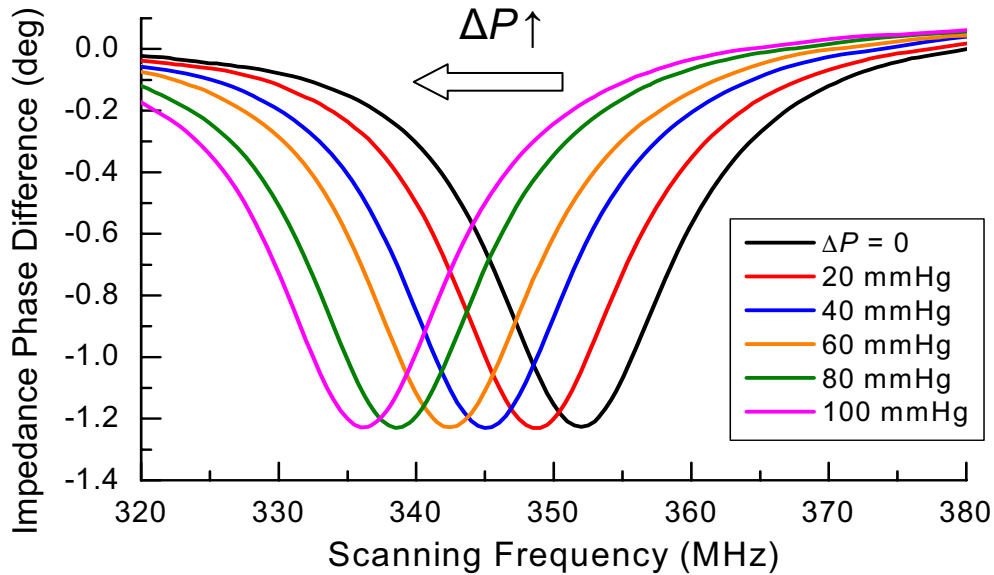


Figure 3-27: Overlay plot of the measured phase-dip curves of the modified sensor in on-bench wireless pressure sensing. $\Delta P = P_{\text{outside sensor}} - P_{\text{inside sensor}}$.

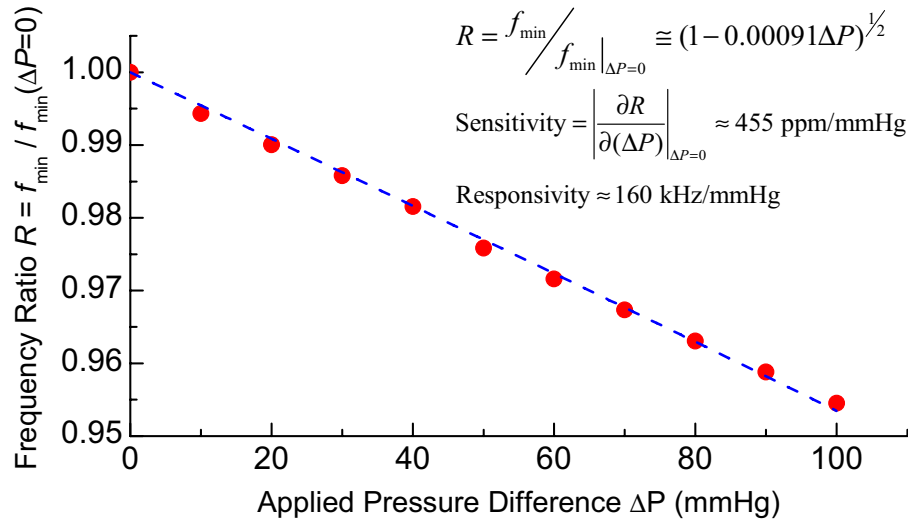


Figure 3-28: On-bench pressure testing result of the modified sensor

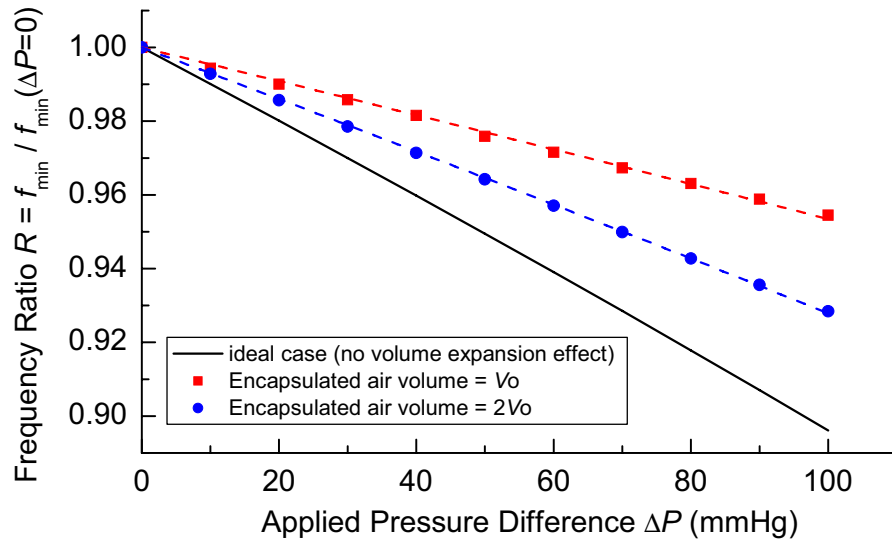


Figure 3-29: Characterization of volume change effect of the encapsulated air

Next, the data-processed readout method was incorporated for sensing distance studies of such a wireless system. For demonstration purposes, devices with different e-beam evaporated gold thicknesses ($3 \mu\text{m}/0.5 \mu\text{m}$ and $6 \mu\text{m}/1 \mu\text{m}$ for first and second metal layer structures, respectively) were prepared. The doubled metal thickness resulted

in approximately $1.5 \times Q_s$ enhancement (from ~ 30 to ~ 45). This enhancement was primarily limited by the high-frequency skin depth effect from the inductor wire resistance at the operating frequency. Also it is worth noting that the metal line thickness could be further increased by depositing thicker metal through current evaporation methods or an electroplating alternative, or by stacking in a special post-microfabrication technique [26] to further reduce the series resistance of the inductor and enhance the overall quality factor. The necessary number of samples for averaging operations depends on the final frequency measurement resolution needed for ultimate pressure sensing. The frequency noise (i.e., frequency fluctuation) in measurements needs to be lower than the resultant frequency shift from environmental pressure variation for reliable pressure sensing accuracy. As previously stated, the pressure sensitivity of the modified flexible-coiled sensor was characterized to be approximately 455 ppm/mmHg, which meant the allowed frequency fluctuation must be lower to achieve 1 mmHg pressure-sensing accuracy. With this information, experiments were designed to verify the sample size effect on SNR and frequency fluctuation. Using a $Q_s \sim 45$ sensor with a 4-mm-diameter on-sensor coil interrogated by a 15-mm-diameter hand-wound reader coil at 2 cm separation distance, the results are shown in Figure 3-30(a) with the SNR defined as

$$\text{SNR} = \frac{\Delta\phi_{\max}}{\Delta\phi_{\text{noise}}}, \quad (3.23)$$

where $\Delta\phi_{\max}$ is the maximum impedance phase dip throughout the frequency scan, and $\Delta\phi_{\text{noise}}$ is the noise from the measurement system. More than 80 measurement samples had to be collected in order to justify $\text{SNR} > 10$ and the associated frequency shift resolution less than 400 ppm. Fewer samples could be collected but the overall pressure

accuracy would be reduced. On the other hand, more samples could be collected but the processing capacity and time would need to be considered. Given this result the required pressure accuracy in specific applications and the physical noise in the measurement system determine the size of data to be collected and analyzed. Figure 3-30(b) shows that the achieved $\Delta\phi_{\text{noise}}$ was lower than 0.0015° by processing more than 80 samples (40 for sensor signal and 40 for baseline signal) and approaching the limit ($\sim 0.001^\circ$) when more than 200 samples were collected. This limit resulted from the noise sources which could not be cancelled or suppressed, so fundamental reader unit modifications—including the use of a low noise amplifier (LNA) or other low-noise electronic techniques, as introduced at the end of this section—would be necessary to fundamentally reduce the system noise, and thus achieve higher SNR and longer range sensing.

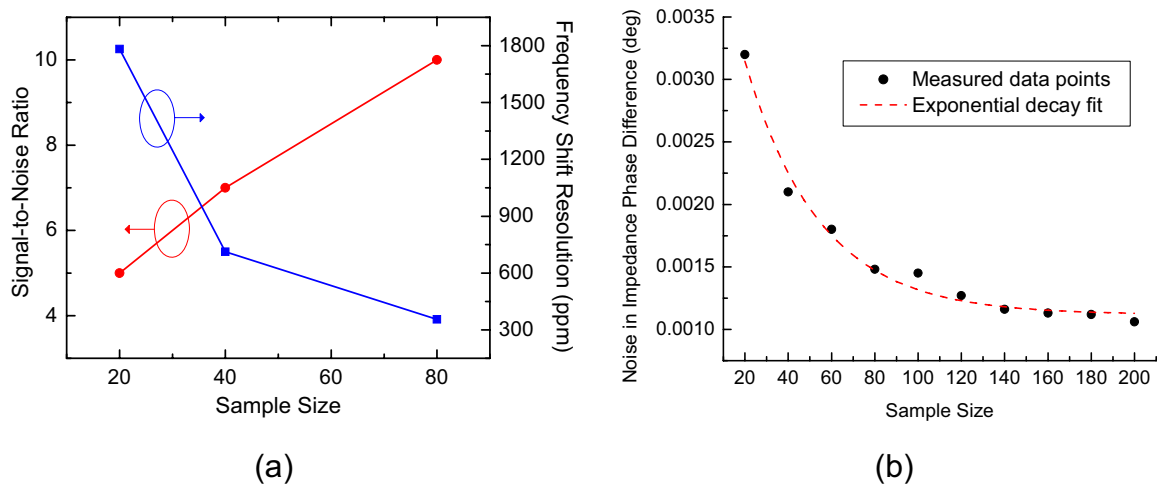


Figure 3-30: Sample size effect on frequency measurements. (a) Obtained SNR and frequency shift resolution. (b) Obtained $\Delta\phi_{\text{noise}}$ with the exponential fit illustrating the reduction limit of using the data-processing readout method. Half of the samples were collected from sensor signal and the other half were from the baseline/background signal.

Sensing distance enabled by the aforementioned flexible-coiled sensor and the data-processed external readout method was studied. The criterion of determining maximum sensing distance was set to be $\text{SNR} > 10$ given the minimal $\Delta\phi_{\text{noise}} \sim 0.001^\circ$ so that the phase-dip frequency measurements were sufficiently accurate for analyzing 1 mmHg pressure difference. The maximum sensing distance was therefore characterized to be 2 cm and 2.5 cm for $Q_s \sim 30$ (3 $\mu\text{m}/0.5 \mu\text{m}$ metal structures) and $Q_s \sim 45$ (6 $\mu\text{m}/1 \mu\text{m}$ metal structures) sensors, respectively. Experiments using a $Q_s \sim 45$ sensor with approximately 4-mm-diameter on-sensor coil interrogated by hand-wound reader coils in different sizes were conducted to further study the relation between coil separation distance and associated electrical performance. Figure 3-31 clearly shows that the phase dip and the derived coupling coefficient from (3.4) decreases as the coil separation increases, with an empirical relation equivalent to that found in [24] as

$$\begin{cases} k \propto z^{-1} & \text{when } z \ll r_p \\ k \propto z^{-3} & \text{when } z \rightarrow r_p \end{cases}, \quad (3.24)$$

where z is the coil separation distance and r_p is the reader coil radius. The obtained phase dip-distance product analogous to gain-bandwidth product was higher for larger reader coils. Both the near-field and far-field coil coupling situations were well described by (3.24), and were in good agreements with theoretical expectations that are derived from [14, 24, 27–29]. With these findings, the ultimate reader coil can be properly designed and realized as part of the glasses-type reader shown in Figure 3-2, incorporating the necessary glasses-to-iris distance (1.5–2 cm) in practical wireless sensing. As a result, the demonstration using the sensor prototype verifies the feasibility of modifying sensor parameters to increase the sensing distance for the required IOP monitoring specifications.

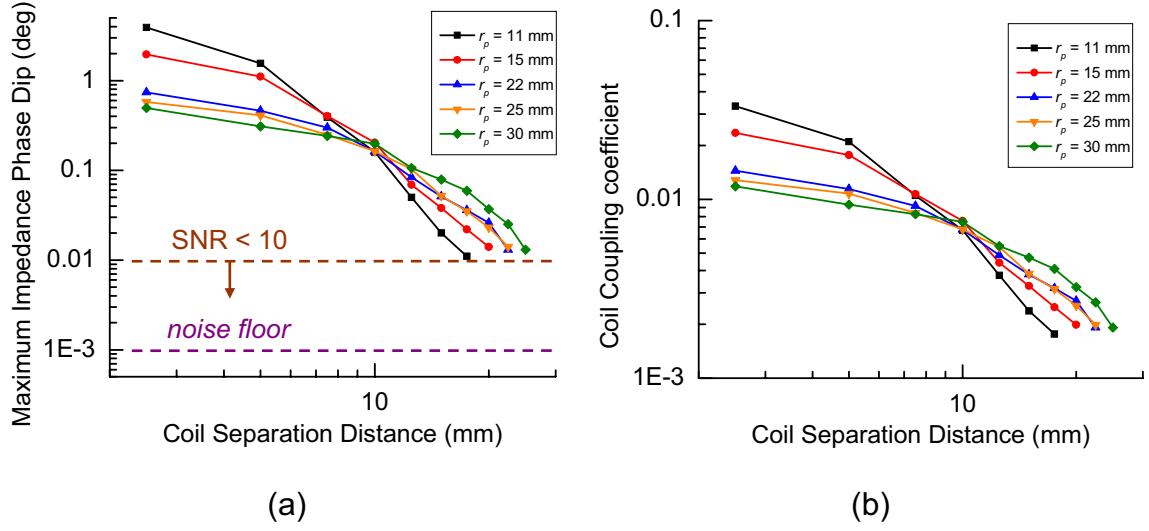


Figure 3-31: Sensing distance study using $Q_s \sim 45$ sensor with approximately 4-mm-diameter on-sensor coil. (a) Measured maximum phase dip plot. (b) Derived coupling coefficient plot using (3.4)

On-bench experimental studies also indicated that the sensor-reader coil coupling is substantially influenced by the medium in which the sensor is placed. As shown in Figure 3-32, the phase-dip frequency was varied from 350 MHz in air to approximately 275 MHz in liquid (water and 0.9% saline) environments, approximately 29% difference. This frequency shift is due to the higher permittivity of water-based solutions (dielectric constant $\epsilon_r \sim 80$ at 20°C) than that of air ($\epsilon_r \sim 1$). It causes increased electrical field concentration on the medium, and so virtually increases the total equivalent capacitance and decreases the resultant phase-dip frequency measured from the external reader. Furthermore, for lossy medium such as saline, the permittivity can be written in the complex form as [29–31]

$$\epsilon = \epsilon' - j\epsilon'', \quad (3.25)$$

with the loss tangent defined as the ratio $\varepsilon''/\varepsilon'$ a measure of the power loss in the medium. Different loss tangent values of water (~ 0) and 0.9% saline (~ 0.2 [11, 31]) reflect their different lossy extent as media degrading the electromagnetic coupling of the coils. As a result, the measured quality factor was around the same value when the sensor was in water as compared with air, while it dropped to ~ 6 when the sensor was in saline. The incorporated sensing distances in water and saline were characterized as 2.5 cm and 1.5 cm, respectively. Solutions to overcoming the decreased sensing distance in saline that has similar composition and properties to the aqueous humor need to be developed, despite the fact that 1.5 cm could be sufficient for practical IOP monitoring. Future works will be investigations on reducing the lossy medium effect using the methods including, but not limited to: 1) strengthening electrical isolation between sensor structures and the environment [11]; and 2) increasing operation/phase-dip frequency to minimize ionic relaxation in response to electromagnetic waves [31]. In addition, the device pressure sensitivity was found invariant to different surrounding media.

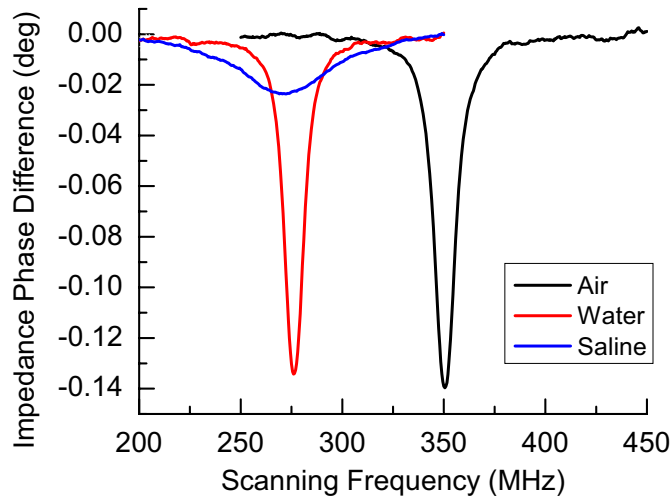


Figure 3-32: Interaction effect in different wave-transmission media. The measured Q_s' were ~ 45 in air, ~ 45 in water, and ~ 6 in 0.9% saline using the flexible-coiled sensors.

Because the operation principle of such a sensor involves encapsulated air/gas reference, the corresponding phase-dip frequency drift due to possible changes of reference needs to be studied as well to verify the sensing feasibility of the sensors. The temperature sensitivity was characterized on-bench as approximately 1064 ppm/°C, in good agreement with design expectations, considering a closed-system air/gas expansion effect based on the ideal gas law. The overall pressure accuracy obtained from this sensor was therefore approximately 2.5 mmHg, incorporating $\pm 1^\circ\text{C}$ temperature fluctuation in the implantation environment (i.e., inside the human body). Other than using temperature compensation techniques, the air/gas reference inside the sensor could be sealed either under low pressure (ultimately in vacuum, as in absolute pressure sensors [21]) or at high temperature so as to directly reduce the pressure-temperature correlation effect. The encapsulated air/gas could also be replaced by liquids to eliminate such effect. After implementing these concepts in device packaging, the pressure sensing accuracy could potentially be improved to 1 mmHg as promised for practical IOP monitoring. Sensor soak tests showed that the phase-dip frequency drift was less than 500 ppm, equivalent to the result by 1 mmHg pressure variation, when the sensor was submerged in saline more than 100 hr at both 25°C and 37°C, confirming the effectiveness of parylene-metal-parylene isolation to liquid/gas permeation and absorption that could affect the pressure reference cavity and other sensor structures [11]. Table 3-4 summarizes important characteristics of the microfabricated flexible-coiled wireless pressure sensor in this work. With the improvements shown here along the way after the developments of the first version of the device, future works on the engineering side will be focused on enhancing pressure accuracy, sensing distance, and device reliability.

Table 3-4: Measured characteristics of the flexible-coiled pressure sensor

Parameters	Values
Planar dimensions	(normal) 4 mm diameter (folded) 4 mm × 1.5 mm
Resonant frequency	~ 350 MHz
Quality factor	~ 30/~ 45* (in air)
Sensing distance	2 cm/2.5 cm* (in air)
Pressure sensitivity	455 ppm/mmHg [†]
Pressure responsivity	160 kHz/mmHg [†]
Temperature sensitivity	1064 ppm/°C
Resonant frequency drift in saline environment	< 500 ppm after 100 hr (at 25°C and 37°C)
Projected pressure accuracy in practical IOP monitoring	2.5 mmHg [‡]

*Altered by different inductor wire thickness

[†] Influenced by volume change effect of the encapsulated air

[‡] Could be improved by modifying encapsulated air conditions

In surgical aspect, a flexible ophthalmic iris retractor (Alcon/Grieshaber AG, Schaffhausen, Switzerland) was modified on bench using a razor blade, and attached to the non-electronic sealing piece using epoxy (as shown in Figure 3-33) to serve as the tissue anchor for suture-less implant fixation. This surgical attachment and the microfabricated sensor were assembled as the final packaged device. After being introduced to the anterior chamber, the tapered feature at the end of the retractor hook penetrates the iris and provides sufficient anchoring to the device in the implant location. This anchoring process is reversible if the implant needs to be removed from the eye.

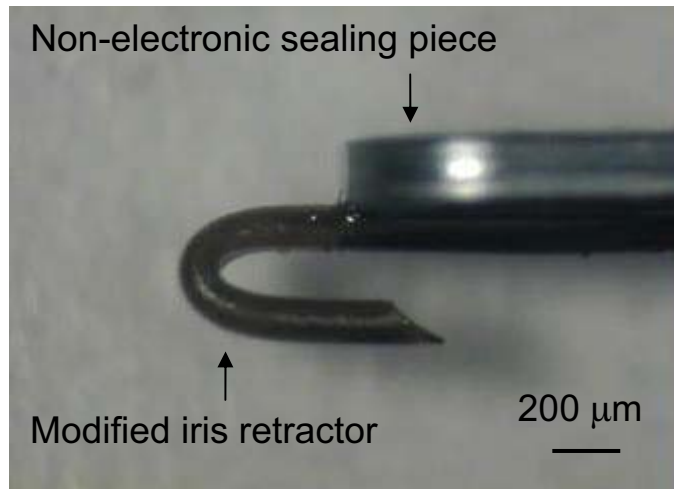


Figure 3-33: Representative iris anchor assembly result (side view)

Figure 3-34 shows the implant location in the intraocular environment after surgery using a live rabbit model. The implant was secured on the iris in the eye with the modified retractor-assembled anchor attachment. Before implantation the packaged device was conformally coated by a thin parylene layer to ensure its biocompatibility in the intraocular environment. The entire surgery was completed within 15 min because of its minimally invasive (< 2 mm incision) nature, which minimizes surgical and post-operative complications. In addition, facilitated by the compatible surgical procedures, this implant location has a tremendous advantage in aligning sensor and reader coils so that possible loss of signal strength through coil misalignment can be reduced. Follow-up study results (including fluorescein angiography and fundus photograph as shown in Figure 3-35) confirmed that no device dislocation or post-operative complications, including inflammatory response or tissue encapsulation/fibrosis, were found over 3 months, verifying the surgical/biological feasibility of using such implant paradigm with appropriate anchoring mechanism in the intraocular environment.

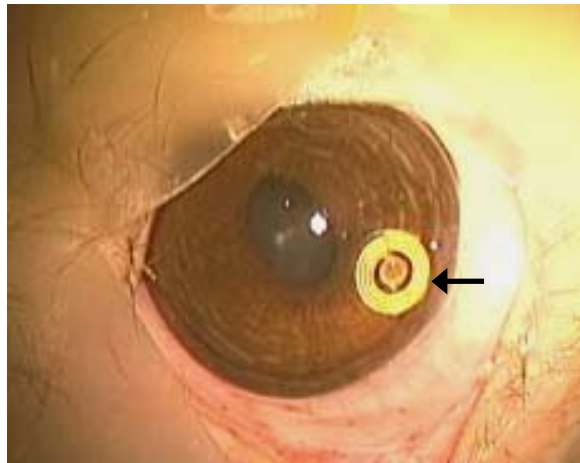
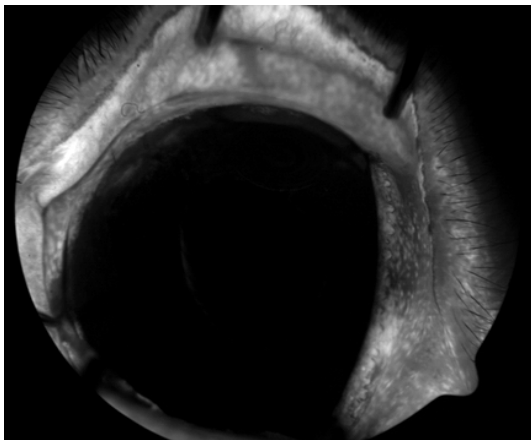
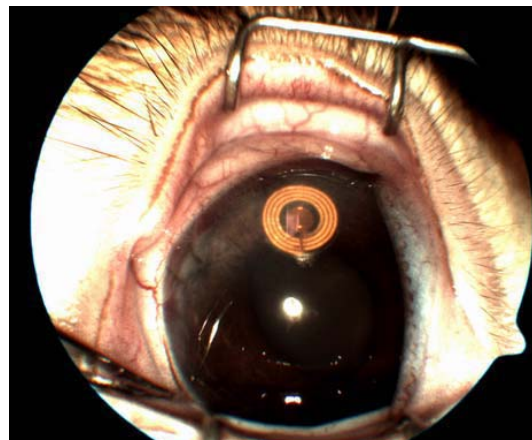


Figure 3-34: Implanted flexible-coiled pressure sensor in the intraocular environment of rabbit eye model. The arrow indicates the implant as observed through the cornea.



(a)



(b)

Figure 3-35: Follow-up study results of *in vivo* device testing using rabbit model to verify biocompatibility of the modified flexible-coiled implant. (a) Fluorescein angiogram showing no noticeable blood vessel leakage at the implantation site one week after surgery. (b) Fundus photograph showing no device dislocation or post-operative complications appeared in the intraocular environment.

In order to demonstrate the *in vivo* wireless pressure sensing feasibility of such a flexible-coiled sensor paradigm, acute animal testing using rabbit eye models was conducted with an experimental setup as shown in Figure 3-36, similar to that previously shown in Figure 3-13 except using a live rabbit and placing the sensor on the iris as in Figure 3-34, with minimally invasive surgical procedures. The obtained phase-dip curves were much clearer and more appropriate for pressure analysis as compared with those in Figure 3-14, attributable to higher SNR using the modified sensor and the developed data-processed external readout method. Although limited by the pressure control and monitoring scheme in surgical protocols at the moment of experiment such that no pressure measurement analysis could be performed, the shifted phase-dip curves correlated to a qualitatively increased IOP in the model, and markedly verified the pressure-sensing feasibility using the developed implant in the intraocular environment.

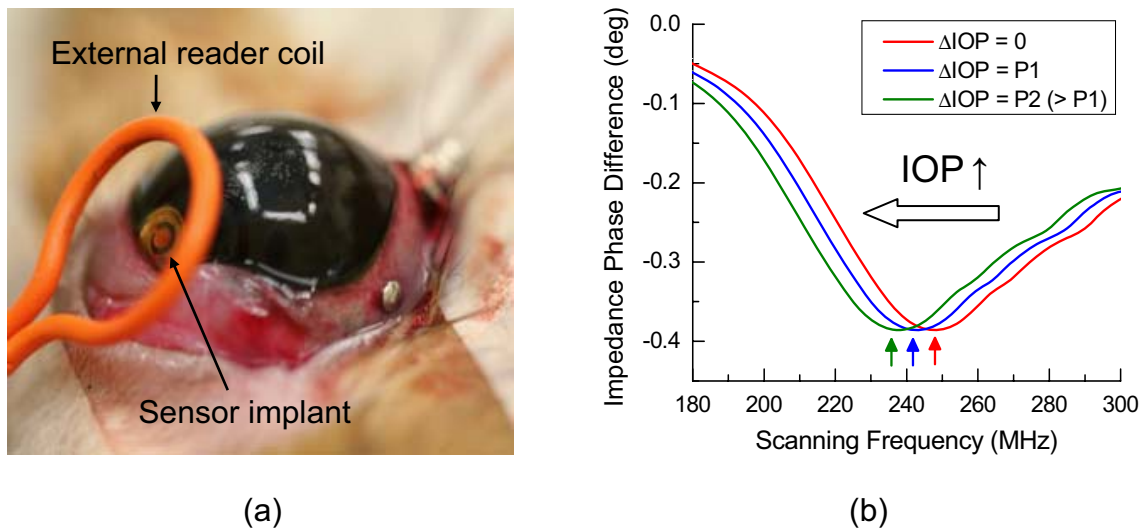


Figure 3-36: Acute *in vivo* device testing using rabbit model. (a) Photograph of experimental setup. (b) Overlay plot of the measured phase-dip curves in wireless intraocular pressure sensing.

Given the results in the acute *in vivo* testing, an improved and more quantitative *ex vivo* study was completed using an enucleated porcine eye as the animal model to characterize the pressure response of the sensor in the simulated intraocular environment. An intraocular manometer was used with the infusion-based pressurization setup in this experiment to obtain precise IOP measurements as compared with the readouts from the sensor. The results shown in Figure 3-37 were analyzed and confirmed in good agreement with the on-bench results shown in Figure 3-27, indicating that the physical pressure response of the developed sensor was consistent when situated in different environments, regardless the different electrical readouts due to the medium effect. Extensive animal studies, including acute and chronic tests, are still underway in order to completely characterize the *in vivo* performance of the flexible-coiled wireless pressure sensor paradigm. Advanced surgical protocols and tools suitable for such an implant paradigm will also be investigated to better meet the future requirements in practice.

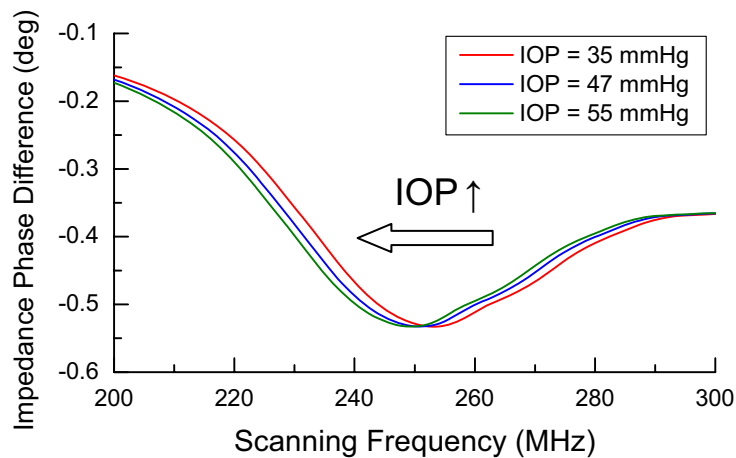


Figure 3-37: Acute *ex vivo* device testing using enucleated porcine eye model

Future work will also be focused on reader optimization and actual implementation. Development of a low-noise measurement system will be the first

keystone. As described previously, besides improvements from using the developed data-processing-based readout method from a software perspective, low-noise circuitry and techniques from a hardware perspective should be included to electronically reduce the measurement noise and enhance the SNR in phase-dip frequency detection [9, 24]. Other readout methods have also been explored in different research groups [32–34] with the aim of long-range telemetric sensing, and are valuable for comparison to the configuration proposed in this work. For example, derived from the grid-dip detection technique, a variable capacitor or a voltage-controlled oscillator (VCO) can be placed on the readout circuit to amplify the sensor response on the principle of minimizing the imaginary term of (3.3) at resonance. In this way, the sensing resolution as well as the corresponding detectable distance can be greatly improved. Other physical examples include the use of two coils on the reader side [32] to increase the electromagnetic detection zone for longer sensing distance. Moreover, in cases where either the sensor-reader coil coupling or quality factor of the sensor is substantial enough to influence the frequency shift resolution based on (3.14), some compensation method would be required as part of the final telemetric system. For example, a distance-compensated technique [35] can be applied under this concept to obtain correct frequency values regardless of possible out-of-plane positional variation between the glasses (reader) and the iris (sensor), which is valuable for further study. These developed techniques involving additional electrical components or microelectronics implementation might be incorporated into the current readout method and will be extensively studied in the future. After successful reader development, this wireless implant-based pressure sensing approach will be complete for practical continuous IOP monitoring and glaucoma study.

3.6 Summary

An implantable unpowered micromechanical parylene-based pressure sensor has been successfully developed in this chapter as part of a new implant paradigm using electrical sensing methodology to realize continuous IOP monitoring. Complete design, fabrication, and characterization of the microsensors are described. Sensors with electrical resonant circuitry in pressure-sensitive variable capacitor and variable capacitor/inductor designs were implemented to facilitate wireless pressure sensing through an inductive coupling link with an external reader. Low-temperature multi-layer polymer/metal micromachining technology enables integrated sensor components fabricated on a monolithic substrate without the need for a multi-wafer bonding process. Sensors with implantable dimensions as well as appropriate surgical features were microfabricated in a suitable form factor for intraocular implantation. Engineering and surgical/biological performance of the sensors were characterized in on-bench, *ex vivo*, and *in vivo* experiments, and shown to be in good agreement with design parameters. With the successful proof of concept and the future implementation of the proposed sensor/reader improvement strategies, this new IOP sensing paradigm has great potential for fulfilling continuous, unpowered, real-time, reliable, and convenient IOP monitoring in glaucoma patients.

3.7 Bibliography

- [1] J. W. McLaren, R. F. Brubaker, and J. S. FitzSimon, "Continuous measurement of intraocular pressure in rabbits by telemetry," *Invest. Ophthalm. Vis. Sci.*, vol. 37, pp. 966–975, 1996.
- [2] K. C. Katuri, S. Asrani, and M. K. Ramasubramanian, "Intraocular pressure monitoring sensors," *IEEE Sens. J.*, vol. 8, pp. 12–19, 2008.
- [3] W. Mokwa and U. Schnakenberg, "Micro-transponder systems for medical applications," *IEEE T. Instrum. Meas.*, vol. 50, pp. 1551–1555, 2001.
- [4] K. C. Katuri, S. Asrani, and M. K. Ramasubramanian, "Intraocular pressure monitoring sensors," *IEEE Sens. J.*, vol. 8, pp. 12–19, 2008.
- [5] Sajeeda and T. J. Kaiser, "Passive telemetric readout system," *IEEE Sens. J.*, vol. 6, pp. 1340–1345, 2006.
- [6] C. C. Collins, "Miniature passive pressure transensor for implanting in the eye," *IEEE T. Biomed. Eng.*, vol. BME-14, pp. 74–83, 1967.
- [7] L. Rosengren, P. Rangsten, Y. Bäcklund, B. Hök, B. Svedbergh, and G. Selén, "A system for passive implantable pressure sensors," *Sens. Actuat. A: Phys.*, vol. 43, pp. 55–58, 1994.
- [8] O. Akar, T. Akin, and K. Najafi, "A wireless batch sealed absolute capacitive pressure sensor," *Sensor. Actuat. A: Phys.*, vol. 95, pp. 29–38, 2001.
- [9] A. DeHennis and K. D. Wise, "A double-sided single-chip wireless pressure sensor," in *Proc. 15th IEEE Int. Conf. MEMS*, Las Vegas, NV, pp. 252–255, Jan. 20–24, 2002.

- [10] A. Baldi, W. Choi, and B. Ziaie, "A self-resonant frequency-modulated micromachined passive pressure transensor," *IEEE Sens. J.*, vol. 3, pp. 728–733, 2003.
- [11] M. A. Fonseca, M. G. Allen, J. Kroh, and J. White, "Flexible wireless passive pressure sensors for biomedical applications," in *Proc. 12th Solid-State Sensors, Actuators, and Microsystems Workshop*, Hilton Head Island, SC, pp. 37–42, Jun. 4–8, 2006.
- [12] J. Shih, J. Xie, and Y.-C. Tai, "Surface micromachined and integrated capacitive sensors for microfluidic applications," in *Proc. 12th Transducers Conf.*, Boston, MA, pp. 388–391, Jun. 8–12, 2003.
- [13] M. A. Fonseca, J. M. English, M. von Arx, and M. G. Allen, "Wireless micromachined ceramic pressure sensor for high-temperature applications," *J. Microelectromech. Syst.*, vol. 11, pp. 337–343, 2002.
- [14] F. E. Terman, *Radio Engineers' Handbook*, New York: McGraw-Hill, 1943.
- [15] T. H. Lee, *The Design of CMOS Radio-Frequency Integrated Circuits*, 2nd ed., New York: Cambridge University Press, 2004.
- [16] S. Timoshenko and S. Woinowsky-Krieger, *Theory of Plates and Shells*, 2nd ed., New York: McGraw-Hill, 1959.
- [17] A. P. Boresi and R. J. Schmidt, *Advanced Mechanics of Materials*, 6th ed., New York: John Wiley & Sons, 2003.
- [18] O. Tabata, K. Kawahata, S. Sugiyama, and I. Igarashi, "Mechanical property measurements of thin films using load-deflection of composite rectangular membranes," *Sens. Actuat. A: Phys.*, vol. 20, pp. 135–141, 1989.

- [19] W. Sim, B. Kim, B. Choi, and J.-O. Park, "Theoretical and experimental studies on the parylene diaphragms for microdevices," *Microsyst. Technol.*, vol. 11, pp. 11–15, 2005.
- [20] X. Q. Wang, Q. Lin, and Y.-C. Tai, "A parylene micro check valve," in *Proc. 12th IEEE Int. Conf. MEMS*, Orlando, FL, pp. 177–182, Jan. 17–21, 1999.
- [21] G. T. A. Kovacs, *Micromachined Transducers Sourcebook*. Boston, MA: McGraw-Hill, 1998.
- [22] C. P. Yue and S. S. Wong, "On-chip spiral inductors with patterned ground shields for Si-based RF IC's," *IEEE J. Solid-St. Circ.*, vol. 33, pp. 743–752, 1998.
- [23] H.-S. Noh, C. Bonner, P. J. Hesketh, and G. C. Frye-Mason, "Fabrication of parylene column for micro gas chromatograph," presented at The 7th Mechatronics Forum International Conference, Atlanta, GA, Sep. 6–8, 2000.
- [24] A. D. DeHennis, "Remotely-powered wireless monitoring systems," Ph.D. dissertation, Dept. Electr. Eng., Univ. Mich., Ann Arbor, MI, 2004.
- [25] A. V. Oppenheim and A. S. Willsky, *Signals & Systems*, 2nd ed. Upper Saddle River, NJ: Prentice Hall, 1997.
- [26] P.-J. Chen, W.-C. Kuo, W. Li, Y.-J. Yang, and Y.-C. Tai, "Q-enhanced fold-and-bond MEMS inductors," in *Proc. 3rd IEEE Int. Conf. NEMS*, Sanya, China, pp. 869–872, Jan. 6–9, 2008.
- [27] F. C. Flack, E. D. James, and D. M. Schlapp, "Mutual inductance of air-cored coils: Effect on design of radio-frequency coupled implants," *Med. Biol. Eng.*, vol. 9, pp. 79–85, 1971.

- [28] W. H. Ko, S. P. Liang, and C. D. F. Fung, "Design of radio-frequency powered coils for implant instruments," *Med. Biol. Eng. Comput.*, vol. 15, pp. 634–640, 1977.
- [29] D. K. Cheng, *Field and Wave Electromagnetics*, 2nd ed., Reading, MA: Addison-Wesley, 1989.
- [30] A. Nyshadham, C. L. Sibbald, and S. S. Stuchly, "Permittivity measurements using open-ended sensors and reference liquid calibration—an uncertainty analysis," *IEEE T. Microw. Theory*, vol. 40, pp. 305–314, 1992.
- [31] J.-M. Kim, D. H. Oh, J.-H. Park, J.-W. Cho, Y. Kwon, C. Cheon, and Y.-K. Kim, "Permittivity measurements up to 30 GHz using micromachined probe," *J. Micromech. Microeng.*, vol. 15, pp. 543–550, 2005.
- [32] K. G. Ong, C. A. Grimes, C. L. Robbins, and R. S. Singh, "Design and application of a wireless, passive, resonant-circuit environmental monitoring sensor," *Sens. Actuat. A: Phys.*, vol. 93, pp. 33–43, 2001.
- [33] J. Coosemans, M. Catrysse, and R. Puers, "A readout circuit for an intra-ocular pressure sensor," *Sens. Actuat. A: Phys.*, vol. 110, pp. 432–438, 2004.
- [34] S. F. Pichorim and P. J. Abatti, "A novel method to read remotely resonant passive sensors in biotelemetric systems," *IEEE Sens. J.*, vol. 8, pp. 6–11, 2008.
- [35] D. Marioli, E. Sardini, M. Serpelloni, and A. Taroni, "A new measurement method for capacitance transducers in a distance compensated telemetric sensor system," *Meas. Sci. Technol.*, vol. 16, pp. 1593–1599, 2005.

CHAPTER 4

IMPLANTABLE PARYLENE-BASED INTRAOCULAR PRESSURE SENSORS WITH OPTICAL READOUTS

4.1 Overview

This chapter presents an implantable, unpowered, parylene-based wireless MEMS pressure sensor for IOP monitoring in an optical sensing paradigm to investigate its feasibility and possibility other than the electrical sensing paradigm described in Chapter 3. From *in situ* mechanical deformation of the compliant spiral-tube structures, this sensor can register pressure variations without electrical or powered signal transduction. Micromachined high-aspect-ratio polymeric hollow tubes are implemented to obtain high-sensitivity pressure responses. An integrated device packaging method has been

developed to enable minimally invasive suture-less needle-based implantation of the device. *In vitro* and *ex vivo* device characterizations have successfully demonstrated 1 mmHg resolution of the pressure responses, along with verifications of biocompatibility and fixation functionality of the implant in the intraocular environment. Facilitated by the implantation scheme, the pressure response of the implant can be directly and optically observed from outside the eye under visible light, with the goal of realizing convenient, direct, and reliable IOP monitoring in glaucoma patients.

4.2 Implant Design

4.2.1 Sensing scheme

This implant facilitates an optical pressure-sensing technology by using a micromechanical sensor with observable deformation to environmental pressure variations. When the sensor is implanted on the iris of the eye, its *in situ* mechanical pressure response corresponding to the IOP variation can be observed with an optical reader—as straightforward as a camera, a microscope, or a stereoscope—from outside the eye through the transparent cornea without the need for electrical circuitry or external powered signal transduction. The device is fabricated in a small form factor suitable for minimally invasive suture-less implantation. Similarly to telemetric sensing, this optical methodology has the potential of enabling a patient to read his/her own IOP (e.g., using his/her one eye to observe the other where the sensor is implanted through a special binocular reader) instead of clinical visits, resulting in more practical and convenient continuous IOP tracking. Sensing distance and pressure readout resolution depend on the depth of focus and optical magnification from the external reader to the sensor implant.

4.2.2 Sensor design

The IOP sensing element, as shown in Figure 4-1, is a high-aspect-ratio compliant structure inspired by a Bourdon tube, a free-standing curved hollow tube [1, 2]. It has a systematic, well-defined pressure response on its mechanical conformation. The tube deforms to respond to a bending moment generated by a pressure difference applied between the pressure encapsulated in the tube/channel and the ambient pressure. The deformation, which can be visualized by movement of the pointing tip at the free end of the tube, is linearly related to this pressure difference. Therefore, the corresponding environmental pressure outside the tube can be measured, given that the pressure inside the tube is set at a predetermined constant. Because of the visible tube deformation after implantation, direct IOP measurements can be obtained through optical observation. Variation in IOP can occur due to reasons such as treatment of underlying disease, diurnal rhythm, and atmospheric pressure change. All of these changes would be accurately detected by the sensor. Different geometric designs can be used to amplify the tube deformation as well as modify its in-plane deformation trajectories. Table 4-1 gives possible layouts of the IOP sensor design. Improved from the basic Bourdon tube design, an Archimedean spiral layout can be utilized to increase the angular rotation at the end pointing tip as well as a long-armed spiral tube used to further enhance the lateral movement of the end arm. These tube geometries can both enlarge the pressure sensitivity and optimize the device dimensions for suture-less clinical implantation using small outer-diameter needles. Moreover, the minimized out-of-plane deformation using these symmetric tube designs leads to more accurate pressure readouts in optical observation of the sensor implant.

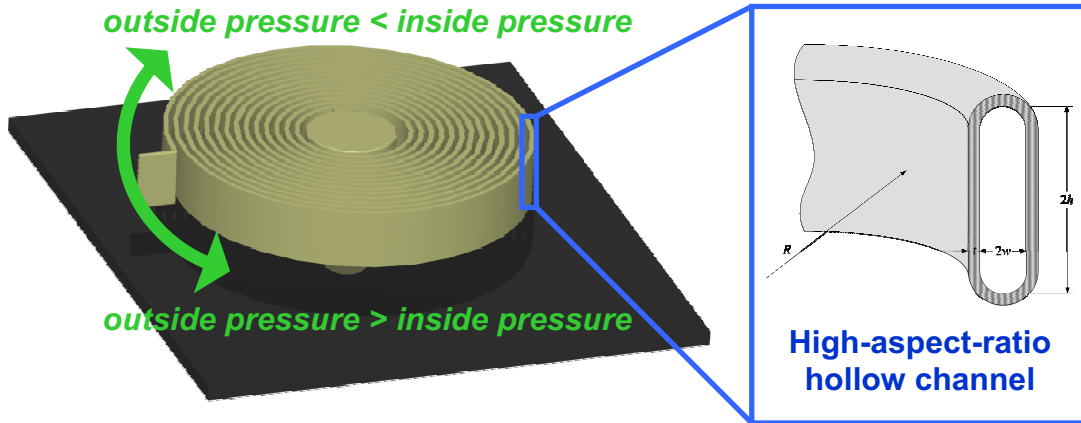
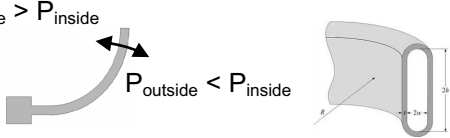
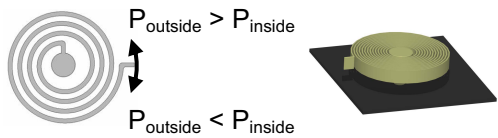
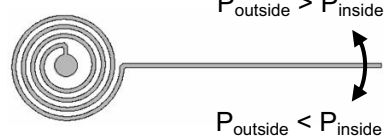


Figure 4-1: Concept of the micromechanical IOP sensor for optical sensing. Different directions of tube rotation result from different pressure conditions across the tube.

Table 4-1: Geometric designs of compliant structures for the IOP sensor

Curved tube (<i>Basic Bourdon tube</i>)	$P_{\text{outside}} > P_{\text{inside}}$ 
Spiral tube (<i>Angular deformation</i>)	
Long-armed tube (<i>Amplified rotation</i>)	

As the main component of the IOP sensor, the thin-walled hollow tube needs to be flexible for more sensitive pressure responses and higher sensing resolution. Conceptually, higher-aspect-ratio tubes in a specific shape (e.g., elliptical or rectangular

cross-section) are necessary to obtain larger in-plane deformations and stronger out-of-plane resistance to environmental interference. Parylene C is selected as the structural material for the tube because of its desirable properties, including mechanical flexibility, chemical inertness, and biocompatibility, as described in the Appendix. More importantly, its pinhole-free thin-film conformal coating ability enables fabrication of high-aspect-ratio hollow tubes in single material layer. These factors support utilization of parylene for such flexible and implantable biomedical microdevice.

4.2.3 Device packaging

Because the pressure sensor is designed to be implanted inside the eye for direct IOP measurement, packaging is necessary to ensure that the IOP sensor is fully functional after implantation. In order to avoid handling and alignment issues during assembly, a wafer-level integrated device packaging method has been developed. By implementing micromachining technology, a fully packaged device comprising the following components can be fabricated on a monolithic substrate as shown in Figure 4-2: 1) a sensor platform to support the IOP sensor; 2) bottom posts with an end “anchoring feet” design to realize suture-less anchoring of the implant on the iris [3]; and 3) a perforated flexible parylene membrane to protect the sensor from damage during implantation. With these features, a packaged device can be implanted on the iris so that faithful IOP readouts from the sensor are observable from outside the eye through the cornea and the protective parylene membrane. The resulting implant fixation method also obviates the use of sutures while additionally favoring a minimally invasive implantation scheme that curtails complications during and after surgery.

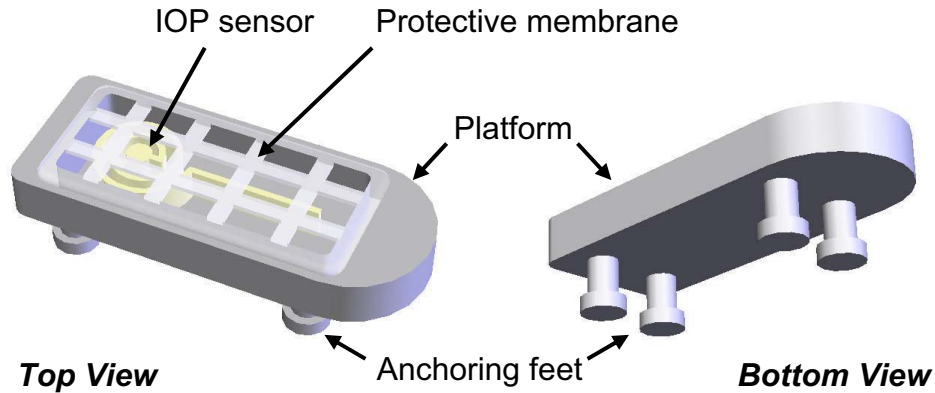


Figure 4-2: Schematics of fully packaged implantable device (not to scale)

4.3 Device Fabrication

Two types of IOP sensors, high-sensitivity and needle-implantable, were microfabricated. The high-sensitivity sensor is a simplified version that includes only the parylene tube, while the needle-implantable sensor has a smaller form factor and has all necessary components for implantation: The parylene tube, the top protective membrane, and the bottom tissue anchoring structures. All sensors were microfabricated on a monolithic substrate to accomplish integrated device packaging. Figure 4-3 illustrates the fabrication process of the needle-implantable sensors. The process began with growing a 0.75- μm -thick wet oxide on a 500- μm -thick double-side-polished silicon wafer. After patterning the backside oxide using buffered hydrofluoric acid and photoresist as a mask, backside two-step DRIE in a PlasmaTherm™ SLR system was performed to define the backside access holes, as well as 200- μm -high feet anchors and trench boundaries of the sensor platform. A novel embedded channel fabrication technology was then employed to create the high-aspect-ratio quasi-rectangular parylene channels [4]. With frontside

oxide patterning, two-step complementary plasma-based dry etching, and an 8- μm -thick parylene C deposition, 180- μm -high, 16.5- μm -wide thin-walled embedded channels with 5- μm -thick parylene walls were successfully fabricated. Channels with an internal channel aspect-ratio of approximately 26 with a quasi-rectangular profile, where the sidewall angle $\sim 90^\circ \pm 1^\circ$, were obtained to achieve large mechanical responses. The backside holes located at the center of the tubes were also connected to the inside of the parylene channels after the frontside trench etching. These holes would be sealed after device fabrication to encapsulate air at a constant pressure inside the tubes. Oxygen plasma etching with a photoresist etch mask was performed to separate the embedded parylene channels into tube patterns with various geometric designs (spiral tube and long-armed tube described above). Subsequent to removal of the remaining frontside oxide, a sacrificial photoresist layer was spin-coated and the second parylene C layer was deposited and patterned to construct a 10- μm -thick perforated parylene membrane caging the channels from 20 μm above. Finally, the photoresist was stripped with acetone and the parylene channels were released using an isotropic gas-phase XeF_2 silicon etch in a customized system. Using the same through-wafer technique, the entire microdevice was separated from the wafer substrate after XeF_2 etching without dicing while the main body of the device remained intact due to protection from the parylene-filled trenches depicted in Figure 4-3. A thin layer of parylene could be further coated on the released device to promote its biocompatibility.

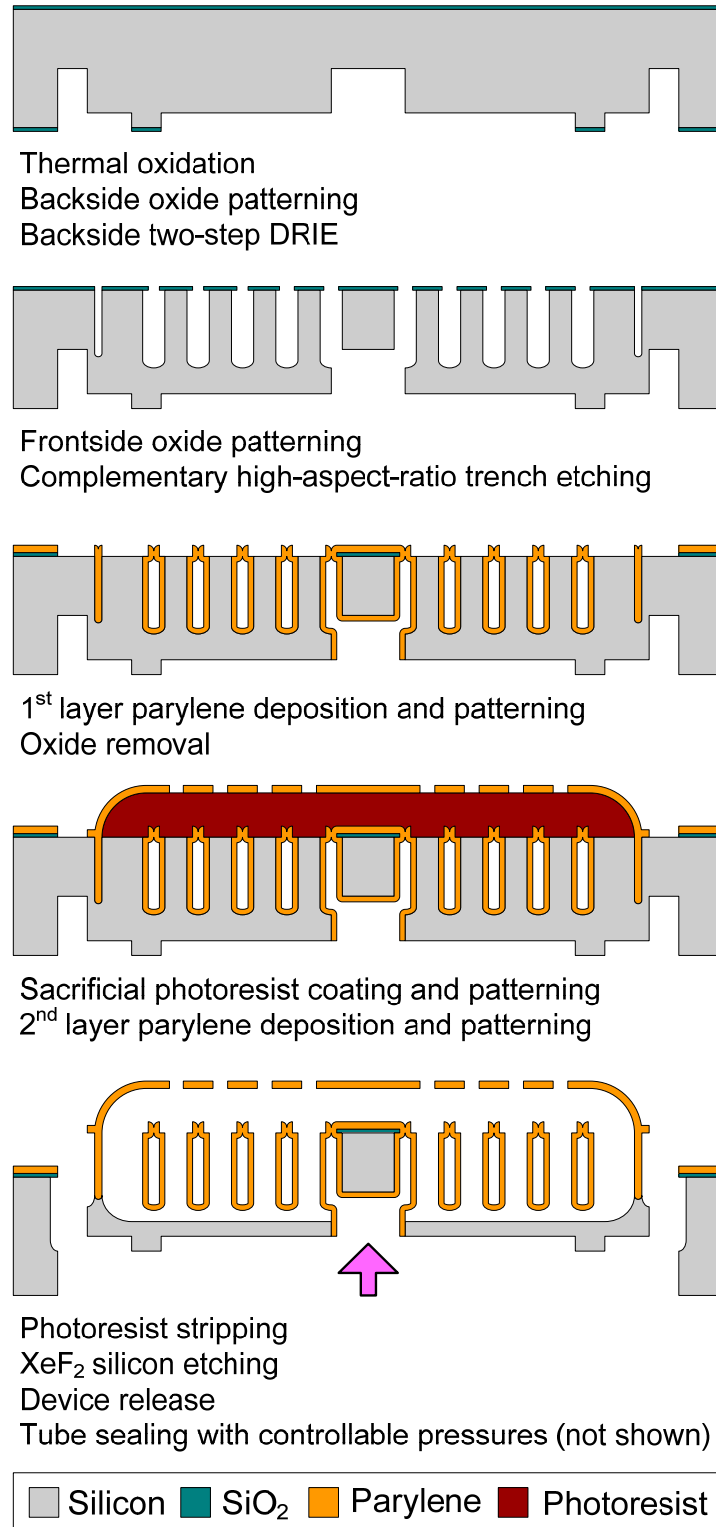


Figure 4-3: Fabrication process flow of the needle-implantable sensors as example. The arrow indicates the location of sealing to parylene tube.

Figure 4-4 shows the high-sensitivity IOP sensors micromachined using only the parylene tube fabrication process. Sensors of both the spiral-tube and long-armed-tube design were successfully fabricated. Note that the indicators surrounding the sensors were fabricated at the same time to accurately determine the position of the end pointing tip. Micromachined integrated packaging components for the needle-implantable IOP sensors before the final XeF_2 device release are shown in Figure 4-5. The embedded IOP sensors are clearly observable through the top perforated protective membranes due to the optical transparency of parylene. An excessively long leverage arm should be avoided as it has a substantial mechanical resistance and thus affects the rotational behavior of the spiral tube. Instead, a pair of long-armed-tube sensors could be placed in the same platform to effectively double the pressure-related movement by observing the distance between the pointing tips. This “rotation-tip” readout amplification method is promising, but requires delicate calibration of the residual stress in the parylene structures for good alignment of the pointing tips after tube release [5–7]. Compared with the spiral-tube sensors, the long-armed-tube sensors were better suited for fabrication in a form factor that can be accommodated inside a 19-gauge needle, as shown in Figure 4-6, while still achieving a reasonable pressure response.



Figure 4-4: Microfabricated high-sensitivity parylene-based IOP sensors in spiral-tube (left) and long-armed-tube (right) designs

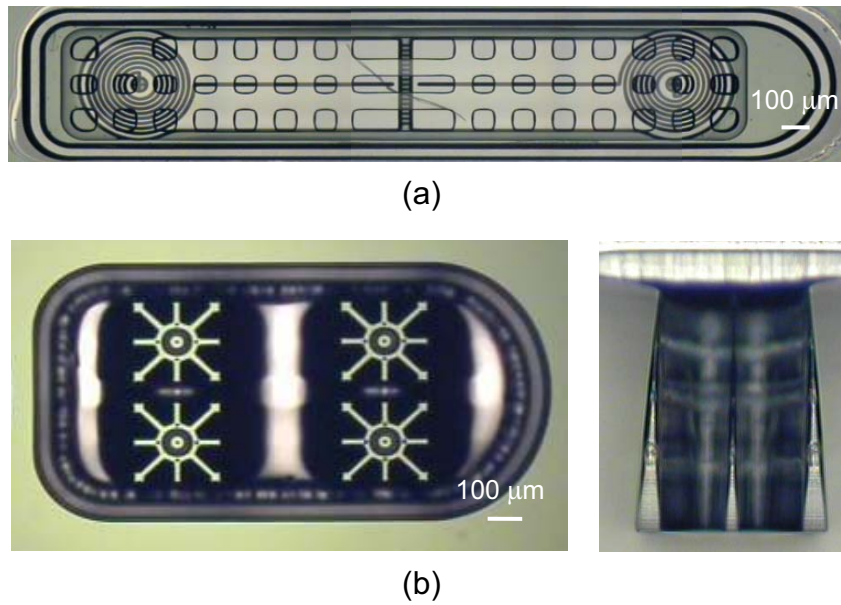


Figure 4-5: Integrated packaging components of the needle-implantable parylene-based IOP sensors. (a) Micrograph of the parylene tube in long-armed-tube design under the perforated parylene membrane before final device release (top view). (b) Example of the backside tissue anchor with its top (left) and side (right; 200 μm in height) views

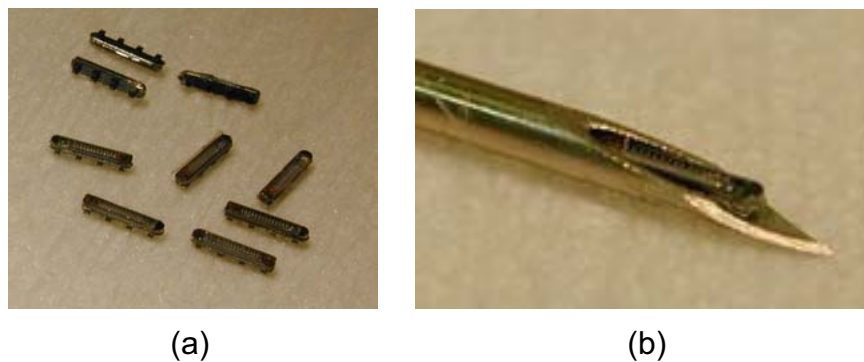


Figure 4-6: Microfabricated needle-implantable parylene-based IOP sensors. (a) Released devices. (b) A device implant situated inside a 19-gauge hypodermic needle

The important physical dimensions of the microfabricated IOP sensors characterized in the following sections are listed in Table 4-2.

Table 4-2: Design metrics of the fabricated micromechanical IOP sensors

Tube design	High-sensitivity sensors (large form factor)		Needle-implantable sensors (small form factor)
	Spiral tube	Long-armed tube	Long-armed tube
Overall size	$2 \times 2 \times 0.5 \text{ mm}^3$	$4 \times 2 \times 0.5 \text{ mm}^3$	$3 \times 0.6 \times 0.5 \text{ mm}^3$
Spiral diameter	$\sim 1,100 \text{ }\mu\text{m}$	$\sim 1,100 \text{ }\mu\text{m}$	$\sim 400 \text{ }\mu\text{m}$
Spiral turns	15	15	8
Pointing tip length	$100 \text{ }\mu\text{m}$	$1,500 \text{ }\mu\text{m}$	$750 \text{ }\mu\text{m}$
Indicator separation	5°	$80 \text{ }\mu\text{m}$	$20 \text{ }\mu\text{m}$

4.4 Characterization Results and Discussions

4.4.1 *In vitro* pressure sensing test

The microfabricated parylene-based pressure sensors were first tested on-bench to characterize their *in vitro* pressure responses. All parylene tubes were sealed by applying epoxy over the backside access holes under atmospheric pressure (1 atm) at room temperature; this served as the gauge reference pressure. A customized pressure regulation setup (as shown in Figure 4-7) was used to vary the environmental pressure surrounding the sensors, in which a off-chip pressure regulator and a pressure gauge were used to control the pressurization with 0.5 mmHg tuning resolution. Structural deformation of the sensors with respect to different positive pressures was measured using a stereoscope and compared with numerical readouts from a pressure gauge. Because the parylene tube structures are strengthened by their high-aspect-ratio shape, the sensors were not affected by stiction on their underside to the platform and were completely functional in both air and liquid media. Prior to immersion and operation in liquid, however, the sensors need to experience appropriate surface treatments such as short oxygen plasma roughening in order to reduce the severity of bubble formation on

polyethylene surfaces [7], which can result in device failure. The pressure testing of the sensors was conducted in water to mimic the intraocular environment. For the high-sensitivity sensors, the testing results shown in Figure 4-8 indicate that their pressure sensitivity was $0.47^\circ/\text{mmHg}$ in rotational displacement with the spiral-tube design and $11.23\ \mu\text{m}/\text{mmHg}$ in lateral displacement with the long-armed-tube design, both showing a continuous pressure response (i.e., continuous pointing tip rotation) with high linearity. These data further verify that different geometric tube layouts result in different trajectories of tube deformation. The pressure sensing resolution was approximately 3.56 mmHg obtained with the long-armed-tube sensors, which falls in the range of interest for IOP measurements. This resolution was determined by the confidence of observation of tip movement through half the distance between 80- μm -spaced indicators. Therefore, even without redesigning the polyethylene tube structure, higher pressure resolution could be achieved using indicators with a smaller separation and optical readers with higher magnification. This fact leaves room to further optimize the micromechanical pressure sensor. The needle-implantable sensors with long-armed-tube design also demonstrated a $3.21\ \mu\text{m}/\text{mmHg}$ pressure sensitivity in lateral displacement, as shown in Figure 4-9.

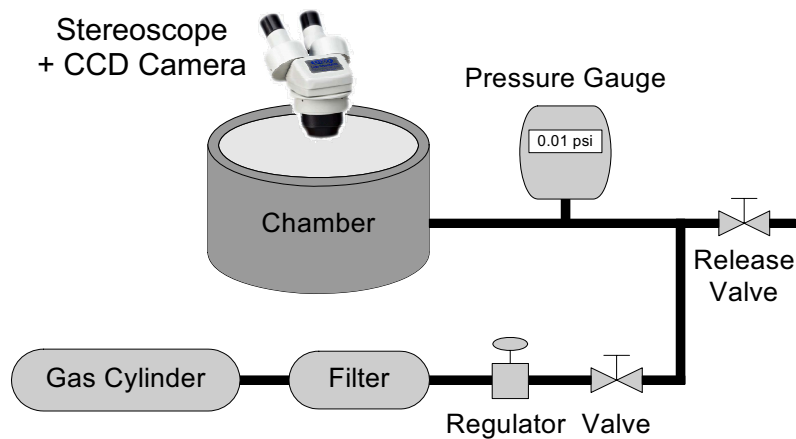


Figure 4-7: Schematic of on-bench pressure testing setup for device characterization

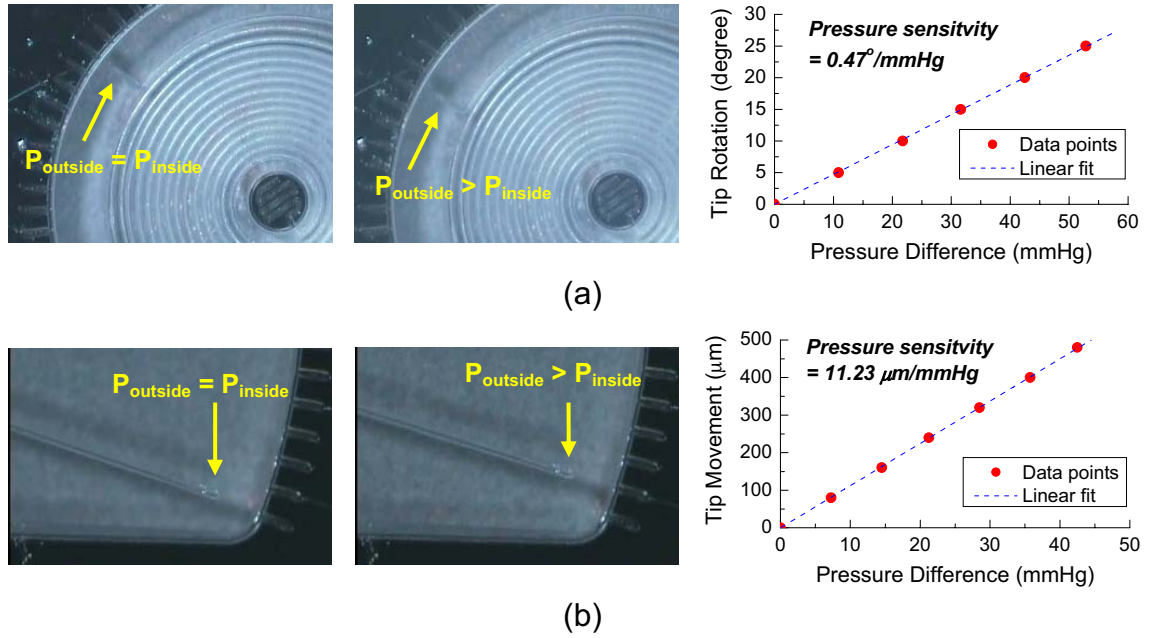


Figure 4-8: *In vitro* pressure response of the high-sensitivity IOP sensors in water. (a) Spiral-tube design. (b) Long-armed tube design. The figures include snapshots of tip movements before and after pressurization and associated measurement data.

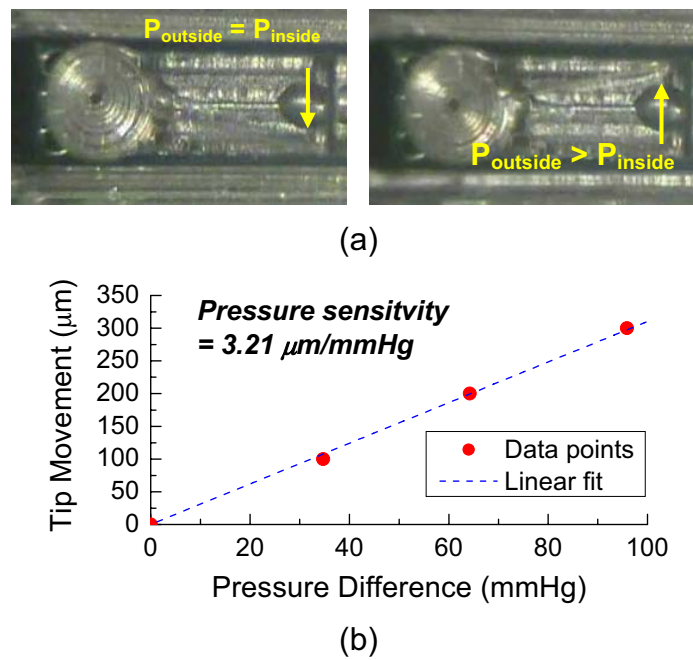


Figure 4-9: *In vitro* pressure response of the needle-implantable IOP sensors in water. (a) Snapshots of tip movement before and after pressurization. (b) Measurement data

4.4.2 *In vivo* anchoring test

The micromachined tissue anchors have been studied to evaluate their *in vivo* efficacy under normal conditions in a rabbit eye model. All devices were sterilized using ethylene oxide gas prior to their implantation through a small angled razor blade incision at the cornea of the rabbit eyes. The dummy silicon substrate with three anchoring feet (all components coated with approximately 1.5 μm of parylene C) were implanted using forceps and gently depressed from above to embed the anchors in the iris. After retraction of the forceps, no additional steps such as suturing procedures were necessary to close the corneal incision. The entire implantation was completed in an extremely short time period, typically less than 5 minutes. As observed in Figure 4-10, after 1 month of surgery, there was no device movement detectable in either of the rabbits implanted with the crossed anchor design illustrated in Figure 4-5. Furthermore, the follow-up fluorescein angiography over the month showed only very minimal leakage of blood in the iris, indicating that the anchors caused only minor trauma to the iris during implantation and this leakage diminished over time.

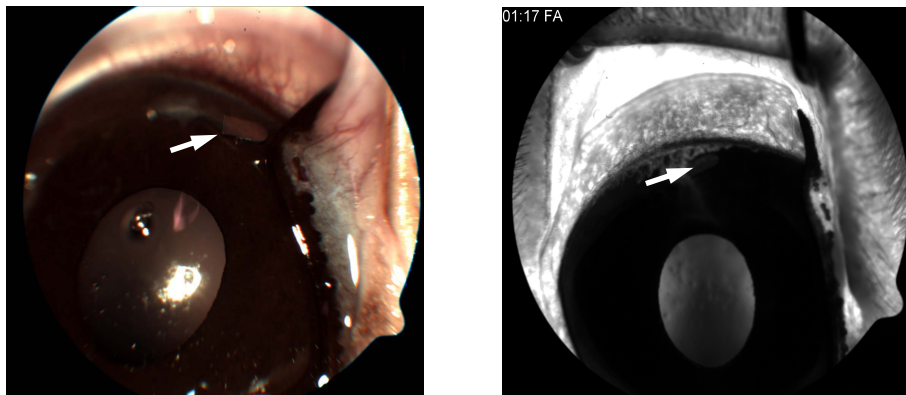


Figure 4-10: *In vivo* anchoring test with fundus photograph (left) and fluorescein angiogram (right) taken after 1 month of study. The arrows indicate the implant location.

4.4.3 *Ex vivo* pressure sensing test

Implantation testing has been conducted in several enucleated porcine eyes to characterize the expected *in vivo* performance of the IOP sensors. For the high-sensitivity sensors, an angled blade incision and corneal suturing were performed to implant the devices due to their large physical dimensions. Test results demonstrate that both the spiral-tube and long-armed-tube designs successfully registered IOP variations in the intraocular environment under external observation with a surgical microscope with approximately $2.4\times$ magnification. Repeatable pressure responses of the sensors were confirmed by applying cyclic pressure variations. Figure 4-11 shows that a real-time $8.72\text{ }\mu\text{m/mmHg}$ sensitivity was obtained in the long-armed-tube sensors, proving the microfabricated IOP sensors can achieve pressure sensing at the mmHg level in the intraocular environment. The needle-implantable sensors, in spite of their minimally observable pressure responses due to low optical magnification of the scope, were successfully implanted using a 19-gauge needle shown in Figure 4-12.

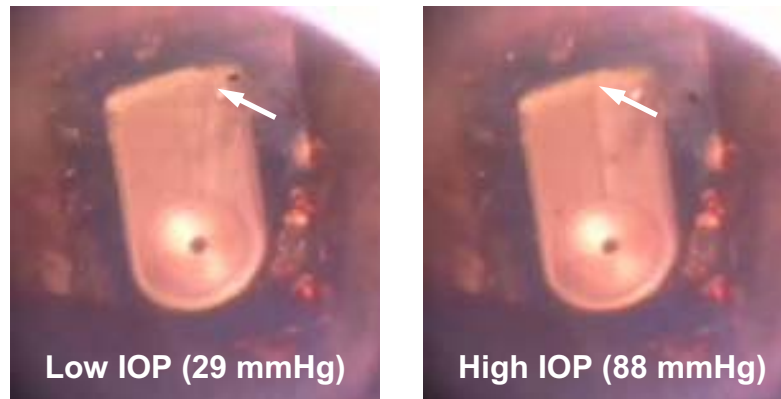


Figure 4-11: *Ex vivo* pressure response of the high-sensitivity long-armed-tube IOP sensor. The arrow indicates the position of the end pointing tip which changes with respect to the pressure variations in the intraocular environment.

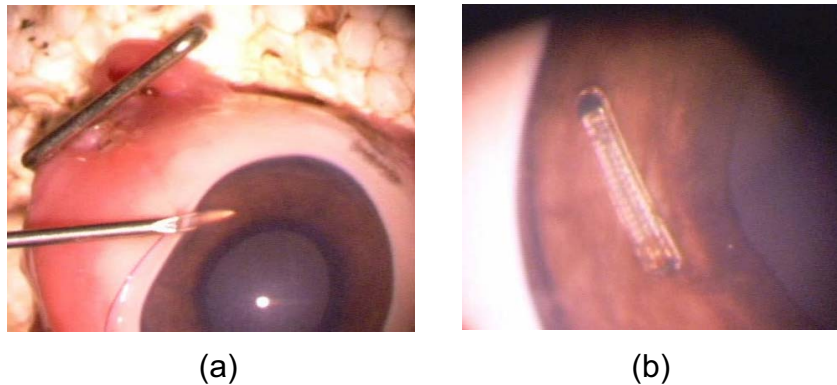


Figure 4-12: *Ex vivo* characterization of the needle-implantable IOP sensor. (a) Device implantation through a needle incision. (b) Device implanted inside the eye. The tissue anchors mechanically secure the device on the iris in the intraocular environment.

4.4.4 *In vivo* implantation test

As another proof-of-concept demonstration, the needle-implantable pressure sensors were implanted in rabbit eyes and examined over time to evaluate their biostability. Over the 2-week follow-up period, one device still maintained its position as shown in Figure 4-13 while another dislodged, possibly due to the large number of anchors in the middle of the device preventing good contact of the ends of the device with the iris. Other than that, after 2 weeks, fluorescein angiography (as shown in Figure 4-13) confirmed only minimal leakage of blood around the device, again indicating only minor trauma to the iris. Devices that were completely coated in parylene showed almost no tissue encapsulation as compared to those with exposed silicon surfaces, which produced a discernable tissue response. Future work will center on determining the optimal anchor number and geometry for more reliable device implantation in the intraocular environment, and on increasing pressure sensitivity of the implant in a smaller form factor for more practical IOP monitoring.

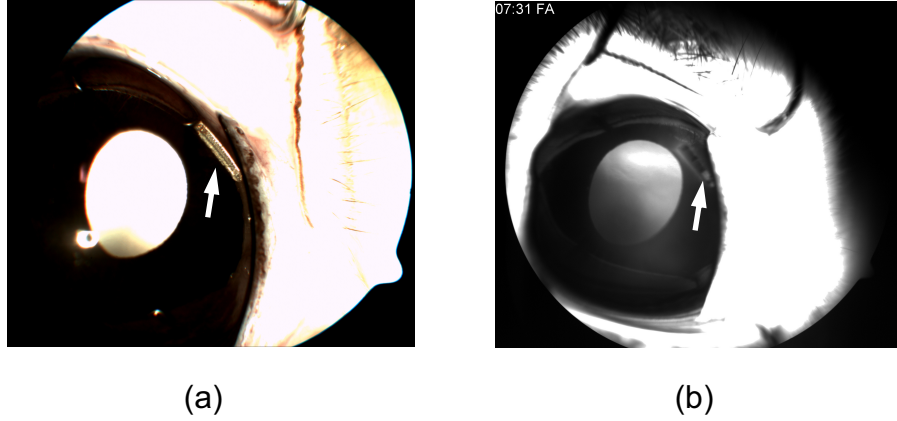


Figure 4-13: *In vivo* animal study using rabbit eyes with functional needle-implantable IOP sensor. (a) One week after implantation with no device dislocation. (b) Two weeks after implantation with fluorescein angiogram showing minimal blood leakage

4.4.5 Temperature effect characterization

Because the device is in gauge pressure sensing configuration where encapsulated air is involved as the pressure reference, the performance of such spiral-tube sensor would have temperature effect [8], as shown in Figure 4-14. This behavior needs to be studied as the temperature in the intraocular environment can vary with human body temperature ($\pm 1^\circ\text{C}$ in normal maximum). When the air inside the tube is sealed, its pressure changes as a function of temperature based on the ideal gas law:

$$PV = nRT, \quad (4.1)$$

where P and V are the pressure and volume in the closed system, n is the number of moles of gas particles, R is the universal gas constant, and T is the environmental temperature. Obviously, this effect explains that a temperature change inside the tube can lead to a pressure difference across the tube in a fixed air volume, so that the tube deformation is also correlated with environmental temperature variation.

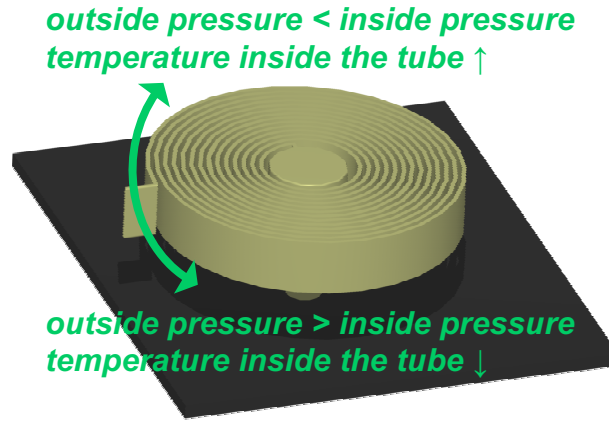


Figure 4-14: Illustration of temperature effect on the IOP sensor. Directions of tube rotation by temperature variation are correlated to the pressure difference across the tube.

In order to characterize this temperature effect, a test structure having a 40-mm-long, 17-turn spiral tube out of a 190- μm -deep, 12- μm -wide, 3- μm -thick-walled high-aspect-ratio (internal channel height/channel width greater than 30) parylene channel was fabricated, as shown in Figure 4-15. The parylene spiral tube was sealed by applying epoxy on the backside access hole under 1 atm at 20°C to provide the pressure and temperature references. Other than pressure testing, temperature testing was conducted by observing the device immersed in a temperature-controlled water environment (as shown in Figure 4-16) to ensure uniform temperature distribution of the parylene spiral tube with 0.1°C tuning resolution, using a combination of a programmable heat control stage as a heat generation source and a thermal couple as a temperature measurement unit. Experimental data (as shown in Figure 4-17) indicate linear responses of tube rotation in both pressure and temperature testing. A 1.92°/mmHg pressure sensitivity and a 6.28°/°C temperature sensitivity were obtained in a good agreement with each other through conversion using the ideal gas relation, which confirms the fact that

environmental temperature fluctuation influences tube deformation by essentially creating intrinsic pressure difference inside the tube. This characterization result must be incorporated in future sensor design for consistent pressure-sensing accuracy under controlled temperature influence. In fact, the following two methods can be used to reduce the effect of temperature variation in the intraocular environment: 1) seal the parylene tube at low pressure or even in vacuum (as in absolute pressure sensors) to weaken the pressure-temperature coupling; and 2) implement a sensor-pair configuration with different pressure reference as shown in Figure 4-18 for temperature compensation in the readouts [8]. Because pressure and temperature readouts can be decoupled and respectively obtained in the sensor-pair configuration, such a micromechanical sensor paradigm also has the potential for both continuous pressure and temperature monitoring in various systems, especially with long-term environmental monitoring needs.

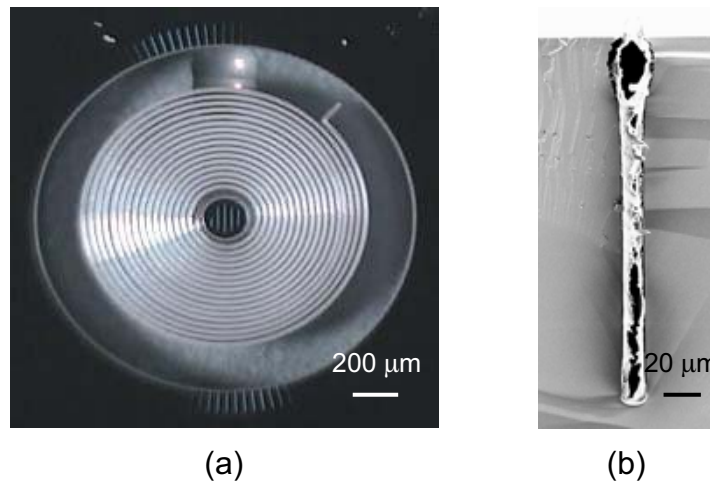


Figure 4-15: Parylene spiral tube for temperature effect characterization. (a) Stereoscope image of the free-standing tube (top view). (b) SEM image of the high-aspect-ratio parylene channel before final release (cross-sectional view). The parylene layer was improperly delaminated due to chip cleavage.

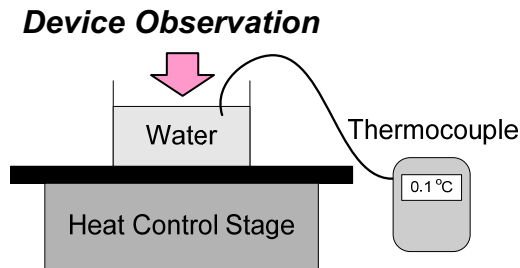


Figure 4-16: Schematic of on-bench temperature testing setup

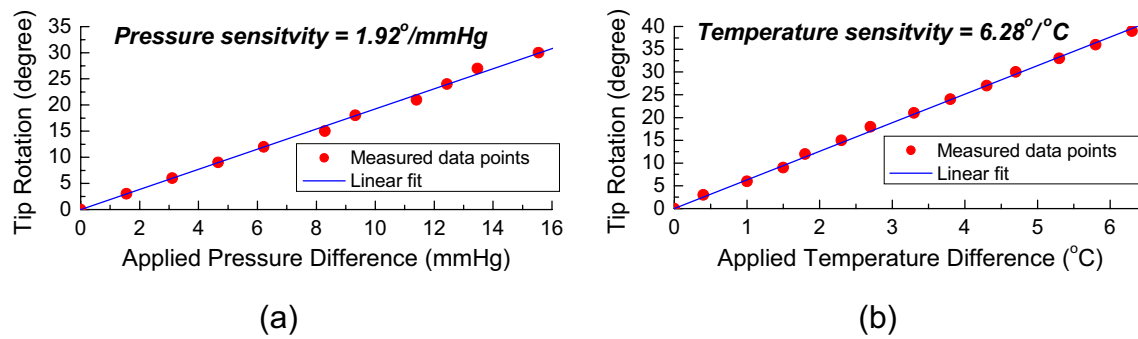


Figure 4-17: Characterization results. (a) Pressure testing. (b) Temperature testing. Linear measurement data indicate linearly continuous pressure and temperature responses of the spiral-tube sensor.

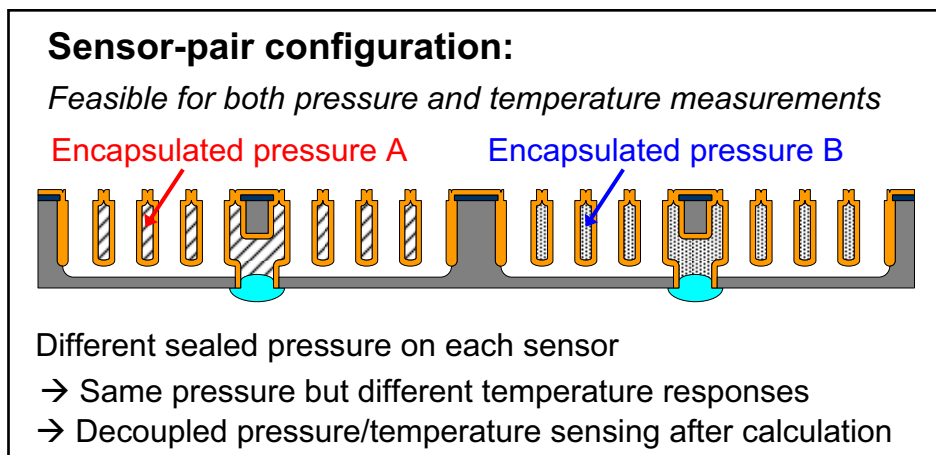


Figure 4-18: Concept of sensor-pair configuration. Illustration adapted from [8].

4.5 Summary

An implantable unpowered micromechanical parylene-based pressure sensor has been successfully developed in this chapter as part of a new implant paradigm using optical sensing methodology to realize continuous IOP monitoring. Various geometric layouts for micromachined high-aspect-ratio flexible thin-walled tubes including a spiral-tube and a long-armed-tube design have been implemented to realize pressure sensing with different deformation trajectories. Depending on the target application, these devices are designed in a relatively large form factor to achieve high-sensitivity pressure responses, and in a small form factor to enable minimally invasive implantation through a needle. Monolithic fabrication and packaging of the microdevices have been successfully demonstrated. The micromachined IOP sensors were characterized *in vitro* and *ex vivo*, as well as *in vivo*. Testing results have yielded positive results toward practical IOP readouts at the mmHg level along with suture-less device anchoring after needle-based implantation. Long-term performance of the parylene spiral-tube pressure sensors will need to be characterized to verify the stability of their behavior in the intraocular environment. Such proposed optical IOP sensing method is more straightforward and economical than the proposed electrical sensing method as described in Chapter 3, and thus be a valuable focus for more studies in the future. With appropriate optical reader implementation, this paradigm has the great potential of fulfilling continuous, unpowered, real-time, reliable, and convenient IOP monitoring in glaucoma patients.

4.6 Bibliography

- [1] R. A. Clark and E. Reissner, "Deformations and stresses in Bourdon tubes," *J. Appl. Phys.*, vol. 21, pp. 1340–1341, 1950.
- [2] K. H. Chau, R. Goehner, E. Drubetsky, H. M. Brady, W. H. Bayles Jr., and P. C. Pedersen, "Pressure and sound measurement," in *The Measurement, Instrumentation, and Sensors Handbook*, J. G. Webster, Ed., Boca Raton, FL: CRC Press, 1999.
- [3] E. Meng, P.-J. Chen, D. Rodger, Y.-C. Tai, and M. Humayun, "Implantable parylene MEMS for glaucoma therapy," in *Proc. 3rd IEEE-EMBS Int. Spec. Top. Conf. MMB*, Oahu, HI, pp. 116–119, May 12–15, 2005.
- [4] P.-J. Chen, C.-Y. Shih, and Y.-C. Tai, "Design, fabrication, and characterization of monolithic embedded parylene microchannels in silicon substrate," *Lab Chip*, vol. 6, pp. 803–810, 2006.
- [5] B. P. van Drieënhuizen, J. F. L. Goosen, P. J. French, and R. F. Wolffenbuttel, "Comparison of techniques for measuring both compressive and tensile-stress in thin-films," *Sensor. Actuat. A: Phys.*, vol. 37–38, pp. 756–765, 1993.
- [6] T. A. Harder, T.-J. Yao, Q. He, C.-Y. Shih, and Y.-C. Tai, "Residual stress in thin-film parylene C," in *Proc. 15th IEEE Int. Conf. MEMS*, Las Vegas, NY, pp. 435–438, Jan. 20–24, 2002.
- [7] T.-J. Yao, "Parylene for MEMS applications," Ph.D. dissertation, Dept. Elect. Eng., Calif. Inst. Technol., Pasadena, CA, 2002.
- [8] P.-J. Chen and Y.-C. Tai, "A micromechanical parylene spiral-tube sensor and its applications of unpowered environmental pressure/temperature sensing," in *Proc. 6th IEEE Int. Conf. Sensors*, Atlanta, GA, pp. 1476–1479, Oct. 28–31, 2007.

CHAPTER 5

IMPLANTABLE PARYLENE-BASED INTRAOCULAR PRESSURE DRAINAGE DEVICES

5.1 Overview

This chapter presents an implantable, unpowered, parylene-based MEMS flow control device for continuous and controllable intraocular fluid drainage and IOP regulation in glaucoma implant therapy as supplementary material to the sensors work in this thesis. The device is designed to be implanted at the subconjunctiva of the eye to provide a biomimetic drainage path similar to the natural path or the ones created by the state-of-the-art glaucoma drainage devices (GDDs). It is in a tube shunt conformation so that a minimally invasive needle-based implantation scheme can be implemented for

reduced time and effort in surgical procedures. Flexible tissue anchors are integrated into the implant to realize suture-less implant anchoring. Successful *in vitro* and *in vivo* characterizations demonstrate the functionality of the tissue anchors, alongside a 6-month animal study verifying the bioefficacy and biostability of such a device implant in the intraocular environment with no surgical or post-operative complications. In addition, parylene microfluidic technology is applied to create micromachined valves with high mechanical and surgical/biological compliance in order to accomplish customized microflow regulation in an exclusive pressure-bandpass profile. The microvalves are designed with appropriate dimensions for integration into a device implant in a form factor suitable for suture-less implantation. Valve prototypes are developed in-channel (i.e., inside representative microchannel conduits) achieving 0–100 mmHg and 0–10 $\mu\text{L}/\text{min}$ pressure and flow rate regulation ranges, suitable for practical IOP drainage. By incorporating these surgical and engineering features described in the following sections, such an implant paradigm has the great potential of fulfilling a continuous, convenient, and direct IOP regulation as a new alternative in glaucoma treatment.

5.2 Surgical Design of Implant: Tissue Anchors

5.2.1 Background

The implantation scheme is considered one of the most crucial factors for the successful implementation of bioimplants, especially when targeting delicate organs such as the human eye. For example, surgical and post-operative complications of all current glaucoma drainage devices (GDDs) leading to device failure and even tissue deterioration have been discussed in the literature [1–3]. The creation of invasive large-area incisions

(e.g., a scleral flap) and the use of sutures may induce such deleterious consequences as well as increase implantation complexity. As a result, a needle-based implantation scheme (as shown in Figure 5-1) is proposed in this work in order to mitigate such problems and further achieve minimally invasive implantation [4]. Conceptually this scheme is utilized for transscleral and transendothelial implants in which integrated flexible tissue anchors are an excellent alternative to sutures for final device fixation. Suture-less implant placement at subconjunctiva can therefore be accomplished.

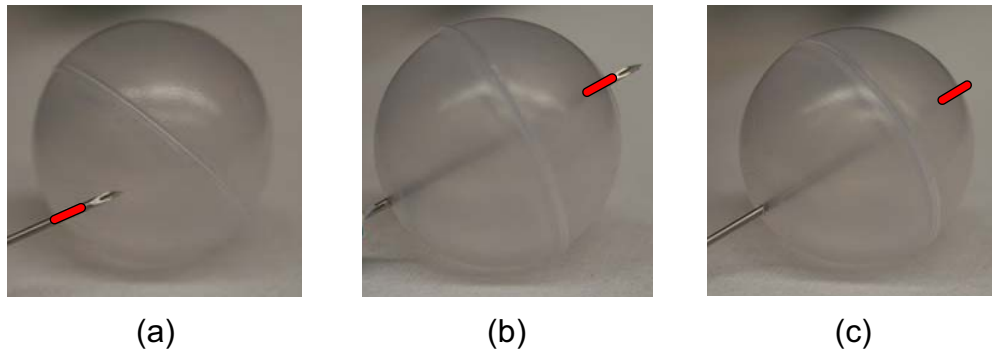


Figure 5-1: Concept of the needle-based device implantation scheme. (a) Device loading inside a hypodermic needle. (b) Needle incision/injection at the target. (c) Device unloading and anchoring after needle retraction. The red region represents the implant location in each step with a hollow ball model used for demonstration purposes.

5.2.2 Design and fabrication

Figure 5-2 illustrates the design of tissue anchoring structures in foldable-arm- and rollable-wing-shaped conformations. The foldable anchors consist of parylene or parylene/silicon arms and parylene flexural joints connected to the implant main body, while the rollable wings are realized using a patterned parylene slab. The designed

flexible anchors can be compliantly folded or rolled so that the implants can be loaded into a hypodermic needle without any damage. After needle incision and device unloading across the target tissue, the anchors spontaneously stretch back to their original conformation, enabling the implant to be fastened to the tissue after needle retraction. Parylene C was selected as the thin-film structural material of the designed tissue anchors to obtain sufficient mechanical flexibility as well as biocompatibility.

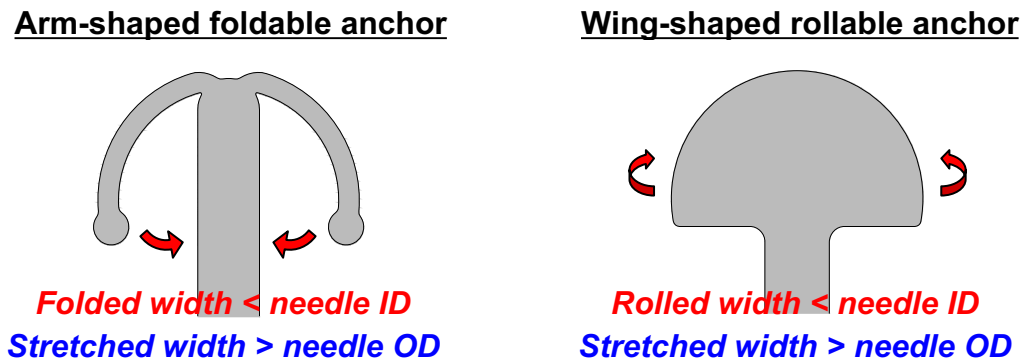


Figure 5-2: Designs of flexible tissue anchor of the implant

The fabrication process of the tube-type implant integrated with tissue anchors (as shown in Figure 5-3) is partly adapted from a modified embedded channel process [5]. Essential process steps include creating high-aspect-ratio parylene-refilled deep trenches facilitated by silicon DRIE to define foldable arms and guard columns for silicon etching, and forming square-like channels with large cross section using isotropic XeF_2 silicon etching and parylene deposition/patterning. Figure 5-4 shows the microfabricated implants embodying approximately 150- μm -wide, 150- μm -high, 4-mm-long artificial microchannel conduits and flexible arm/wing parylene anchors on the ends. The wingspan of the stretched anchors was 800 μm , which is larger than the needle outer diameter and the corresponding incision hole.

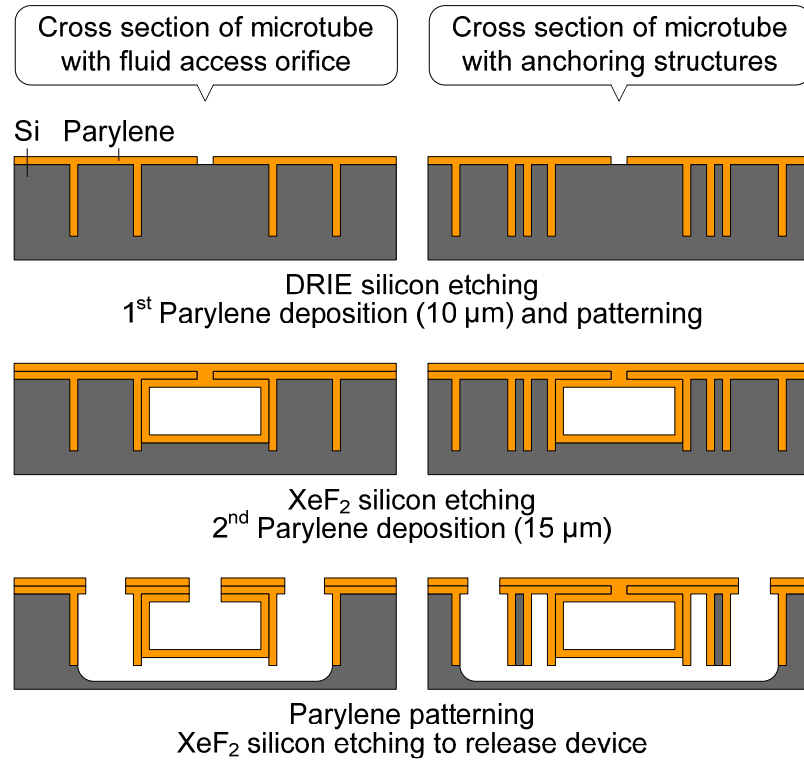


Figure 5-3: Fabrication process flow of tube-type implant prototype with silicon-embedded arms as example of anchoring structures

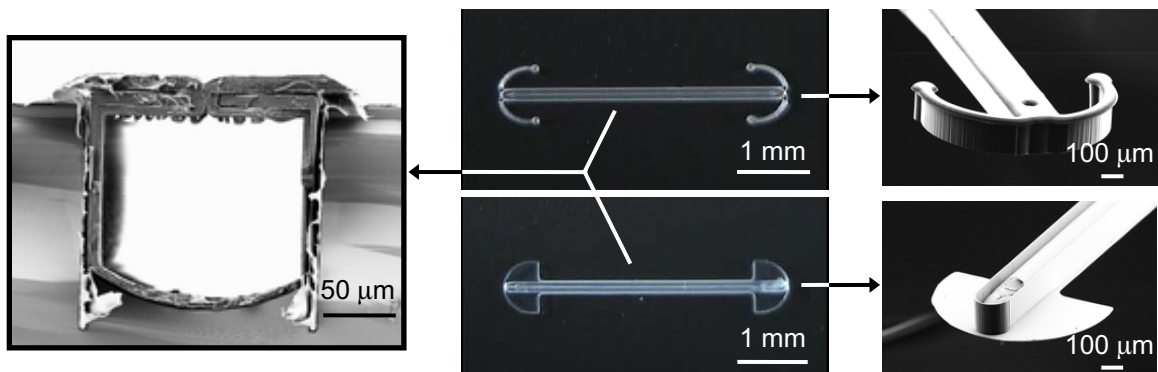


Figure 5-4: Microfabricated parylene-based implants (middle) with SEM images highlighting their artificial conduit before release (left) and flexible tissue anchors after release (right). The foldable arm-shaped anchor is shown top-side up and the rollable wing-shaped anchor is shown bottom-side up.

5.2.3 Characterization results and discussions

The fabricated devices were first tested *in vitro* to verify their functionality. Testing result of pressure/flow rate characterization using water as the testing fluid is shown in Figure 5-5, indicating that the microchannel had a fluidic conductance in the range of 1–10 $\mu\text{L}/\text{min-mmHg}$, comparable to the contemporary GDDs [6]. Afterwards, anchor testing was conducted with the use of a customized implanter and a 22-gauge clinical-standard hypodermic needle. As shown previously in Figure 5-1, the “inside-out” implantation scheme was utilized to implant the devices through an incision created at the other side from the target site of the eye. *In vitro* study (as shown in Figure 5-6) demonstrates that all devices were successfully fastened in their predetermined positions across the simulated eye model after needle injection, with the arm anchors providing better visualization due to the embedded silicon while the wing anchors were structurally more robust. *In vivo* animal study using three live rabbit eyes as the model was also performed to evaluate the bioefficacy of the flexible tissue anchors in wing-shaped design as example. Remarkably, the implantation surgery as shown in Figure 5-7 was able to be completed within 5 min due to its suture-less minimally invasive nature, implying minimal surgical complications could be induced. Observation shows that the wing structure was stretched back after unloading from the needle, as expected. Long-term follow-up study with result photographs (as shown in Figure 5-8) confirms that no device dislocation or post-operative complications—including inflammatory response or tissue encapsulation/fibrosis—were found throughout the 6-month study. These results substantially verified the surgical/biological feasibility of using such an implant paradigm in the intraocular environment.

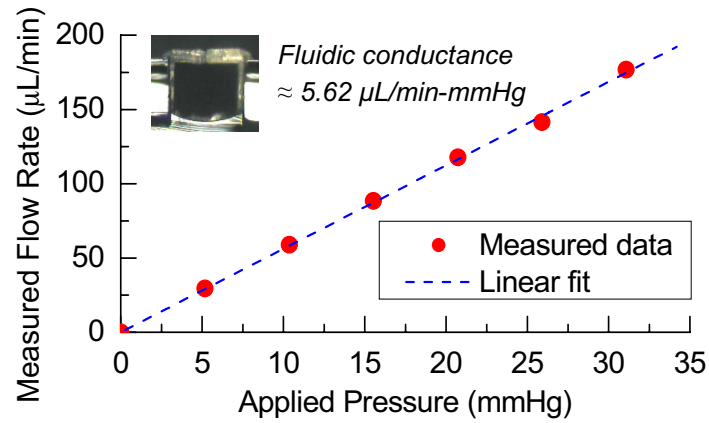


Figure 5-5: Pressure/flow rate testing result of the microchannel conduit

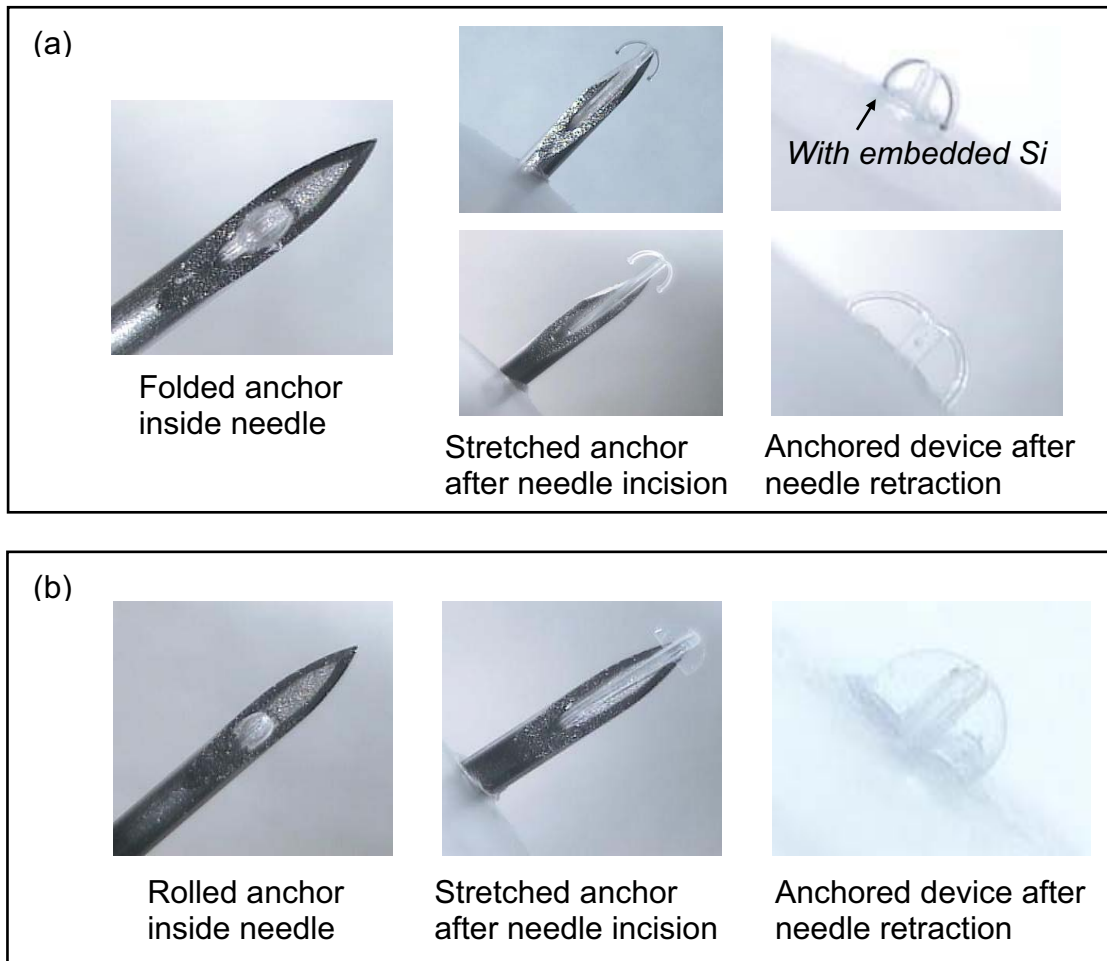


Figure 5-6: *In vitro* tissue anchor testing. (a) Foldable arm-shaped anchor. (b) Rollable wing-shaped anchor

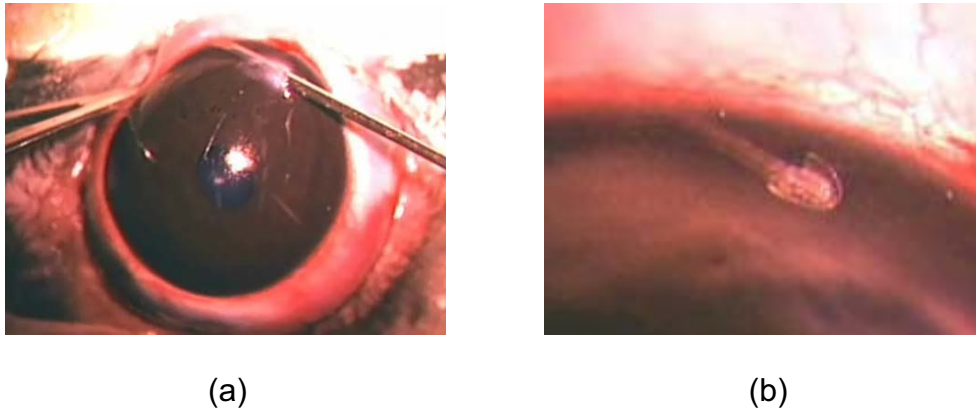


Figure 5-7: Needle-based implantation surgery of the device. (a) 22-gauge needle incision to inject the implant into the live eye model. (b) Suture-less anchored implant in the intraocular environment after surgery

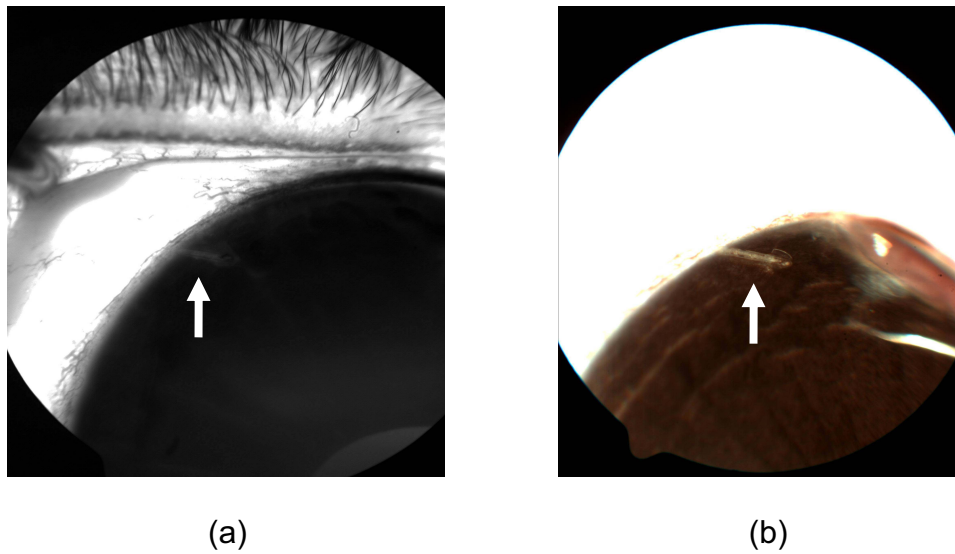


Figure 5-8: *In vivo* animal study of the flexible tissue anchor. (a) Fluorescein angiogram showing no noticeable blood vessel leakage at the implantation site 3 days after surgery. (b) Fundus photograph showing no device dislocation or post-operative complications 6 months after surgery. The arrows indicate the implant as seen through the cornea.

5.3 Engineering Design of Implant: Microvalves

5.3.1 Background

In addition to the aforementioned surgical features, the implant has to incorporate microflow control components inside the microchannel conduit for controllable flow regulation. Here the microfluidic approach is implemented to fulfill the concept by exploiting microvalves as the key control component. They enable systematic flow control for accurate and reliable operation, as well as high-level integration with other microfluidic components stemming from the fact that their mechanical structures are relatively simple [7]. Technically, microvalves are either active or passive, with passive valves (i.e., check valves) having the advantages of simple operation, zero power consumption, and ease of integration. Because check valves can shunt fluids with a single pressurized flow direction they are recognized as “fluidic diodes.” Figure 5-9 shows the shunting behaviors of a check valve [8] and an electronic diode for comparison. Based on their actuation mechanism, micromachined check valves are categorized as normally-open valves where the fluidic channel is always open unless there is sufficient backward pressure [8], or normally-closed valves where the fluidic channel is blocked until the pressure is above cracking/threshold pressure [8, 9]. However, as indicated in Figure 5-9, neither type of check valve is ideal. For normally-open (NO) valves, the cracking pressure to conduct forward flow is minimal, while there is always a leakage problem when backflow is applied. For normally-closed (NC) valves, the backflow leakage can be reduced, but the cracking pressure turns out to be so large that a reasonable flow rate is not achievable with low pressure loading. Given this fundamental knowledge, new microvalves can be developed as part of the proposed MEMS-based

implant paradigm achieving the required engineering and biological/medical specifications as stated in Chapter 2.

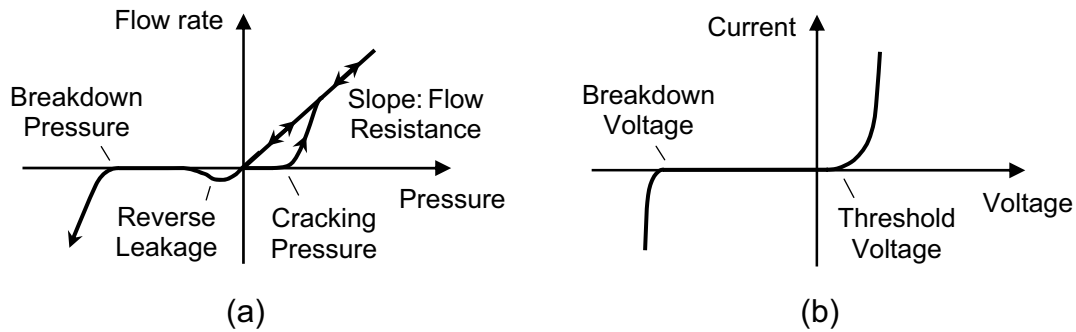


Figure 5-9: Fluidic and electronic diodes. (a) Pressure/flow rate curve of a mechanical check valve. (b) I-V curve of an electronic diode for comparison

5.3.2 Design and fabrication

Although conventional micro check valves are not ideal in certain applications, different design combinations and variations can be implemented to modify the fluidic behaviors from those in a single valve. Under this concept, microfluidic devices in a dual-valve configuration and a single-valve configuration have been separately developed in this work to achieve passive microflow regulation for the proposed operation. With their design concept illustrated in Figures 5-10 and 5-11, both of the configurations can inherently regulate pressure and flow rate of fluids without any power consumption and greatly reduce the complexity of device fabrication and integration compared with other existing micro flow regulators. A multi-layer parylene surface-micromachining technology with process flows illustrated in Figures 5-12 and 5-13 is utilized to fabricate the microfluidic devices (as shown in Figures 5-14 and 5-15) being tested in this work. Several important device dimensions are listed in Table 5-1; these are designed to realize

flow controls in a minute pressure/flow rate range as well as to achieve suitable form factor for needle-based minimally invasive implantation. This specific flow regulation in a pressure-bandpass profile meets the operation specifications of continuous IOP regulation. Details on device design and fabrication can be found in [10] and [11].

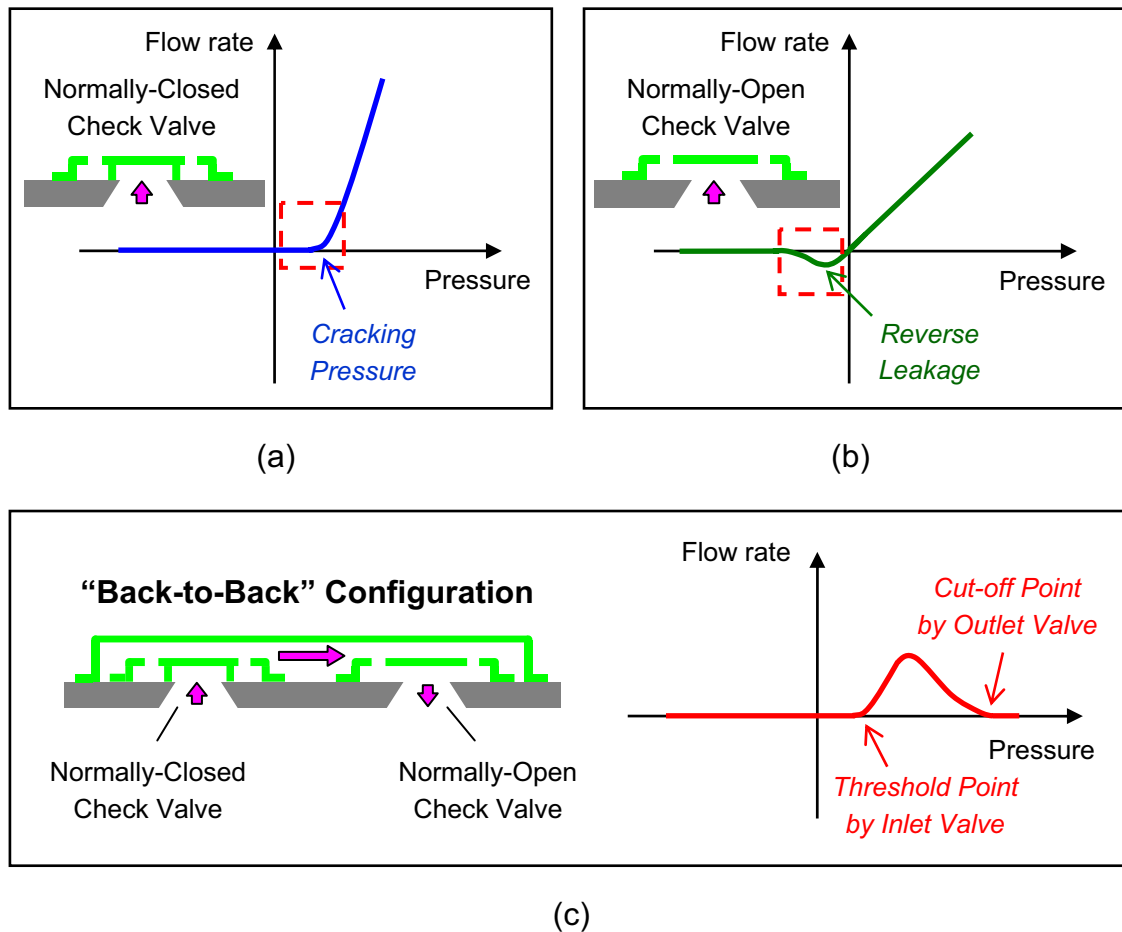
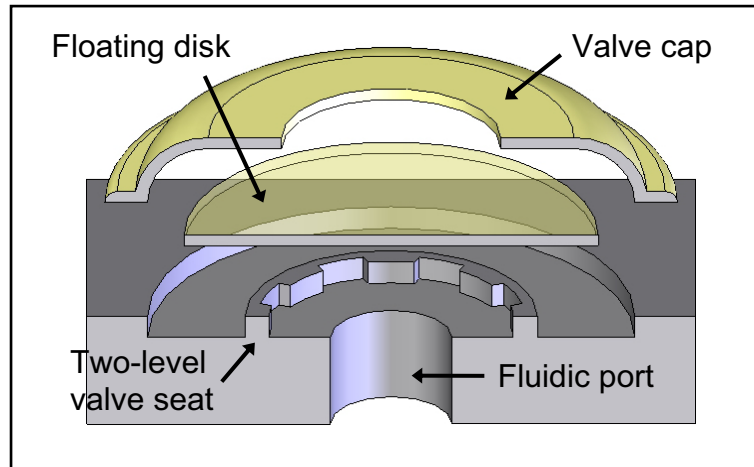
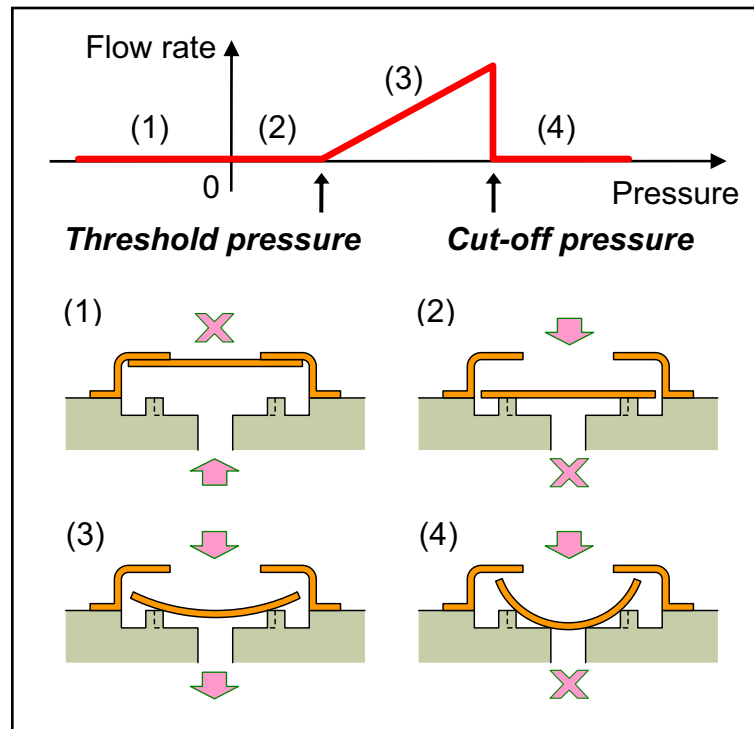


Figure 5-10: Concept of dual-valve configuration featuring combination of tethered-disk microvalves in normally-closed and normally-open check valve designs. (a) Fluidic behavior of normally-closed valve. (b) Fluidic behavior of normally-open valve. (c) Generated fluidic behavior by the dual valves in back-to-back operation. The arrows in valve illustrations indicate the forward flow direction.



(a)



(b)

Figure 5-11: Concept of single-valve configuration featuring floating-disk microvalve in pressure-bandpass check valve design. (a) Conceptual schematic (cross-sectional exploded view; not to scale). (b) Self-regulation mechanism. The arrows indicate flow directions through the valve. Note the relative position between disk diaphragm and radiating trench channels of two-level valve seat corresponding to device operation steps.

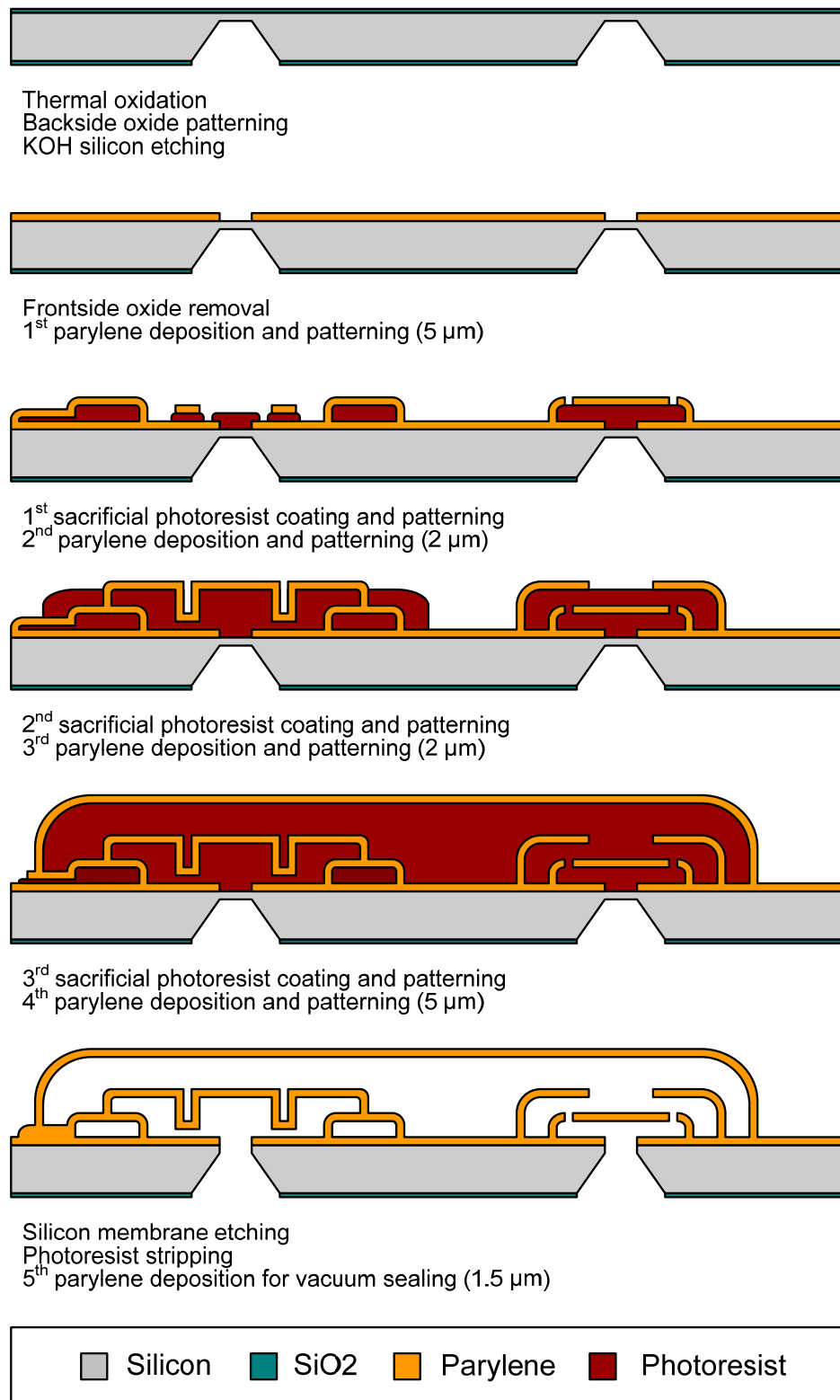


Figure 5-12: Fabrication process flow of dual parylene-based microvalves

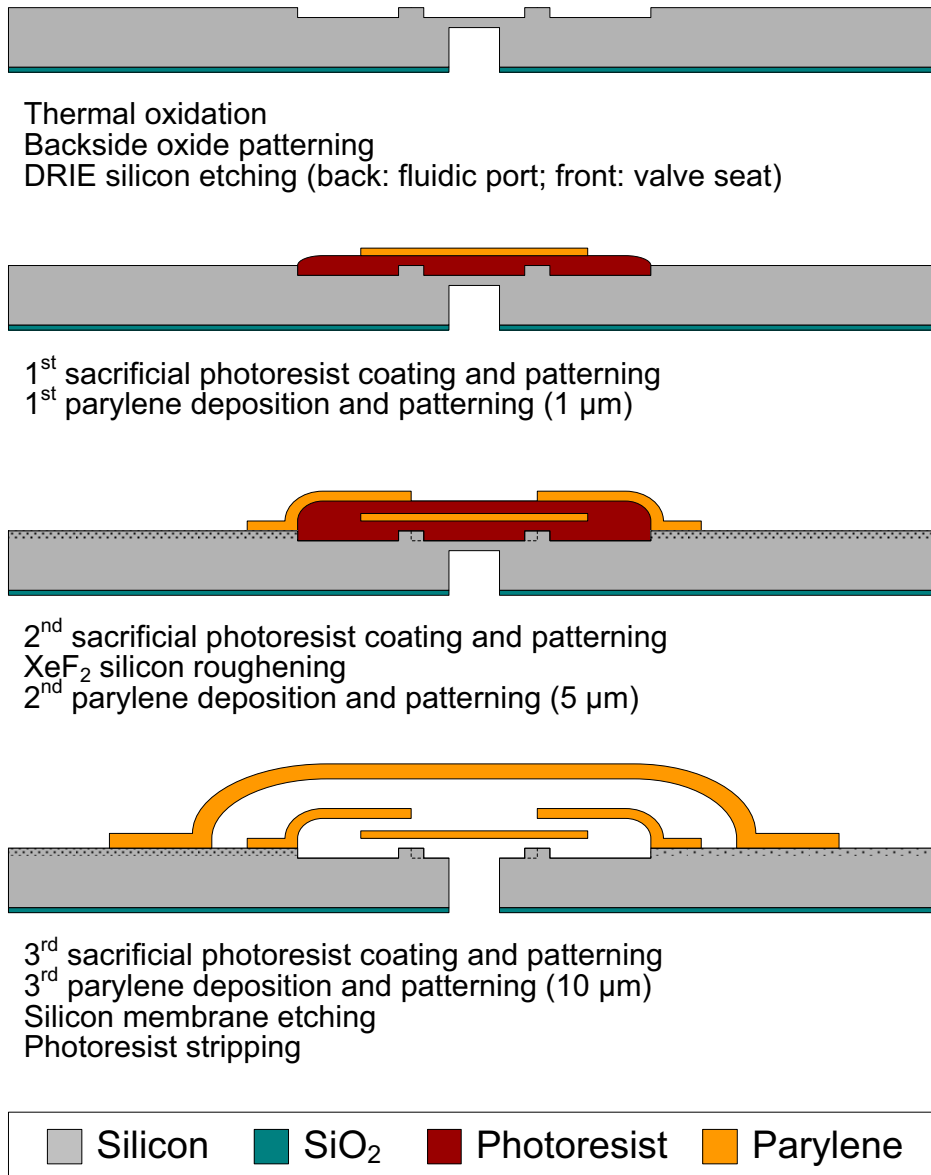


Figure 5-13: Fabrication process flow of single parylene-based microvalve

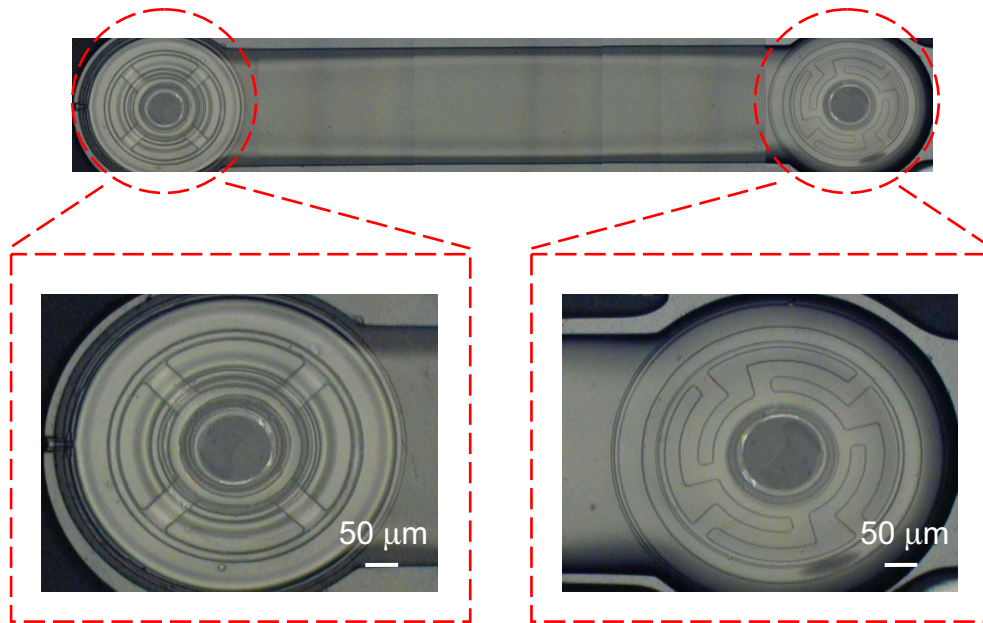


Figure 5-14: Micrographs of the fabricated dual-valved channel (2 mm long in port-to-port distance) and cut-in views of the normally-closed (left) and normally-open (right) parylene check valves, all in top view. The diaphragm tethers can be designed as straight arms or twisted arms depending on performance requirements.

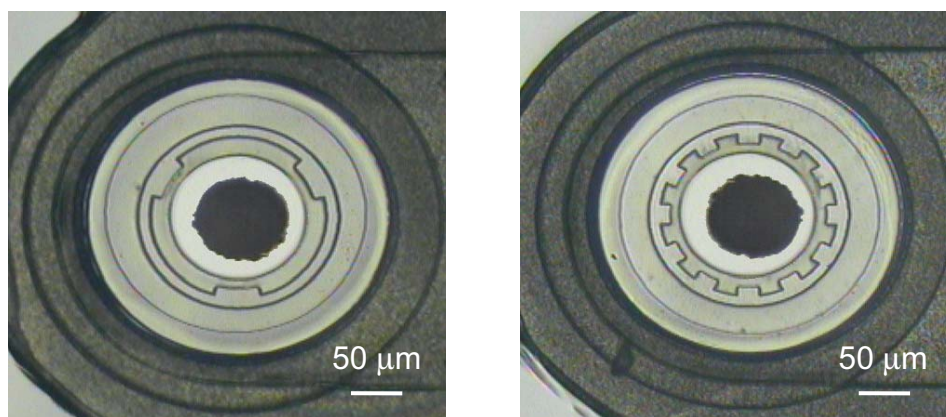


Figure 5-15: Micrographs of the fabricated floating-disk parylene single valves with different design variations immersed in water (top view)

Table 5-1: Design metrics of the in-channel microvalves developed in this work

	Dual-valve configuration	Single-valve configuration
Valve disk diameter	200 μm	250 μm
Valve disk thickness	1.5 μm	1 μm
Valve seat orifice diameter	100 μm	100 μm
Total valve width	460 μm	400 μm
Channel width	400 μm^*	350 μm^*
Channel height	20 μm	20 μm
Channel length	2,000 μm	1,800 μm
Channel thickness	10 μm	10 μm

*500 μm at the valved sections

5.3.3 Characterization results and discussions

Microfabricated in-channel parylene microvalves were tested using the fluidic setup illustrated in Figure 5-16. A customized testing jig featuring PEEK (poly-ether-ether-ketone) material was used to provide a macroscale/microscale fluidic interface with diced chips, so that microflows could be introduced with regular Teflon capillary tubing to the devices through their backside fluidic access ports [12, 13]. The jig was immersed in water when packaging the floating-disk valves in order to avoid stiction occurrence at an air-liquid-solid interface on the microvalves. Air bubbles in the entire fluidic path need to be completely removed prior to valve characterization to ensure reliable microvalve operation. For demonstration purposes, clean water served as the fluid source for device characterization. On the front end of the jig, an off-chip pressure regulator and a pressure gauge were connected to control the injection pressure of the fluids with 0.07

kPa (~ 0.01 psi, ~ 0.5 mmHg) tuning resolution. Pressure readouts were recorded in gauge pressure format to indicate the additional pressure loading from the injected fluids relative to atmospheric pressure. Hydrostatic pressure differences due to any height difference of the column in the testing system were carefully calibrated for accurate pressure control. Flow rate measurement and fluid collection was performed on the back end of the jig. Water flow rate was measured by recording its marching velocity in the capillary enabled by its relatively small flow rates ($\mu\text{L}/\text{min}$ range). In marching velocity recording, given the fact that the resolution was limited to 0.5 mm in marching distance and 1 s in marching time in the testing setup, the overall flow rate measurement error was typically 5%–15%, depending on the flow rate level. Using these measurement techniques with the stated considerations, pressure/flow rate behavior of the in-channel microvalves could be well characterized.

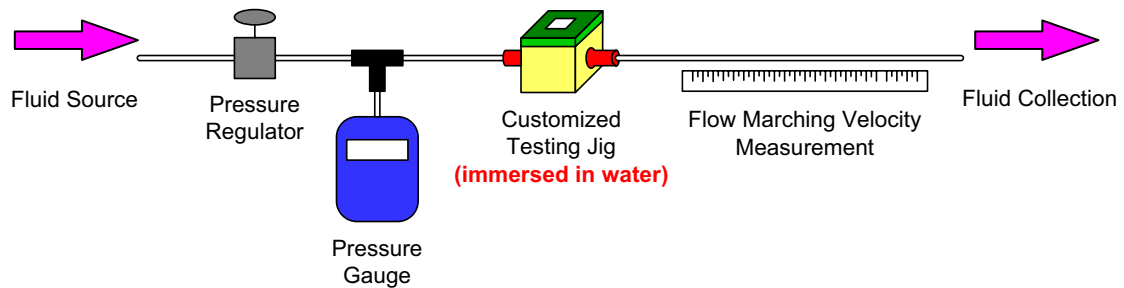


Figure 5-16: Schematic of fluidic testing setup for device characterization. The jig was immersed in water if packaging single floating-disk valves to avoid stiction effect.

Representative pressure/flow rate testing results of the micromachined in-channel valves in both dual-valved and single-valved configurations were shown in Figures 5-17 and 5-18, with reliable and repeatable behaviors from the same device in cyclic operation

regardless of errors in gauge pressure and marching velocity/flow rate measurements. They successfully demonstrated passively controlled microflow in 0–100 mmHg and 0–10 $\mu\text{L}/\text{min}$ bandpass regulation ranges under the fabricated device dimensions. Both low-off and high-off flow shunting characteristics were achieved in experiments given the result of no observable water flow below the threshold pressure point and greatly reduced flow rate beyond the cut-off pressure point. The threshold and cut-off pressures were characterized to be approximately 10 mmHg and 50 mmHg in the dual-valved device and 10–20 mmHg and 65–75 mmHg in the single-valved device. Higher variations of the pressure characteristics in the single floating-disk microvalve were caused by imperfect valve disk-seat-cap alignment due to: 1) uncontrollable in-plane disk movement during operation; and 2) double-side pattern misalignment on the wafer. These two misalignments can change the boundary conditions of the bendable disk including the effective overhang and the pressurized area of the disk diaphragm. All these factors can accordingly vary the device performance as the experimental results had approximately 30%–50% discrepancy from the designed threshold and cut-off pressures, so that further study and analysis will need to be conducted to address this issue. Moreover, the following three factors related to the fabrication process contributed to the resultant performance variation in both valved configurations: 1) thickness control of photoresist coating; 2) thickness control of parylene deposition; and 3) material property control of thin-film parylene. Consequently, more process calibration and characterization should be conducted in order to enhance uniformity of the device performance so that the bandpass pressure regulation range can be precisely controlled depending on specific applications. The maximum water flow rate of the devices in dual-

valved configuration was lower than that in single-valved configuration ($1.3 \mu\text{L}/\text{min}$ and $7.9 \mu\text{L}/\text{min}$, respectively) because of the difference in fluidic resistance. Nevertheless, the overall fluidic resistance could be modified by having different dimensions of the microvalve and/or the encapsulating microchannel, so as to appropriately meet the design specification of practical IOP drainage. Under backward flow injection, the devices in both configurations were able to withstand high pressure as they remained leakage-proof when operated under pressure loadings greater than 1,000 mmHg. These characterization results demonstrated that such valved microfluidic devices achieved pressure-bandpass flow control suitable for physical intraocular fluid drainage and IOP regulation. More device testing results of the individual valves (i.e., normally-closed tethered-disk valve, normally-open tethered-disk valve, and floating-disk valve) developed in this work are listed in Table 5-2, with details in [10] and [11] for basic reference of valve implementation in practical implant systems.

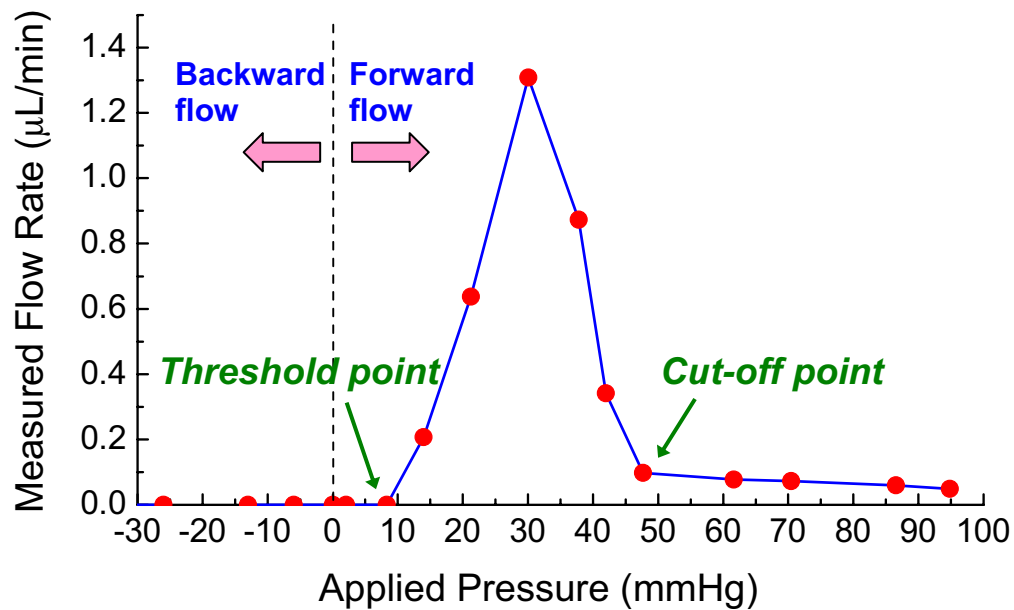


Figure 5-17: Dual valve characterization result to water microflow control

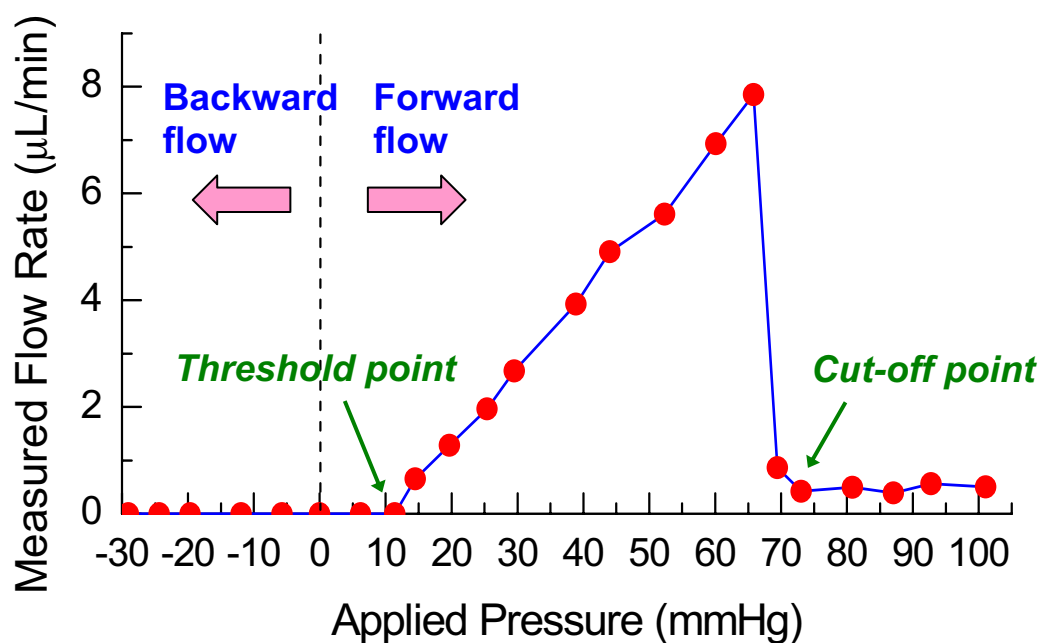


Figure 5-18: Single valve characterization result to water microflow control

Table 5-2: Comparison of the developed parylene-based microvalves
in regular check valve operation for flow shunting

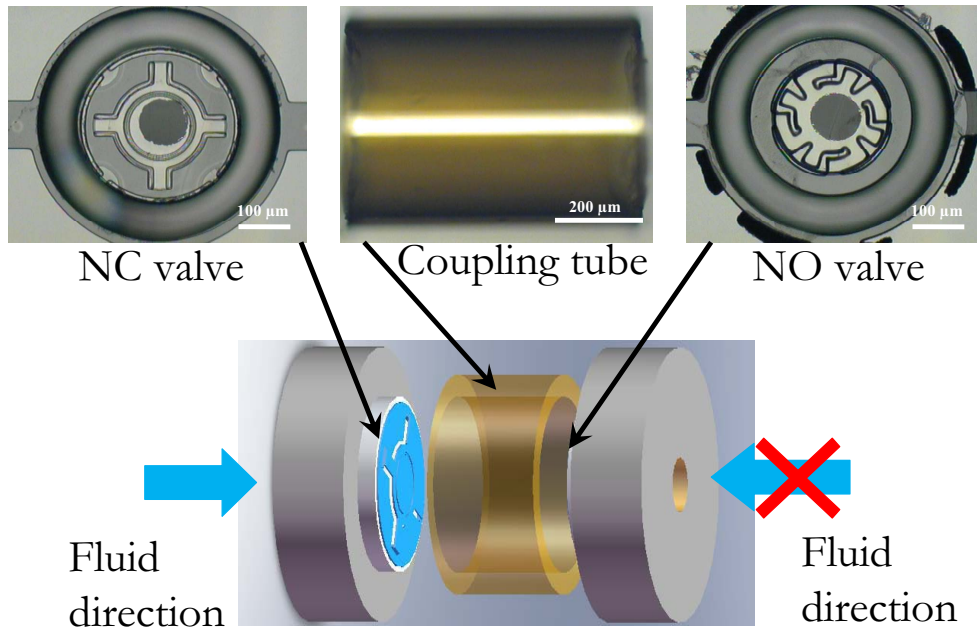
	Normally-closed valve	Normally-open valve	Floating-disk valve
Valve disk design	Tethered disk	Tethered disk	Floating disk
Occupied area*	10^{-7} m^2	10^{-7} m^2	10^{-7} m^2
Valve void volume	$\sim 3 \text{ nL}$	$\sim 1 \text{ nL}$	$\sim 1 \text{ nL}$
Cracking pressure	$\sim 10 \text{ mmHg}$	$< 5 \text{ mmHg}$	~ 0
Reverse-leakage stop pressure	~ 0	$> 50 \text{ mmHg}$	~ 0
Breakdown pressure	$> 1,000 \text{ mmHg}$	$> 1,000 \text{ mmHg}$	$> 1,000 \text{ mmHg}$

*Calculated order of scale

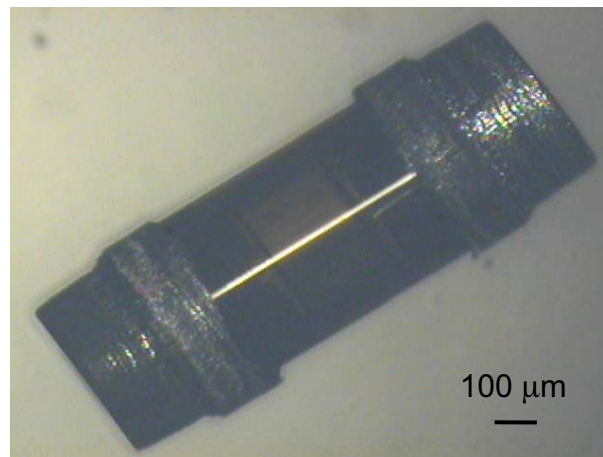
Two different microvalved design configurations (dual-valved and single-valved) for flow controls have been reported as adequate candidates to be included in the IOP drainage device implant, but each of them has its own advantages and disadvantages. These considerations in their use of pressure-bandpass flow controls are compared in Table 5-3. With these engineering findings, current work is underway to incorporate such parylene-based microvalves in tube shunt implants for *in vivo* studies of controllable continuous intraocular fluid drainage and associated IOP regulation in practice. For example, a proof-of-concept experiment has been conducted featuring a dual-valve-packaged implant shown in Figure 5-19 as the initiative [14]. These studies experimentally verify the feasibility and possibility of integrating all of the surgical and engineering device features in the ultimate MEMS-based implant in the future.

Table 5-3: Comparison of the developed parylene-based microvalves
with implementation considerations

	Dual-valved configuration	Single-valved configuration
Valve disk design	Tethered disk	Floating disk
Number of valves required to accomplish the flow control profile	2	1
Design constraints	high	low
Fabrication complexity	high	moderate
Handling after fabrication	easy	difficult
Device reliability	moderate	high
Pressure characteristics variation	low	high
Surgical/biological compliance	high	high



(a)



(b)

Figure 5-19: Concept of representative dual-valved tube shunt implant integration for *in vivo* study [14]. (a) Post-fabrication assembly illustration. (b) Stereoscope image of assembled tube shunt device prototype. Images courtesy of Mr. Jeffrey C. Lin.

5.4 Summary

An implantable unpowered micromechanical parylene-based microfluidic device has been proposed in this chapter as part of a new implant paradigm to realize continuous and controllable physical IOP drainage. Surgical and engineering features are separately presented with complete design, fabrication, and characterization description in order to demonstrate the concept of such an implant. On the surgical side, the implant is designed to be a tube shunt type, with integrated flexible tissue anchors facilitating a minimally invasive suture-less needle-based device implantation scheme at the subconjunctiva of the eye, in order to provide a biomimetic intraocular fluid drainage path. Long-term *in vivo* animal study has verified the feasibility of the biocompatible implant prototype placed in the intraocular environment. On the engineering side, two device prototypes, in dual-valved and single-valved design configurations, have been developed to accomplish the flow control function of the implant, with the demonstrated performance suitable for physical intraocular fluid drainage and IOP regulation. These experimental studies preliminarily verify feasibility of such device features for use in the ultimate MEMS-based implant. With future development on the integration of these features, such a device implant can be realized as a prospective means to fulfilling continuous, convenient, and direct IOP regulation for practical glaucoma treatment.

5.5 Bibliography

- [1] C.-H. Hong, A. Arosemena, D. Zurakowski, and R. S. Ayyala, "Glaucoma drainage devices: A systematic literature review and current controversies," *Surv. Ophthalmol.*, vol. 50, pp. 48–60, 2005.
- [2] R. S. Ayyala, J. L. Duarte, and N. Sahiner, "Glaucoma drainage devices: State of the art," *Expert Rev. Med. Dev.*, vol. 3, pp. 509–521, 2006.
- [3] K. S. Schwartz, R. K. Lee, and S. J. Gedde, "Glaucoma drainage implants: A critical comparison of types," *Curr. Opin. Ophthalmol.*, vol. 17, pp. 181–189, 2006.
- [4] P.-J. Chen, D. C. Rodger, S. Saati, J. C. Altamirano, C.-H. Lin, R. Agrawal, R. Varma, M. S. Humayun, and Y.-C. Tai, "Implementation of microfabricated suture-less flexible parylene tissue anchors on minimally invasive biomedical implants," in *Proc. 11th Int. MicroTAS Conf.*, Paris, France, pp. 518–520, Oct. 7–11, 2007.
- [5] C.-Y. Shih, W. Li, and Y.-C. Tai, "A novel embedded liquid chromatography system with submicron-sized filter structure and capacitively-coupled contactless conductivity detector," presented at The 20th International Symposium on Microscale Bioseparations, Amsterdam, Netherlands, Jan. 22–26, 2006.
- [6] D. L. Eisenberg, E. Y. Koo, G. Hafner, and J. S. Schuman, "In vitro flow properties of glaucoma implant devices," *Ophthalmic Surg. Las.*, vol. 30, pp. 662–667, 1999.
- [7] K. W. Oh and C. H. Ahn, "A review of microvalves," *J. Micromech. Microeng.*, vol. 16, pp. R13–R39, 2006.

- [8] X. Q. Wang, "Integrated parylene micro electro mechanical systems (MEMS)," Ph.D. dissertation, Dept. Electr. Eng., Calif. Inst. Technol., Pasadena, CA, 2000.
- [9] J. Xie, X. Yang, X. Q. Wang, and Y.-C. Tai, "Surface micromachined leakage proof parylene check valve," in *Proc. 14th IEEE Int. Conf. MEMS*, Interlaken, Switzerland, pp. 539–542, Jan. 21–25, 2001.
- [10] P.-J. Chen, D. C. Rodger, E. Meng, M. S. Humayun, and Y.-C. Tai, "Surface-micromachined parylene dual valves for on-chip unpowered microflow regulation," *J. Microelectromech. Syst.*, vol. 16, pp. 223–231, 2007.
- [11] P.-J. Chen, D. C. Rodger, M. S. Humayun, and Y.-C. Tai, "Floating-disk parylene microvalves for self-pressure-regulating flow controls," *J. Microelectromech. Syst.*, in press.
- [12] Q. He, "Integrated nano liquid chromatography system on-a-chip," Ph.D. dissertation, Dept. Elect. Eng., Calif. Inst. Technol., Pasadena, CA, 2005.
- [13] V. C. Shih, "Temperature-controlled microchip liquid chromatography system," Ph.D. dissertation, Dept. Electr. Eng., Calif. Inst. Technol., Pasadena, CA, 2006.
- [14] J. C. Lin, P.-J. Chen, S. Saati, R. Varma, M. Humayan, and Y.-C. Tai, "Implantable microvalve-packaged glaucoma drainage tube," in *Proc. 13th Solid-State Sensors, Actuators, and Microsystems Workshop*, Hilton Head Island, SC, pp. 146–149, Jun. 1–5, 2008.

CHAPTER 6

CONCLUSIONS

Over the years, researchers and engineers have proved MEMS to be an enabling technology for numerous applications covering physical, chemical, and biological domains in defense and commercial markets. The access of MEMS to interaction with the microscopic world through those tiny little micromechanical structures facilitates smaller, cheaper, and faster solutions to target sensing, actuating, and control compared with conventional mechanical/electrical components. Integration of such microdevices, possibly with microelectronics, realizes high-level system applications. After successful demonstration of physical MEMS, optical MEMS, and RF MEMS—given their stable growth in industry nowadays—the next territory to be expanded on the microtechnology portfolio is microfluidics, bioMEMS, and medical MEMS for life science and health care, driven by the increasing need for better quality of life.

Backed by profound study of parylene as a biocompatible MEMS material in our research group, this thesis investigates the possibility of this parylene MEMS technology in development of implantable medical microdevices. As a continuation with the reported applications in cortex neural probes, spinal cord electrode arrays, and retinal prosthesis, two kinds of intraocular MEMS implants involving pressure sensors and valved flow-control devices have been developed in this work for medical application in glaucoma study and management. Clinical findings of the correlation between neuropathy and a physiological parameter (i.e., intraocular pressure (IOP)) in glaucoma provide a basis for the proposed approaches that utilize MEMS implants to physically monitor and regulate the IOP in glaucoma patients. With a great emphasis on pressure sensors, followed by supplemental description of pressure regulation devices, the complete design, fabrication, characterization, and analysis of such microdevices have been presented in this thesis, thus demonstrating their feasibility and potential for meeting the engineering and surgical/biological specifications of the proposed applications. More importantly, studies with the use of these MEMS implants have demonstrated applicable minimally invasive implantation schemes, as well as device chronic biocompatibility in the intraocular environment (given the evidence of no/minimal observed surgical or post-operative complications). These parylene-based MEMS implant paradigms have performed significant and promising results not achieved by previous MEMS or non-MEMS devices/implants due to technology barriers either in manufacturing or material aspect.

Certainly there were lots of trials and iterations conducted before successful demonstration of the devices presented throughout this thesis. This fact may be more

obvious as compared with other types of MEMS devices because more concerns and unknowns exist in such interdisciplinary fields as that of emerging engineering and biology/physiology/medicine. Through this work, we understand that device biocompatibility is extremely important for *in vivo* applications, and thus any planning of design, fabrication, and packaging of the device should be thoroughly examined to address possible surgical and biological issues from the beginning of process, in order to effectively reduce associated time and effort in the entire development cycle. In addition, this work mainly focuses on device development, while more studies on device-to-world interfacing will be required from the system-level view for ultimate use in practice, especially in the implementation of the external reader in the IOP sensor example. We can foresee that most cost and challenges would fall upon the reader part in the overall monitoring system, as has already been shown in other developed wireless sensing/detection paradigms, such as radio-frequency identification (RFID).

Initiated with ophthalmic applications as the first demonstration, the developed biocompatible parylene-based MEMS implants are completely adaptable to other biomedical applications as long as the corresponding physiological parameters can be monitored/regulated by the physical operating principles in the device nature. Representative examples include, but are not limited to, cardiovascular pressure monitoring, intracranial pressure monitoring, cerebrospinal fluid (CSF) drainage, blood flow regulation, hypertension control, and other detections and controls involved during neurosurgeries. It can be anticipated that such parylene MEMS technology will evolve into more interesting and useful device derivatives in the future.

APPENDIX

INTRODUCTION TO MEMS TECHNOLOGY

A.1 MEMS

A.1.1 Origin and definition

There is no doubt that our science voyage to “Lilliput”—the microscopic world—was initiated by two remarkable talks: “There’s Plenty of Room at Bottom [1],” and “Infinitesimal Machinery [2],” delivered by the contemporarily prestigious physicist Richard P. Feynman. Even though he himself could not see the real use of these micromachines at that time of his presentations, he successfully anticipated the future research trend toward exploring a brand new field: microtechnology or nanotechnology. As shown in Figure A-1 [3], those microdevices (including “micromachinery” as Feynman called them) have characteristic lengths in the range of 1–100 μm , smaller than

the diameter of human hair and comparable to that of bacteria and human cells. Because of this, numerous promising applications can be derived that benefit by their size and associated scaling laws [4].

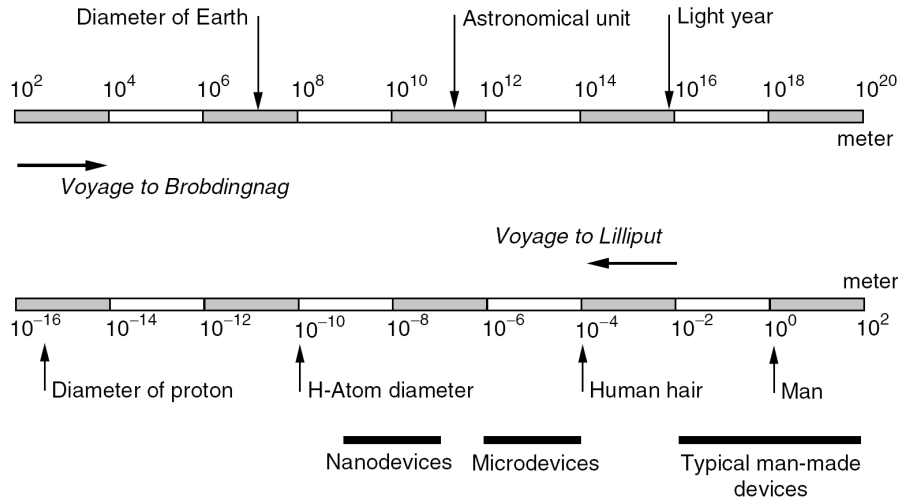


Figure A-1: Scale of things. $1 \text{ m} = 10^6 \mu\text{m} = 10^9 \text{ nm} = 10^{10} \text{ \AA}$. Image reprinted from [3].

With almost 50 years of research and development by scientists and engineers, microtechnology has become a practical and viable solution to many scientific and engineering problems/challenges nowadays [4–9]. It enables us to explore new phenomena at the microscale for extensive applications. The associated implementation platforms are usually recognized as micro-electro-mechanical systems (MEMS) or microsystems, which embody micromechanical structures and microelectronics as core components to accomplish sensing, actuating, and computing functions (as shown in Figure A-2). Micromechanical structures are intensively emphasized in MEMS as they are the key to realization of the transducing/interfacing concept. They crucially create the communication interface between the macroworld (“Brobdingnag,” i.e., humans/users) and the microworld (“Lilliput,” i.e., targets at the microscale) in interdisciplinary

operations covering physical, chemical, electrical, mechanical, optical, and biological domains. MEMS can also provide smaller, faster, cheaper, and more effective solutions as compared with conventional bench-top approaches in many circumstances, all because of the nature of miniaturization.

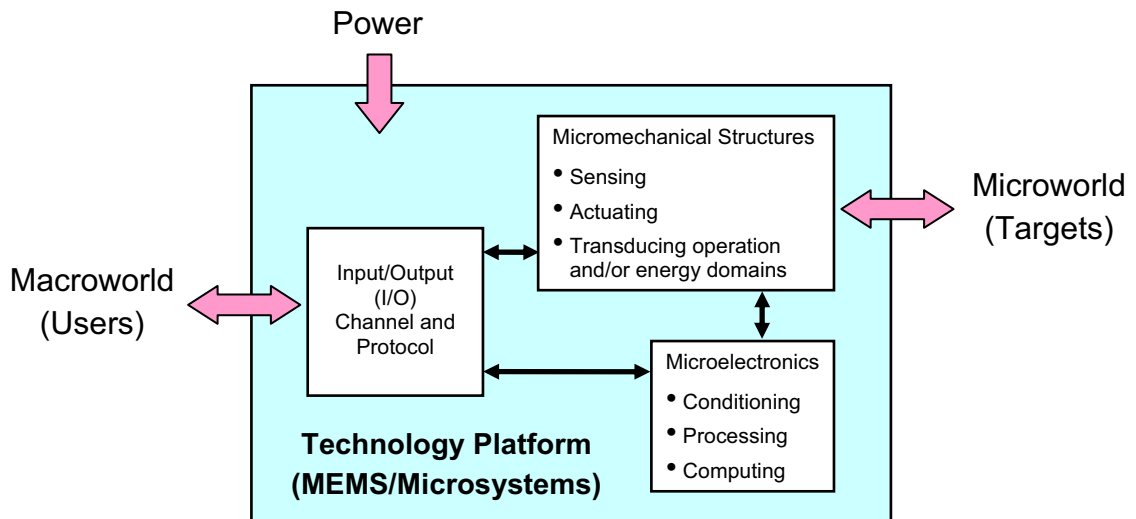


Figure A-2: MEMS implementation concept with micromechanical structures as the key to realization of macro-to-micro communication and interfacing. Image adapted from [4].

A.1.2 Technology

MEMS are highly correlated with semiconductor integrated circuits (IC) because their microfabrication processes are identically based on silicon processing technology. Accordingly, their fabrication facilities are ideally interchangeable based on batch-fabrication [10] and pattern transfer [9, 11] concepts as shown in Figures A-3 and A-4, respectively. Instead of creating electronic components and circuitry, MEMS technology mainly focuses on development of micromechanical structures and devices dealing more with mechanical, thermal, and other properties. Because of their similarities on the fabrication side, the rapid growth of the IC industry, with revolutionary progresses in

microelectronics [12] (as shown in Figure A-5) has resulted in the growth of the MEMS industry as well, with several representative examples [13–15] (as shown in Figure A-6) indicating the enhancement of both design and fabrication complexity by the recent technology push. As more evidence of continuous MEMS technology development, the recent growth in MEMS integration given in Figure A-7 shows a trend similar to the well-known “Moore’s law” [16] in terms of device density.

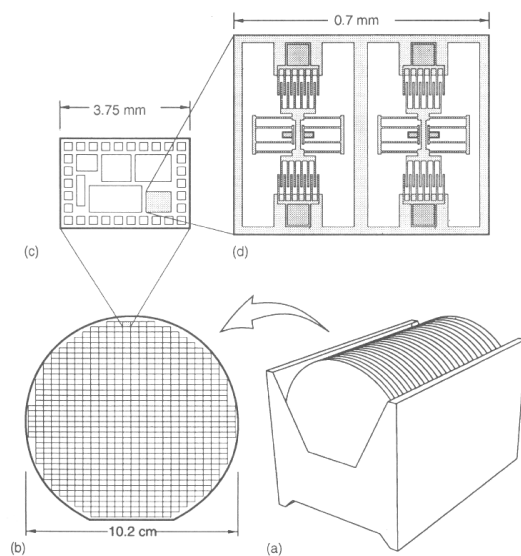


Figure A-3: Concept of batch-fabrication process in silicon processing technology. Close-ups are shown in the sequence of (a)–(d). Image reprinted from [10].

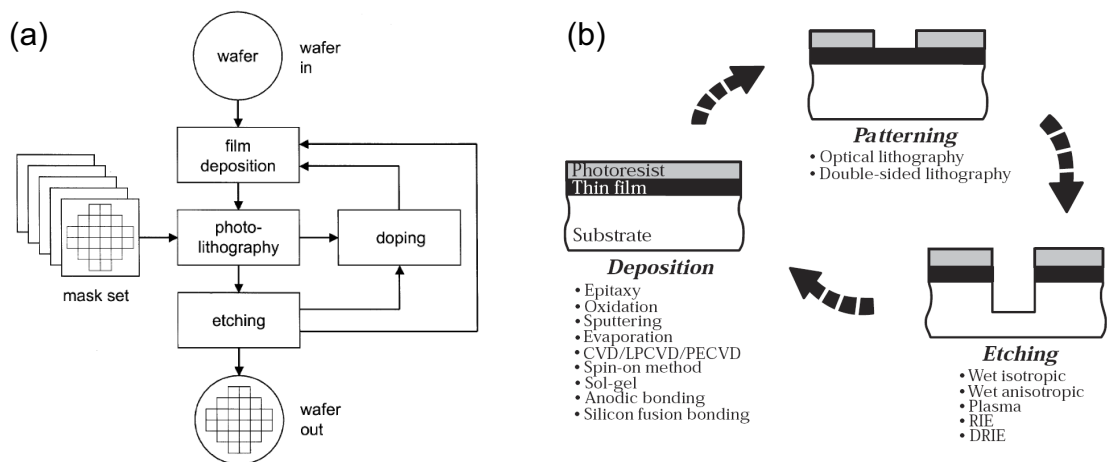


Figure A-4: Concept of pattern-transfer process in silicon processing technology. (a) Process flow. (b) Involved process steps. Images reprinted from [9] and [11].

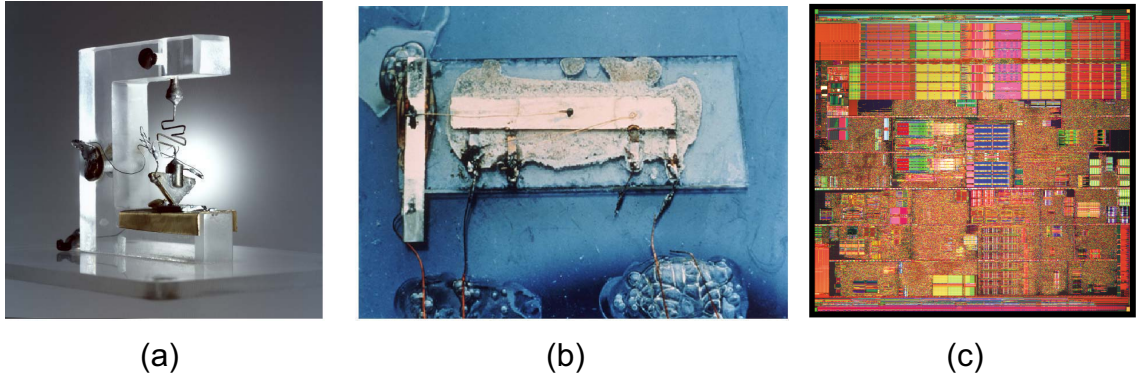


Figure A-5: Microelectronics development. (a) The first transistor from Bell Labs (Murray Hill, NJ) in 1947. (b) The first IC from Texas Instruments (Dallas, TX) in 1958. (c) Pentium[®] 4 chip from Intel (Santa Clara, CA). Images adapted from [12].

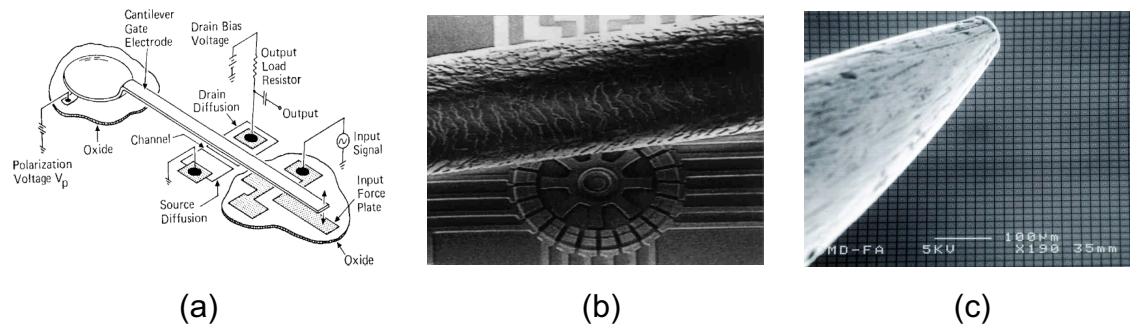


Figure A-6: MEMS development. (a) The first resonant gate transistor [13] from Westinghouse (Monroeville, PA) in 1967. (b) The first micromotor [14, 15] (next to a human hair) from the University of California at Berkeley in 1989. (c) DLP[®] chip (next to a household pin) from Texas Instrument (Dallas, TX)

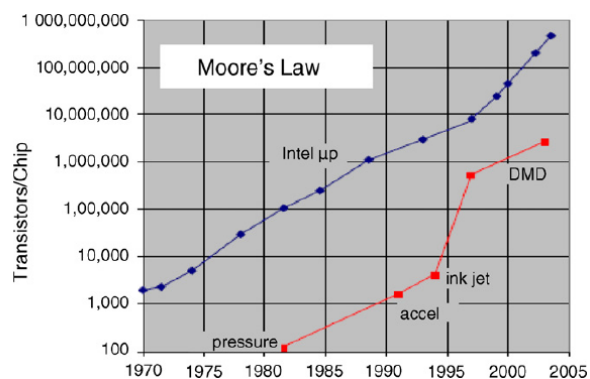


Figure A-7: Comparable trend of MEMS technology development to Moore's law in IC industry. Image reprinted from [16].

Because of different focus, as stated previously, MEMS fabrication technology over the years has evolved to be “micromachining” to differentiate itself from IC-type microfabrication. Other than standard silicon processing techniques [17] including photolithography, oxidation, doping, thin-film deposition, wet chemical etching, and dry plasma etching, special techniques [6]—such as HNA/KOH/TMAH (wet) and XeF_2 (dry) silicon etching, electroplating, LIGA (German acronym for x-ray lithography, electroforming, and molding), deep-reactive-ion etching (DRIE), and wafer bonding—have also been developed in silicon-based micromachining to enable fabrication of complex 2-D and 3-D mechanical structures out of silicon wafer (as shown in Figure A-8 [12]). They are generally categorized as bulk micromachining and surface micromachining and are respectively described as follows.

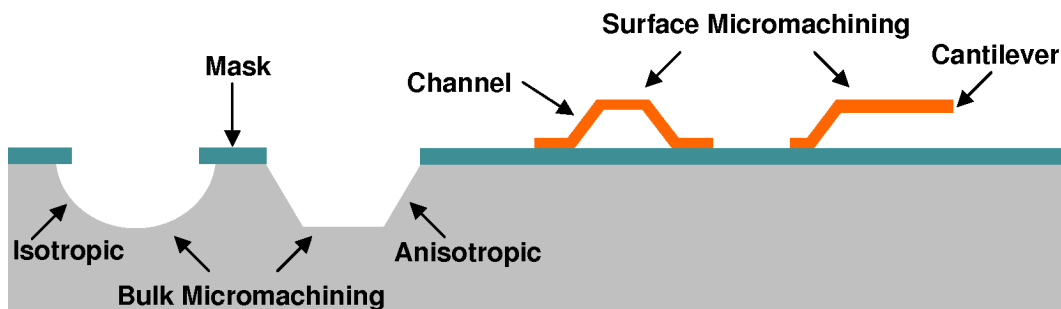


Figure A-8: Silicon-based micromachining technology including bulk micromachining (left) and surface micromachining (right). Image reprinted from [12].

Bulk micromachining [18] refers to selectively removing/etching significant amounts of substrate material—silicon in most cases—to create the designed structures. By using different kinds of etching methods, the silicon substrate can be orientationally (isotropically or anisotropically) micromachined (as shown in Figure A-9) so as to create

a wide variety of micromechanical structures [19] for different purposes. Since the invention of DRIE process [18], the capability of bulk micromachining has been expanded to create vertical holes/trenches so that high-aspect-ratio (HAR) structures (as shown in Figure A-10) can be realized for more extensive applications.

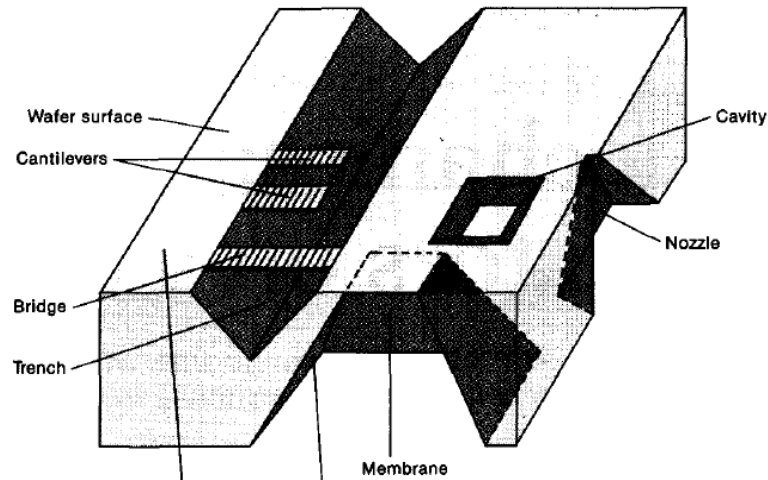


Figure A-9: Bulk-micromachined structure examples. Image reprinted from [19].

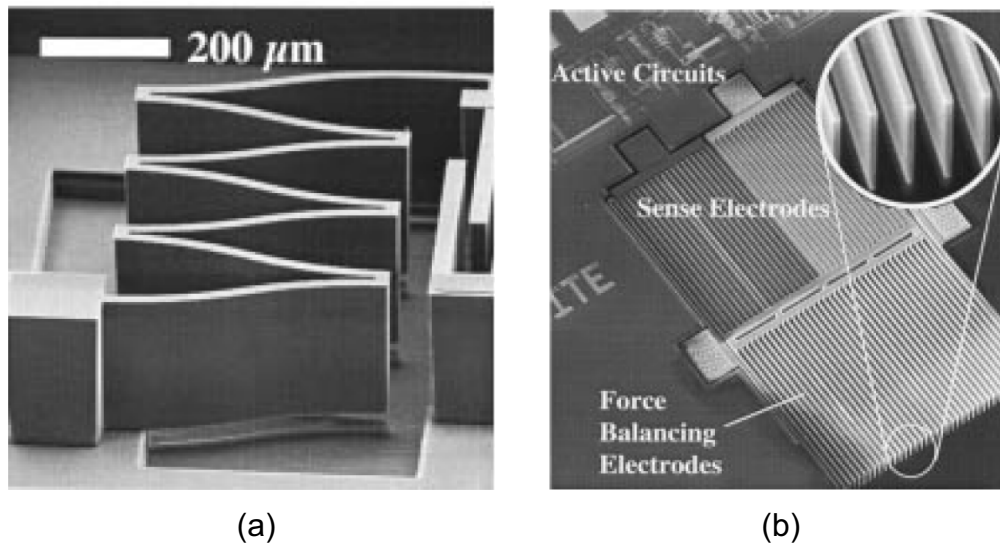


Figure A-10: Examples of high-aspect-ratio (HAR) structures created by DRIE. (a) Leaf spring. (b) Comb beams. Image reprinted from [18].

Surface micromachining [20] refers to sequentially depositing and patterning layers of thin-film sacrificial and structural materials on the surface of the substrate to create the designed structures after releasing the sacrificial material (as shown in Figure A-11). Given this concept and the available delicate patterns on the photomasks, highly complex surface-micromachined devices can be built as shown in Figure A-12. Not only planar structures, but out-of-plane structures/devices (as shown in Figures A-13 and A-14) can also be realized using surface micromachining with the assistance of sophisticated manipulation and/or assembly techniques [21] after fabrication.

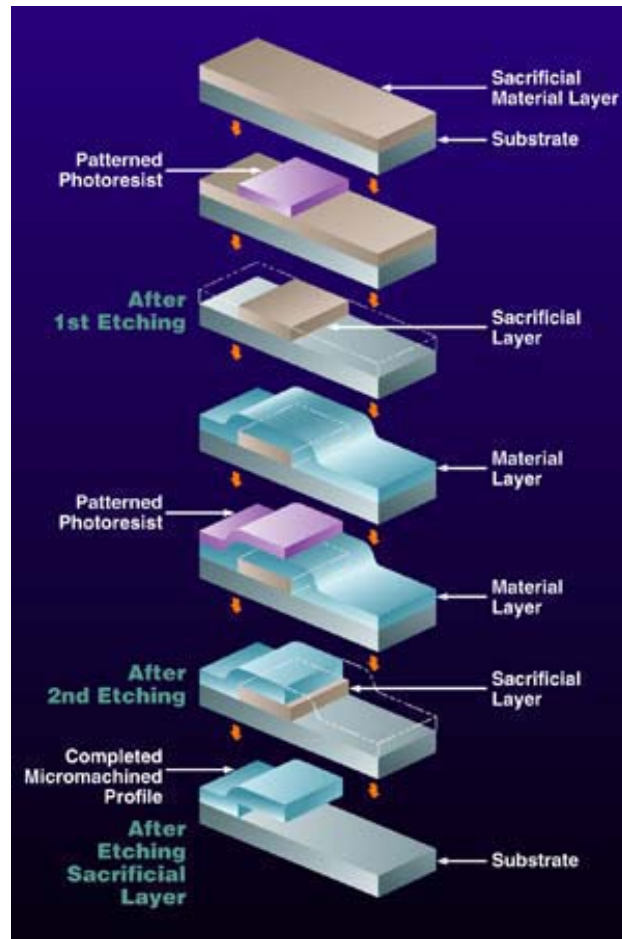


Figure A-11: Concept of surface micromachining. Image courtesy of Southwest Research Institute (SwRI).

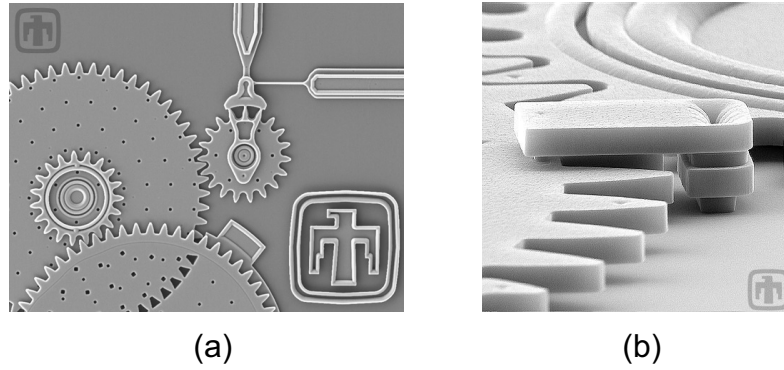


Figure A-12: Micromachined structures by SUMMiT™ Technologies. (a) Multiple gear speed reduction unit. (b) Gear alignment clip. Images courtesy of Sandia National Laboratories.

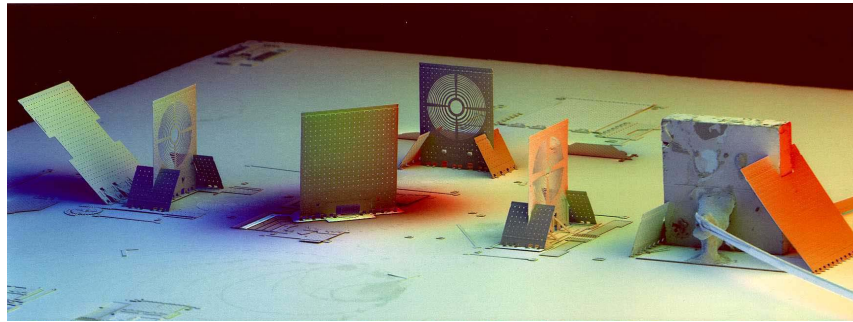


Figure A-13: Micro optics system including laser, 3 Fresnel lenses, beam splitter, and 45° mirror. Images courtesy of Dr. Ming C. Wu.

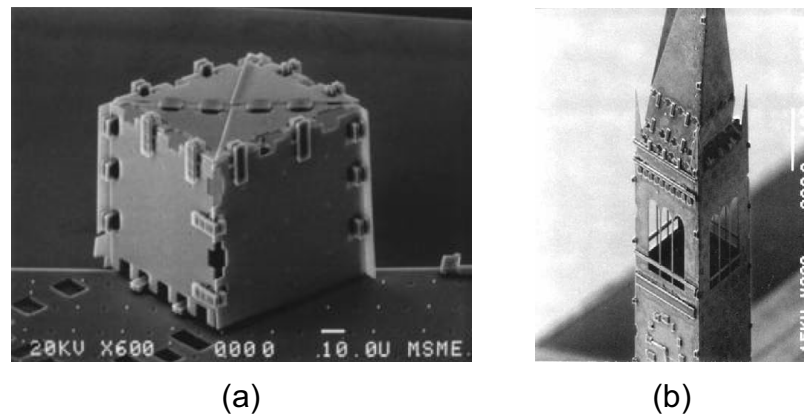


Figure A-14: Assembled 3-D microstructures. (a) Pop-up box. (b) Model of UC Berkeley Campanile clock tower. Images reprinted from [21].

Because of the maturity of both processing techniques, state-of-the-art micromachining often involves hybrid processes in which both bulk and surface micromachining are applied to realize specific structures and enhance their performance. Critical issues/challenges such as CMOS/MEMS integration, system integration, packaging, and reliability are mainstream in current research topics of fabrication technologies toward the successful development and commercialization of MEMS.

A.1.3 Products and market

With successful technology development, versatile MEMS products have been brought to the market from both academic and industrial efforts. This evolution can be clearly seen from Figure A-15 [22]. Nowadays MEMS business is still in rapid growth, with estimated global market reaching 10.8 M USD in 2011, as shown in Figure A-16 [23] (even only when taking into account silicon/quartz-based devices). As of 2008, more than 450 MEMS industrial players worldwide have been identified, with geographical breakdown shown in Figure A-17 [24]; the top 30 players are listed in Figure A-18 [25].

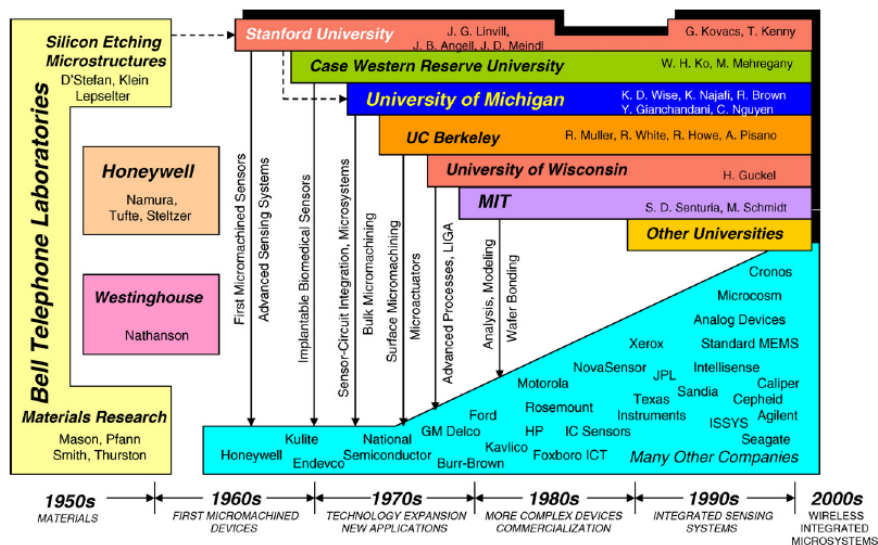


Figure A-15: MEMS evolution. Images reprinted from [22].

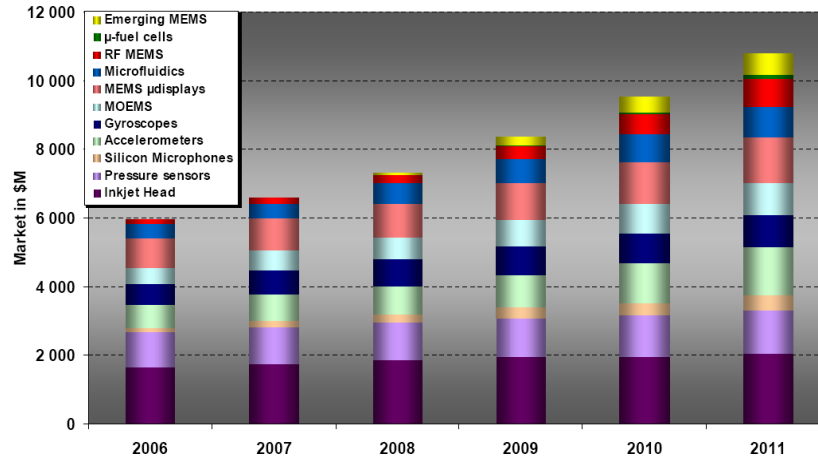


Figure A-16: Analysis of global MEMS market 2006–2011. Images reprinted from [23].

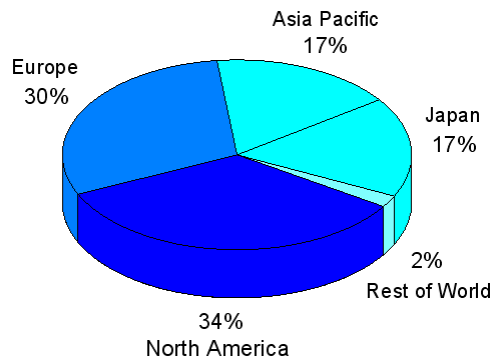


Figure A-17: Geographical breakdown of MEMS players. Image adapted from [24].

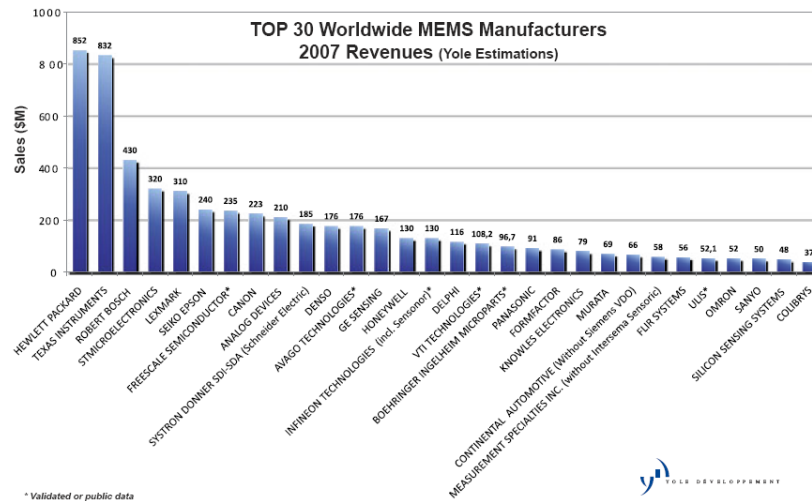


Figure A-18: Top 30 worldwide MEMS manufacturers (ranked by estimated 2007 revenues). Image reprinted from [25].

Given the demonstrated progress on physical, optical, and RF MEMS products, the next wave is unanimously believed to be on bioMEMS, lab-on-a-chip systems, implantable MEMS devices/systems, or generic MEMS components for life sciences. The expected business growth is shown in Figure A-19, implicitly reflecting the high need of such products in the market.

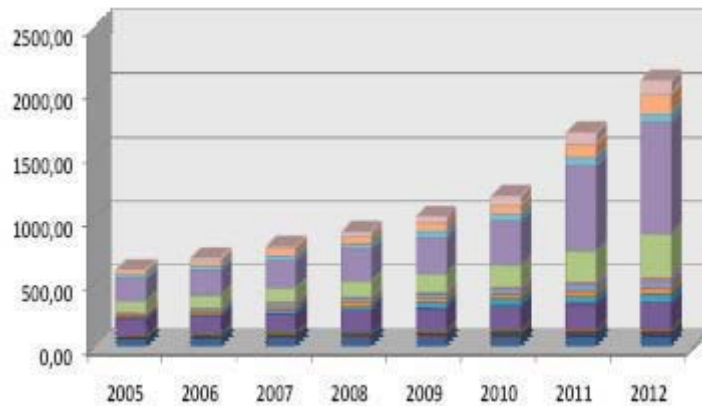


Figure A-19: Analysis of MEMS components for life sciences market 2005–2012. Image reprinted from [26].

A.2 Implantable Medical MEMS

Implantable medical MEMS, or MEMS implants, are a rising field and have attracted significant attentions from engineering, biological, and medical societies [27–30]. This emerging technology aims to apply microtechnologies/microdevices to human health care, driven by the increasing desire for better study of physiology and for better quality of life. Critical building blocks of such devices/systems include processing, packaging, communication, power, and materials—especially the latter two. Because the devices are designed to be implanted inside the human body, their power consumption and biocompatibility come first in minimizing interference to the body tissue and meeting

regulatory requirements (e.g., approval from the Food and Drug Administration (FDA) in the U.S.). Inclusion of MEMS processing technology favorably facilitates fabricated devices in a small form factor, suitable for minimally invasive and painless implantation, as well as for placement inside delicate organs or at specific locations to accomplish specific operations. Prospective application targets cover the human body, as shown in Figure A-20 [30]. Depending on their use, the state-of-the-art MEMS implants can be categorized into acute (temporary) and chronic (long-term) types, as shown in Figures A-21 and A-22, respectively, with more detailed descriptions in [30].

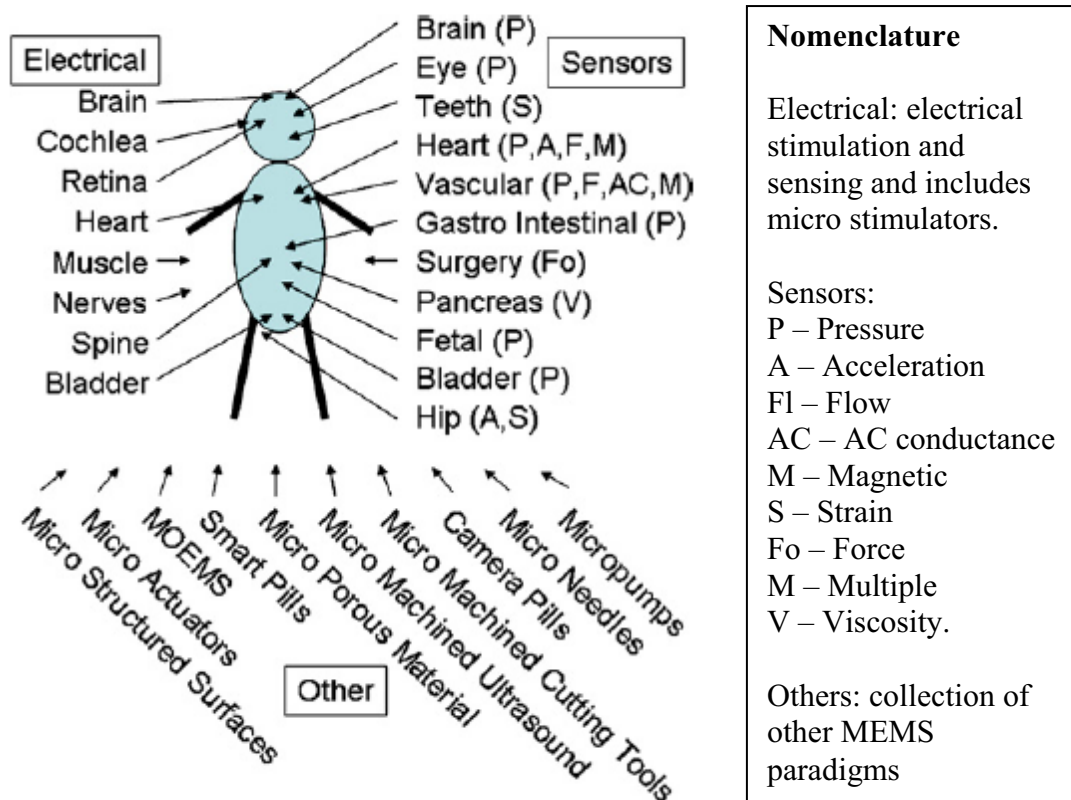


Figure A-20: MEMS for implantable applications. Image reprinted from [30].

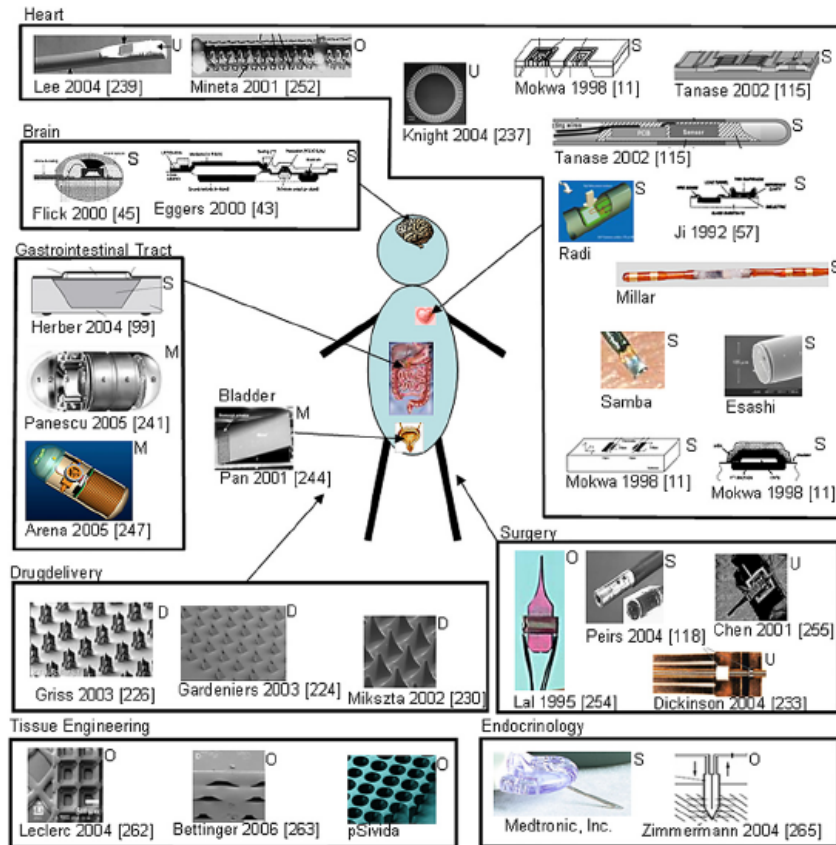


Figure A-21: Graphical overview of acute MEMS implants. Image reprinted from [30].

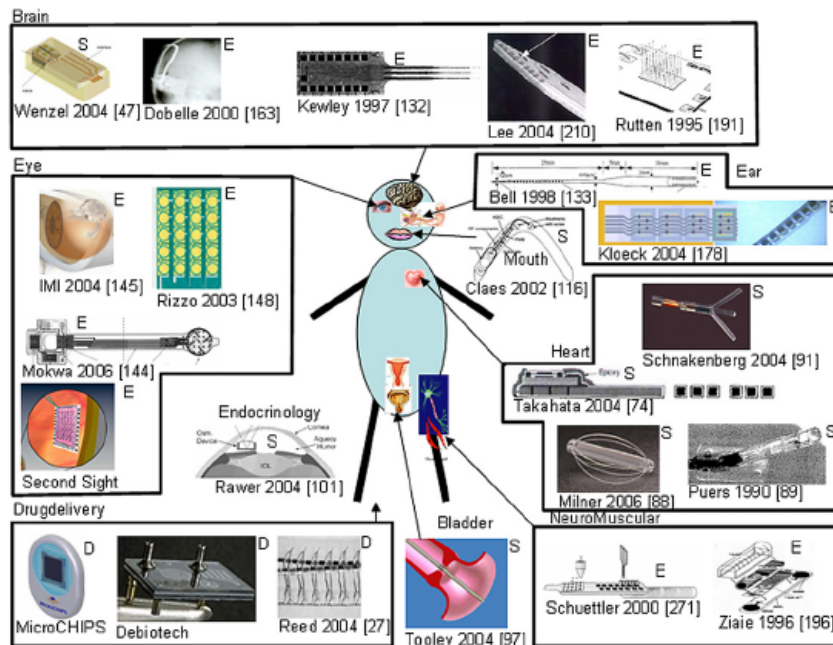


Figure A-22: Graphical overview of chronic MEMS implants. Image reprinted from [30].

From the examples in Figures A-21 and A-22, it is evident that the implantable medical MEMS diverge from typical MEMS paradigms based on exclusive device concepts and material selections. Conventional MEMS materials, including silicon and CMOS-compatible thin films, are not the only choices in this field. In fact, use of polymeric materials has been found to allow implants to have more flexibility, more processing availability, more shaping possibility (including 3-D conformations), easier packaging and integration, lower cost, and more configurable structural/chemical/biological functionalities. Associated polymeric MEMS materials and polymer micromachining have therefore been broadly researched and engineered to pursue ultimate realization of certain ideal MEMS implants.

A.3 Polymeric MEMS Materials

A.3.1 Overview

Polymers (including elastomers, plastics, and fibers) have been increasingly exploited as MEMS materials since the 1990s [31], motivated by the aforementioned reasons. Typical microfabricated structures include device substrates, structural thin films, functional thin films, adhesives, packaging, and coating, mainly for flexible devices and life science applications. Table A-1 summarizes representative polymeric MEMS materials as well as their processing methods and demonstrated applications. Because of their ease of processing and configurable functionalities, polymeric materials are prevalent in microfluidics for flow control and fluid transportation components. More knowledge of polymers has been adapted to micromachining technologies in order to construct functional and reliable MEMS devices/systems. Among the listed polymers,

parylene has exclusive physical/chemical/biological properties, so it is specifically discussed in the following to justify the development of parylene-based MEMS implants in this work.

Table A-1: Representative polymeric MEMS materials. Table adapted from [31].

Material	Processing methods	Demonstrated applications
Parylene (poly-para-xylene)	Chemical vapor deposition	Microfluidics; flexible structures and devices
Polyimide	Spin coating; extrusion	Substrates; microfluidics
Acrylics	Molding	High-aspect-ratio structures; microfluidic channels
PDMS (poly-dimethyl-siloxane)	Molding	Microfluidic channels, pumps, and valves
Liquid crystal polymer	Chemical etching	Flow sensors
Biodegradable polymer	Molding	Drug delivery devices
SU-8 epoxy	Photo patterning; spin casting	Artificial haircell sensors; microfluidic gaskets
Poly-urethane	Molding	Micromechanical structures
Nanocomposite elastomer	Screen printing; molding	Conductors; sensors and actuators

A.3.2 Parylene

Parylene (poly-para-xylene) as a MEMS material has been extensively investigated in our research group since the last decade [32, 33]. While its invention can be traced back to 1947 [34], it was commercialized in 1965 by Union Carbide Corporation (now Specialty Coating Systems Inc., Indianapolis, IN). Parylene is the official trade name for a family of semicrystalline thermoplastic polymers. Figure A-23 gives currently commercially available parylene types [35], where parylene N (no chlorines on the benzene ring), parylene C (one chlorine on the benzene ring), and

parylene D (with two chlorines on the benzene ring) are the originally commercialized derivatives, while other types such as parylene HT (fluorinated version) and dix A/AM (amino function groups on the benzene ring) are also available from Specialty Coating Systems and Kishimoto Sangyo Co., Ltd in Japan, respectively.

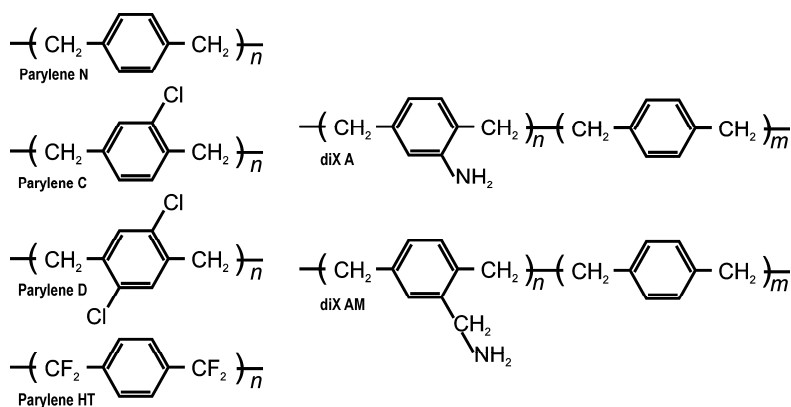


Figure A-23: Commercially available parylene types. Image reprinted from [35].

The preparation of parylene is conducted by the Gorham vapor-deposition process [36–38], a room-temperature chemical vapor deposition (CVD) polymerization process as shown in Figure A-24 with parylene N as an example. The commercially available dimer (di-para-xylene) in powder form is placed in the vaporizer to be sublimated at elevated temperature (120–150°C), then broken into monomers when it passes through the pyrolysis furnace at 650–750°C. The monomers enter the deposition chamber, which is held at room temperature, and conformally polymerize all exposed surfaces without pinholes. The process pressure is in the range of 20–35 mT to modify the monomer mean free path to the coated substrate. Residual monomer is collected on the cold trap. Different process conditions need to be applied to perform deposition of different variants of parylene. Typical deposited parylene film thickness from a single run is 0.1–30 μm in a PDS 2010 Labcoater™ system from Specialty Coating Systems.

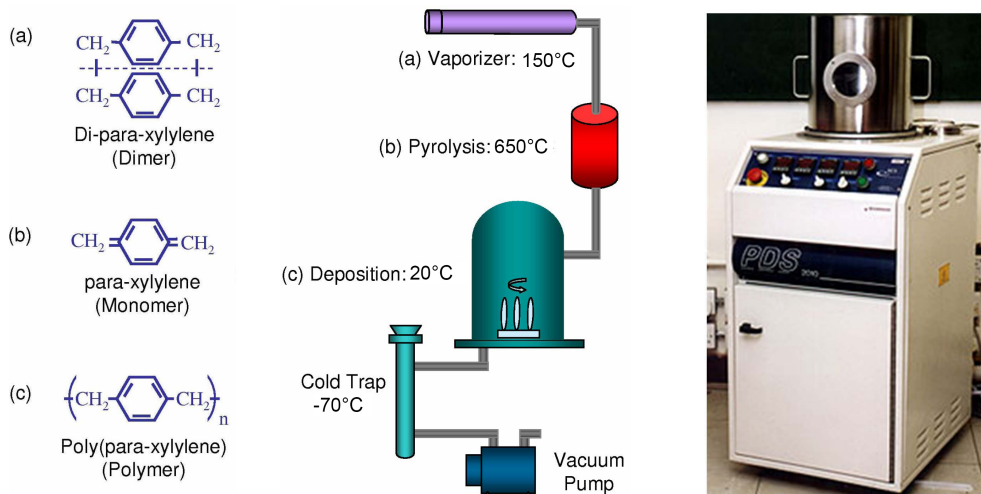


Figure A-24: Parylene preparation. (center) Process diagram. (left) Chemical structures at corresponding steps. (right) Photograph of actual deposition system (PDS 2010 Labcoater™ from Specialty Coating Systems). Images reprinted from [37, 38].

The material properties of parylene summarized in Tables A-2 and A-3 [38, 39] indicate its potential for electrical, mechanical, and physical applications. More importantly, its thin-film nature, chemical/biological inertness, and excellent barrier characteristics (low water absorption and low gas/liquid permeability) enable parylene to be used as a coating material in the electronics and medical industries, with successful demonstrations in pace-makers and other cardiac assist devices, stents, surgical tools, implantable electronics, and catheters [40, 41]. Studies have confirmed that parylene C is a long-term biocompatible material meeting ISO 10993 standard and United States Pharmacopeia (USP) Class VI grade (the highest biocompatibility rating for plastics in the U.S.) [39–43]. Furthermore, parylene C films have been implanted in live rabbit eyes for six months with no detectable adverse immune response such as inflammation, tissue fibrosis, or other post-operation complications [38]. This fact strongly supports the biocompatibility and biostability of parylene in the unique intraocular environment.

Table A-2: Material properties of parylene N, C, D, and HT. Table adapted from [38].

Property	Parylene N	Parylene C	Parylene D	Parylene HT
Dielectric strength (V/mil), 1 mil film	7,000	5,600	5,500	5,400
Dielectric constant				
60 Hz	2.65	3.15	2.84	2.21
1 kHz	2.65	3.10	2.82	2.20
1 MHz	2.65	2.95	2.80	2.17
Young's modulus (psi)	350,000	400,000	380,000	—
Yield strength (psi)	6,100	8,000	9,000	—
Elongation to break (%)	20–250	200	10	—
Coefficient of friction				
Static	0.25	0.29	0.33	0.145
Dynamic	0.25	0.29	0.31	0.130
Density (g/cm ³)	1.10–1.12	1.289	1.418	—
Melting point (°C)	420	290	380	> 450
Thermal conductivity at 25°C (10 ⁻⁴ cal/cm-s-°C)	3.0	2.0	—	—
Specific heat at 20°C (cal/g-°C)	0.20	0.17	—	—
Water absorption (% after 24 hours)	< 0.1	< 0.06	< 0.1	< 0.01
Index of refraction	1.661	1.639	1.669	—

Table A-3: Comparison of parylene N, C, and HT. Table adapted from [38].

Property	Parylene N	Parylene C	Parylene HT
Thickness Control	Excellent	Excellent	Excellent
Coating Speed	Medium	High	Low
Crevice Penetration	Better	Good	Best
Hardness	Better	Good	Best
Coefficients of Friction	Better	Good	Best
Thermal Stability	Moderate	Moderate	Excellent
Gas Permeability	Better	Best	Good
Moisture Resistance	Better	Best	Good
Chemical Resistance	Excellent	Excellent	Excellent

Micromachining of parylene involves film deposition, photolithography (pattern generation), and oxygen plasma etching (pattern transfer), all of which can be done at low temperatures ($< 120^{\circ}\text{C}$). Parylene C (poly-chloro-p-xylylene) is frequently used as the MEMS material because of its processing convenience and satisfactory material properties, so the mentions of parylene in this work are assumed to refer to parylene C unless stated otherwise. Although standard silicon wafers are usually used for process compatibility, the coated substrate can be made out of virtually any material. The processed parylene film from a silicon substrate (as shown in Figure A-25 [44]) maintains its original flexibility and transparency. As a result, the entire process is compatible with general CMOS/MEMS microfabrication processes, and thus can be expanded to multi-layer parylene surface micromachining technology that integrates silicon and metal processes (as shown in Figure A-26) to build complex parylene-based structures and features [45]. Device examples facilitated by such enabling technology are given in Figure A-27 [32, 46] with a great focus on microfluidic components such as fluid channels/columns, pumps, valves, filters, pressure/flow sensors, mass flow controllers, and electrospray nozzles. An integrated parylene-based microsystem for serial on-chip liquid chromatography and tandem mass spectrometry (LC-MS/MS) is shown in Figure A-28 [47] as a demonstration of applying such technology.



Figure A-25: Processed parylene film from a silicon wafer. Image reprinted from [44].

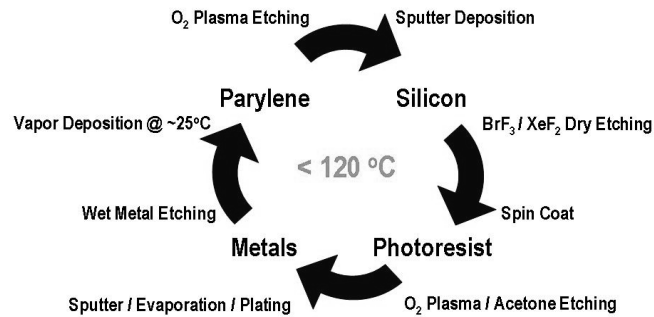


Figure A-26: Concept of low-temperature multi-layer parylene micromachining technology. Diagram reprinted from [45].

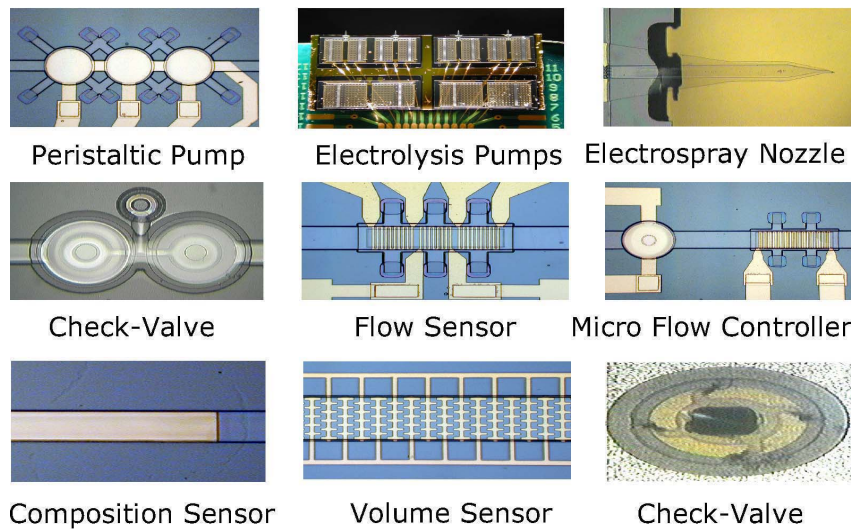


Figure A-27: Microfabricated parylene-based devices. Images reprinted from [32, 46].

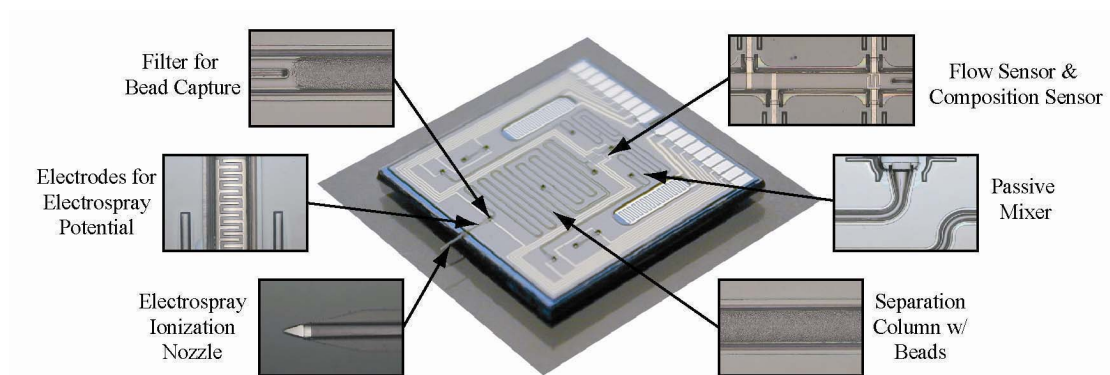


Figure A-28: Integrated parylene LC-MS/MS microsystem. Image reprinted from [47].

Similar to other polymers such as polyimide, silicone, PMMA, and SU-8, trials using parylene in MEMS medical implants have been investigated more versatile shapes and functions, due to its thin-film nature, as compared with other bulky candidates. Depending on surgical placements and associated procedures, parylene can be used as a coating material on rigid structures or directly used as a structural material. For example, parylene-coated silicon neural probes having multi-electrode arrays (MEAs) and integrated with flexible parylene cables have been reported (as shown in Figure A-29) for multi-channel cortex neural signal recording and stimulation [48]. On the other hand, flexible devices having MEA in different density and configuration have been reported for spinal cord and retinal stimulation as shown in Figures A-30 and A-31, respectively [38]. Facilitated by the use of parylene, all the demonstrated implants are identified as having minimally invasive features and high biocompatibility for chronic implantation. Given such technology, therefore, diverse parylene-based MEMS medical implant paradigms can be created to ultimately benefit people's lives.

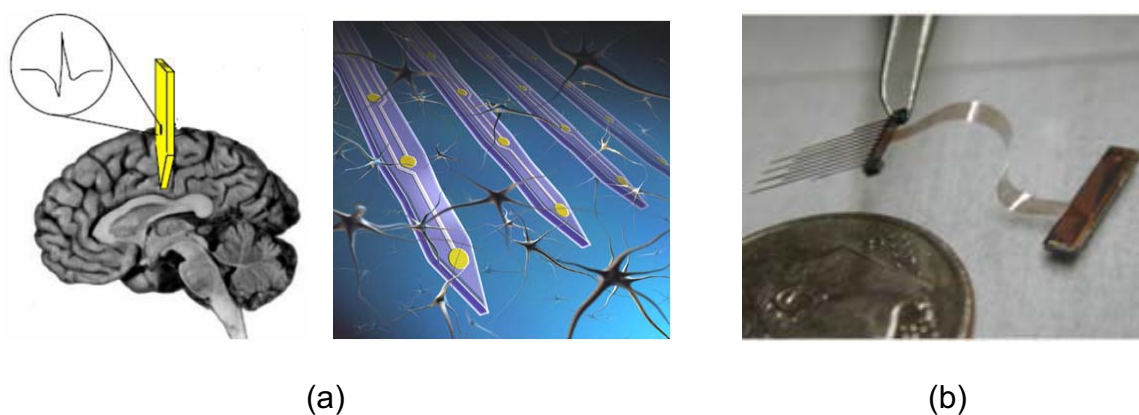


Figure A-29: Neural probe implant for cortex signal recording and stimulation. (a) Concept and surgical placement. (b) Microfabricated parylene-coated silicon neural probe with flexible parylene cable for electrical interconnection. Images reprinted from [48].

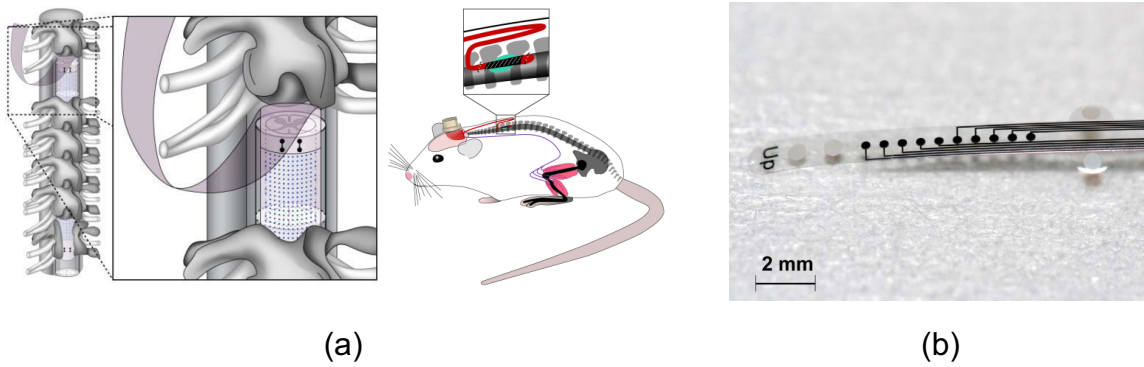


Figure A-30: Spinal cord prosthesis for neural stimulation. (a) Concept and surgical placement. Animal is drawn as the illustrative model. (b) Microfabricated parylene-based MEAs with designed surgical features. Images reprinted from [38].

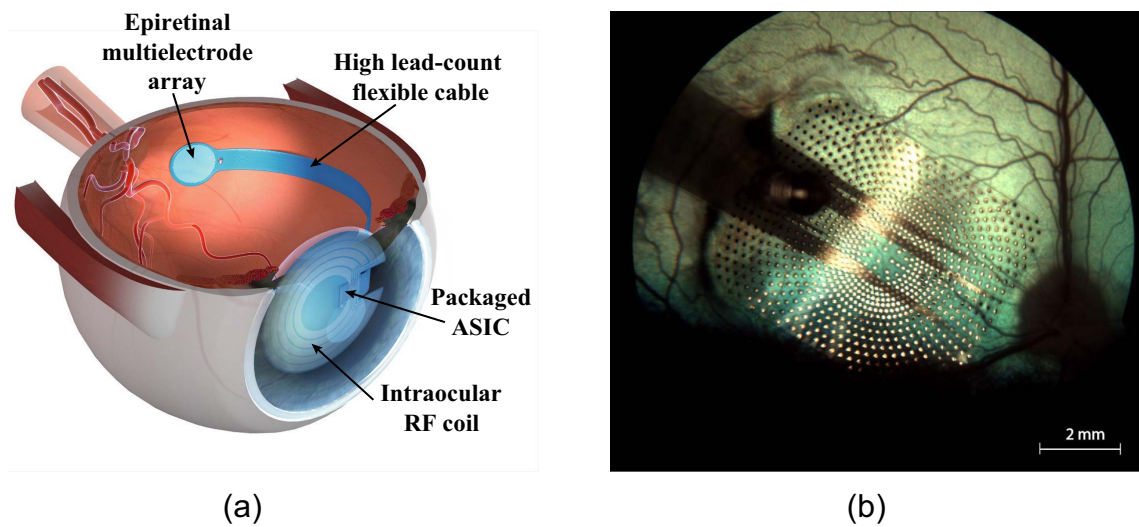


Figure A-31: Integrated intraocular prosthesis for retinal stimulation. (a) Concept and surgical placement. The parylene-based MEA is designed to be located at epiretina in the intraocular environment. (b) Fundus photograph of high-density (1024 pixels) parylene-based MEAs tacked to the retina of a canine eye. Images reprinted from [38].

A.4 Summary

This appendix gives an overview of MEMS definition, trend, and evolution. Core MEMS processes, including bulk and surface micromachining, are briefly described to show the capability of such enabling technology in microfabricated devices/systems covering a wide variety of applications, including implantable MEMS (MEMS implants). Minimally invasive biocompatible medical microdevices can be created with suitable form factor and material from designed MEMS processes. Among all available solid-state and polymeric MEMS materials, parylene has exclusive properties, such as high mechanical flexibility, great chemical resistance, electrical insulation, optical transparency, and ease of processing. A CMOS/MEMS-compatible multi-layer parylene micromachining technology has been developed to fabricate flexible and reliable parylene-based microdevices. With seamless combination of design, material selection, and technologies, various biocompatible parylene-based MEMS implants can be realized, with great potential for medical applications.

A.5 Bibliography

- [1] R. P. Feynman, "There's plenty of room at the bottom," *J. Microelectromech. Syst.*, vol. 1, pp. 60–66, 1992 (reprint).
- [2] R. P. Feynman, "Infinitesimal machinery," *J. Microelectromech. Syst.*, vol. 2, pp. 4–14, 1993 (reprint).
- [3] M. Gad-el-Hak, in *The MEMS Handbook*, 2nd ed. vol. 3, M. Gad-el-Hak, Ed. Boca Raton, FL: CRC Press, 2006.
- [4] W.S. Trimmer, Ed., *Micromechanics and MEMS: Classic and Seminal Papers to 1990*, Piscataway, NJ: IEEE Press, 1997.
- [5] K. E. Petersen, "Silicon as a mechanical material," *P. IEEE*, vol. 70, pp. 420–457, 1982.
- [6] G. T. A. Kovacs, *Micromachined Transducers Sourcebook*. Boston, MA: McGraw-Hill, 1998.
- [7] N. Maluf, *An Introduction to Microelectromechanical Systems Engineering*, Norwood, MA: Artech House, 2000.
- [8] S. D. Senturia, *Microsystem Design*, New York: Springer, 2001.
- [9] M. J. Madou, *Fundamentals of Microfabrication: The Science of Miniaturization*, 2nd ed., New York: CRC Press, 2002.
- [10] S. M. Sze, *Semiconductor Sensors*, New York: John Wiley & Sons, 1994.
- [11] A. Hierlemann, O. Brand, C. Hagleitner, and H. Baltes, "Microfabrication techniques for chemical/biosensors," *P. IEEE*, vol. 91, pp. 839–863, 2003.
- [12] Q. He, "Integrated nano liquid chromatography system on-a-chip," Ph.D. dissertation, Dept. Elect. Eng., Calif. Inst. Technol., Pasadena, CA, 2005.

- [13] H. C. Nathanson, W. E. Newell, R. A. Wickstrom, and J. R. Davis, Jr., "The resonant gate transistor," *IEEE T. Electron Dev.*, vol. ED-14, pp. 117–133, 1967.
- [14] L.-S. Fan, Y.-C. Tai, and R. S. Muller, "IC-processed electrostatic micromotors," *Sens. Actuat.*, vol. 20, pp. 41–47, 1989.
- [15] Y.-C. Tai and R. S. Muller, "IC-processed electrostatic synchronous micromotors," *Sens. Actuat.*, vol. 20, pp. 49–55, 1989.
- [16] K. Peterson, "A new age for MEMS," in *Proc. 13th Int. Transducers Conf.*, Seoul, Korea, pp. 1–4, Jun. 5–9, 2005.
- [17] S. Wolf and R. N. Tauber, *Silicon Processing for the VLSI Era*, 2nd ed., vol. 1, Sunset Beach, CA: Lattice Press, 2000.
- [18] G. T. A. Kovacs, N. I. Maluf, and K. E. Petersen, "Bulk micromachining of silicon," *P. IEEE*, vol. 86, pp. 1536–1551, 1998.
- [19] R. T. Howe, R. S. Muller, K. J. Gabriel, and W. S. N. Trimmer, "Silicon micromechanics: Sensors and actuators on a chip," *IEEE Spectrum*, vol. 27, pp. 29–35, 1990.
- [20] J. M. Bustillo, R. T. Howe, and R. S. Muller, "Surface micromachining for microelectromechanical systems," *P. IEEE*, vol. 86, pp. 1552–1574, 1998.
- [21] E. E. Hui, R. T. Howe, and M. S. Rodgers, "Single-step assembly of complex 3-D microstructures," in *Proc. 13th IEEE Int. Conf. MEMS*, Miyazaki, Japan, pp. 602–607, Jan. 23–27, 2000.
- [22] K. D. Wise, "Integrated sensors, MEMS, and microsystems: Reflections on a fantastic voyage," *Sens. Actuat. A: Phys.*, vol. 136, pp. 39–50, 2007.
- [23] *Status of the MEMS Industry*, Lyon, France: Yole Développement, 2007.

- [24] *Micronews*, Lyon, France: Yole Développement, no. 67, Mar. 2008.
- [25] *Micronews*, Lyon, France: Yole Développement, no. 70, Jun. 2008.
- [26] *BioMEMS*, Lyon, France: Yole Développement, 2008.
- [27] A. C. R. Grayson, R. S. Shawgo, A. M. Johnson, N. T. Flynn, Y. Li, M. J. Cima, and R. Langer, "A bioMEMS review: MEMS technology for physiologically integrated devices," *P. IEEE*, vol. 92, pp. 6–21, 2004.
- [28] Y. Haga and M. Esashi, "Biomedical Microsystems for minimally invasive diagnosis and treatment," *P. IEEE*, vol. 92, pp. 98–114, 2004.
- [29] W. Mokwa, "Medical implants based on microsystems," *Meas. Sci. Technol.*, vol. 18, pp. R47–R57, 2007.
- [30] R. A. M. Receveur, F. W. Lindemans, and N. F. de Rooij, "Microsystem technologies for implantable applications," *J. Micromech. Microeng.*, vol. 17, pp. R50–R80, 2007.
- [31] C. Liu, "Recent developments in polymer MEMS," *Adv. Mater.*, vol. 19, pp. 3783–3790, 2007.
- [32] X. Q. Wang, "Integrated parylene micro electro mechanical systems (MEMS)," Ph.D. dissertation, Dept. Electr. Eng., Calif. Inst. Technol., Pasadena, CA, 2000.
- [33] Y.-C. Tai, "Parylene MEMS: material, technology, and applications," in *Proc. 20th Sens. Symp.*, Tokyo, Japan, pp. 1–8, Jul. 23–24, 2003.
- [34] Special Coating Systems, "Parylene knowledge: Discovery/History," http://www.scscoatings.com/parylene_knowledge/history.aspx (accessed: Jul. 2, 2008)

- [35] E. Meng, P.-Y. Li, and Y.-C. Tai, "Plasma removal of parylene C," *J. Micromech. Microeng.*, vol. 18, 045004, 2008.
- [36] W. F. Gorham, "A new general synthetic method for preparation of linear poly-p-xylylenes," *J. Polym. Sci. A-1*, vol. 4, pp. 3027–3039, 1966.
- [37] V. C. Shih, "Temperature-controlled microchip liquid chromatography system," Ph.D. dissertation, Dept. Electr. Eng., Calif. Inst. Technol., Pasadena, CA, 2006.
- [38] D. C. Rodger, "Development of flexible parylene-based microtechnologies for retinal and spinal cord stimulation and recording," Ph.D. dissertation, Dept. Bioeng., Calif. Inst. Technol., Pasadena, CA, 2007.
- [39] *SCS Parylene Properties*, Indianapolis, MN: Specialty Coating Systems Inc., 2007.
- [40] L. Wolgemuth, "Crystal-clear coating covers components," *Med. Des.*, vol. 6, pp. 48–51, 2006.
- [41] L. Wolgemuth, "Parylene as a surface modifier (coating) for medical devices," presented at The 4th SMTA Medical Electronics Symposium, Bloomington, MN, May 2–3, 2007.
- [42] L. Wolgemuth, "Assessing the performance and suitability of parylene coating," *Med. Dev. Diagn. Ind.*, vol. 22, pp. 42–49, 2000.
- [43] *Certificate of Compliance, USP Biological Tests*. Northwood, OH: North American Science Associates, Inc., 2005.
- [44] T. N. Pornsinsirak, "Parylene MEMS technology for adaptive flow control of flapping flight," Ph.D. dissertation, Dept. Electr. Eng., Calif. Inst. Technol., Pasadena, CA, 2002.

- [45] E. Meng and Y.-C. Tai, "Parylene etching techniques for microfluidics and bioMEMS," in *Proc. 18th IEEE Int. Conf. MEMS*, Miami Beach, FL, pp. 568–571, Jan. 30–Feb. 3, 2005.
- [46] J. Xie, "Integrated parylene LC-ESI on a chip," Ph.D. dissertation, Dept. Electr. Eng., Calif. Inst. Technol., Pasadena, CA, 2004.
- [47] J. Shih, Y. Miao, T. D. Lee, and Y.-C. Tai, "Microfluidic platform for liquid chromatography—tandem mass spectrometry (LC-MS/MS)," in *Proc. 10th Int. MicroTAS Conf.*, Tokyo, Japan, pp. 1573–1575, Nov. 5–9, 2006.
- [48] C. Pang, "Parylene technology for neural probes applications," Ph.D. dissertation, Dept. Electr. Eng., Calif. Inst. Technol., Pasadena, CA, 2007.